

KEVIN GEISHENDORF

MAGNETOTRANSPORT  
EXPERIMENTS IN  
 $\text{Co}_3\text{Sn}_2\text{S}_2$   
MICROSTRUCTURES

TECHNISCHE UNIVERSITÄT DRESDEN



## *Magnetotransport Experiments in $\text{Co}_3\text{Sn}_2\text{S}_2$ Microstructures*



# *Magnetotransport Experiments in $\text{Co}_3\text{Sn}_2\text{S}_2$ Microstructures*

*Kevin Geishendorf*

Copyright © 2020 Kevin Geishendorf

TECHNISCHE UNIVERSITÄT DRESDEN  
FAKULTÄT FÜR PHYSIK

Dissertation zur Erlangung des akademischen Grades:  
Doctor rerum naturalium (Dr. rer. nat.)

Gutachter:

Prof. Dr. Kornelius Nielsch  
Prof. Dr. Georg Woltersdorf

Die Dissertation wurde im Zeitraum von April 2017 bis April 2020 am Leibniz-Institut für Festkörper- und Werkstoffforschung in Dresden angefertigt.

Hiermit erkläre ich, dass ich die vorliegende Dissertation selbständig verfasst, und keine anderen als die ausdrücklich angegebenen Hilfsmittel verwendet habe. Des Weiteren erkenne ich hiermit die Promotionsordnung des Bereichs Mathematik und Naturwissenschaften der Technischen Universität Dresden an.

(Kevin Geishendorf)

*April 2020*

# *Contents*

<i>Publication List</i>	9
<i>Preface</i>	11
<i>Introduction</i>	15
<i>Microstructure Preparation and Magnetic Properties</i>	23
<i>Magnetoresistance and Anomalous Hall Effect</i>	31
<i>Anisotropic Magnetoresistance</i>	41
<i>Thermomagnetic Transport</i>	57
<i>Summary and Outlook</i>	73
<i>Bibliography</i>	77





# *Publication List*

1. M. Schürmann, N. Shephard, N. Frese, K. Geishendorf, H. Sudhoff, A. Göhlhäuser, U. Rückert, C. Kaltschmidt, B. Kaltschmidt, and A. Thomas, “Technical feasibility study for production of tailored multielectrode arrays and patterning of arranged neuronal networks”, *PLOS ONE* **13**, 1–20 (2018).
2. K. Geishendorf, R. Schlitz, P. Vir, C. Shekhar, C. Felser, K. Nielsch, S. T. B. Goennenwein, and A. Thomas, “Magnetoresistance and anomalous hall effect in micro-ribbons of the magnetic weyl semimetal  $\text{Co}_3\text{Sn}_2\text{S}_2$ ”, *Applied Physics Letters* **114**, 092403 (2019).
3. M. Lammel, R. Schlitz, K. Geishendorf, D. Makarov, T. Kosub, S. Fabretti, H. Reichlova, R. Huebner, K. Nielsch, A. Thomas, and S. T. B. Goennenwein, “Spin Hall magnetoresistance in heterostructures consisting of noncrystalline paramagnetic YIG and Pt”, *Applied Physics Letters* **114**, 252402 (2019).
4. V. Barati, J. Garcia Fernandez, K. Geishendorf, L. U. Schnatmann, M. Lammel, A. Kunzmann, N. Pérez, G. Li, G. Schierning, K. Nielsch, and H. Reith, “Thermoelectric characterization platform for electrochemically deposited materials”, *Advanced Electronic Materials*, 1901288 (2020).
5. K. Geishendorf, P. Vir, C. Shekhar, C. Felser, J. I. Facio, J. van den Brink, K. Nielsch, A. Thomas, and S. T. B. Goennenwein, “Signatures of the magnetic entropy in the thermopower signals in nanoribbons of the magnetic weyl semimetal  $\text{Co}_3\text{Sn}_2\text{S}_2$ ”, *Nano Letters* **20**, 300–305 (2020).
6. N. Meyer, K. Geishendorf, J. Walowski, A. Thomas, and M. Münzenberg, “Photocurrent measurements in topological insulator  $\text{Bi}_2\text{Se}_3$  nanowires”, [arXiv:2001.05249] (2020).

7. L. Schnatmann, K. Geishendorf, M. Lammel, C. Damm, S. Novikov, A. Thomas, A. Burkov, H. Reith, K. Nielsch, and G. Schierning, "Signatures of a charge density wave phase and the chiral anomaly in the fermionic material cobalt monosilicide CoSi", *Advanced Electronic Materials* **6**, 1900857 (2020).
8. T. Tynell, K. Geishendorf, S. Piontek, T. Komossa, S. Schulz, K. Nielsch, and A. Thomas, "Rapid thermal annealing of Sb<sub>2</sub>Te<sub>3</sub> thin films grown via atomic layer deposition", *Thin Solid Films*, 137922 (2020).

# Preface

Reviewing the development of information technology in the past underlines the importance of advances in fundamental solid state research. In many cases such advances are directly linked to the discovery of effects with a large transport response. This is important for building devices, because a large transport response generally results in large and robust electrical signals. One of the most famous examples is the giant magnetoresistance (GMR), discovered in 1988, where a very large change of resistance occurs upon switching two neighbouring ferromagnetic layers between an antiparallel and an parallel state.<sup>1,2</sup> It was this large transport response, which enabled significant advances in the development of read heads for hard disk drives. Consequently, this led to rapid advances in the information technology in the following years. Of course not every discovery impacts information technology in such a successful and direct way, but this does not diminish the importance of understanding fundamental properties in solid state materials and how they impact the transport response.

The electrical properties of solids can be very successfully connected to its band structure. Materials are often distinguished based on the position of the Fermi level within the band structure, for example into insulators, semiconductors and metals. However, there is another paradigm to distinguish different states of matter which is based on topology. One of the earliest instances this concept was used in solid state physics was in connection with the quantum Hall effect.<sup>3</sup> The field evolved rapidly after the theoretical proposal and the experimental realization of a topological insulator.<sup>4,5,6</sup> This phase is characterized by a gap in the bulk states and gapless edge- or surface states. The peculiarity of those surface states is their topological origin and thereby special properties, such as the high mobility due to suppressed backscattering and the spin polarization through spin momentum locking. A natural question at that time was whether the existence of topological phases is only restricted to bulk insulating materials.

<sup>1</sup> M. N. Baibich et al., Phys. Rev. Lett. **61**, 2472–2475 (1988)

<sup>2</sup> G. Binasch et al., Phys. Rev. B **39**, 4828–4830 (1989)

<sup>3</sup> K. v. Klitzing et al., Phys. Rev. Lett. **45**, 494–497 (1980)

<sup>4</sup> C. L. Kane and E. J. Mele, Phys. Rev. Lett. **95**, 146802 (2005)

<sup>5</sup> L. Fu et al., Phys. Rev. Lett. **98**, 106803 (2007)

<sup>6</sup> M. König et al., Science **318**, 766–770 (2007)

Theoretical work soon predicted topological phases in conductors. As such, Dirac and Weyl semimetals were identified and experimentally verified. Up to date it poses an intriguing question to connect the existence of topological phases to interesting transport responses.

Very recent topological phases were also identified in magnetically ordered materials. This allows to explore the interplay of magnetism and topology. One especially interesting material is the magnetic Weyl semimetal  $\text{Co}_3\text{Sn}_2\text{S}_2$ . It hosts 8 pairs of Weyl points close to the Fermi level and possesses a very interesting magnetic ground state related to its Kagome structure.<sup>7</sup> The Weyl points can contribute significantly to the transport in this system as they are located near the Fermi level. One consequence is the enhanced Berry curvature, which in turn gives rise to a large intrinsic anomalous Hall effect (AHE) in  $\text{Co}_3\text{Sn}_2\text{S}_2$  bulk single crystals. To explore the transport properties arising from Weyl physics in more detail, it is important to realize microstructures of this unique compound, for example to facilitate non-local transport experiments.

<sup>7</sup> E. Liu et al., Nat. Phys. **14**, 1125–1131 (2018)

## *This Thesis*

The first part of this thesis reports on details of the fabrication of  $\text{Co}_3\text{Sn}_2\text{S}_2$  micro ribbon devices for transport experiments via focused ion beam cutting in combination with conventional lithography techniques. The magnetoresistive response and the AHE are carefully compared to bulk transport properties and predictions from band structure calculations. The well defined sample geometry makes such devices suitable for more complex transport experiments. This is used in the second part where the magnetoresistive response (MR) for different orientations of the external magnetic field is investigated. In this context the presence of an MR which appears to be sensitive to the crystalline c-axis is discussed.

It was established theoretically that the Berry curvature does not only impact the electrical transport properties but also influences the thermomagnetic response, namely the anomalous Nernst effect (ANE), of a system. Interestingly, there are subtle differences in the relation between Berry curvature and AHE compared to Berry curvature and ANE. In principal, this difference allows to investigate not only states below but also above the Fermi level.<sup>8</sup> The large AHE observed in  $\text{Co}_3\text{Sn}_2\text{S}_2$  immediately

<sup>8</sup> J. Noky et al., Phys. Rev. B **98**, 241106 (2018)

raises the question about the magnitude of the ANE. Therefore, thermomagnetic transport experiments are discussed in the third part.

Electrical and thermomagnetic transport coefficients are related through the Mott relation. A test of this relation was proposed and successfully employed by Pu and coworkers.<sup>9</sup> This model was applied to different material systems and achieved good agreement between the experimental results and the model. Testing this relation in  $\text{Co}_3\text{Sn}_2\text{S}_2$  revealed an additional contribution close to the magnetic ordering temperature which is not captured by the current model. Possible origins of this contribution are discussed and it is proposed that magnetic fluctuations are visible in the ANE.

<sup>9</sup> Y. Pu et al., Phys. Rev. Lett. **101**, 117208 (2008)

## *Acknowledgments*

I am grateful for all the help and advice that I received during the past three years. Therefore, I would like to especially thank:

- Prof. Dr. Kornelius Nielsch, for his supervision and for enabling me to complete this thesis at the Institute for Metallic Materials in Dresden
- Prof. Dr. Sebastian T.B. Gönnerwein, for sharing this project with me and, in particular, for his critical input to the scientific publications. I deeply appreciate the invaluable advice, that will accompany me on my future path
- Prof. Dr. Rudolf Schäfer, for his support with the MOKE microscopy investigations
- PD. Dr. Andy Thomas, for creating such a lively environment in the Quantum Materials and Devices group. Furthermore, I would like to thank him for all his advice concerning physics and other stuff
- Dr. Javier G. Fernandez, for introducing me to the lithography systems at the IMW
- Dr. Savio Fabretti, for sharing his knowledge on UHV systems and thin film synthesis with me
- Dr. Tommi P. Tynell for teaching me one or the other ALD trick and discussing his experiences as postdoctoral researcher

- Michaela R. Lammel, for seeing the bright side of things, when I could not. I also thank her for always having an open ear to talk about physics, life and other things. Her positive mind inspired me every day
- Richard Schlitz, for his help building up the measurement setup and the split coil cryostat. I would also like to thank him for his help with all the measurements in the Chaos setup and for nudging me to use python for the data evaluation. I am thankful for all the things I could learn from him in the lab and that he keeps challenging me with his cryptic answers
- Lauritz U. Schnatmann, for his help with my quantum mechanics course and for proof-reading this thesis
- Almut Pöhl, for her outstanding skill and dedication to the FIB preparation of the  $\text{Co}_3\text{Sn}_2\text{S}_2$  micro ribbons
- My parents, for not only encouraging me to pursue my own path, but enabling me to do so through their support
- Anne-Sophie, for her crucial support throughout all ups and downs of the past three years

# Introduction

## Topological Materials

The classification of matter and phases according to spontaneous symmetry breaking finds frequent application in all fields of physics. One of the first exceptions not captured by this paradigm is the quantum Hall effect first discovered by Klitzing, Dorda and Pepper in 1980.<sup>10</sup> The quantum Hall effect occurs in two dimensional electron gases under the influence of a finite external magnetic field. The transverse electrical conductivity (Hall conductivity) does not change linearly with the external magnetic field but only takes values which are integer multiples of  $e^2/h$ . This quantization occurs due to the formation of discrete conduction channels at the edges. Every time the transverse conductivity of the system changes by  $e^2/h$  it undergoes a quantum Hall transition by populating or depopulating a Landau level. The exceeding precision of the occurring quantization is noteworthy, with deviations to less than one part in  $10^9$ .<sup>11</sup> Interestingly, the quantization does not depend on material parameters such as the charge carrier concentration but has a more fundamental origin.<sup>12</sup> Another peculiarity is that the different quantum Hall phases can not be distinguished by any spontaneously broken symmetry. It was in that context that topological order was first proposed as additional classification scheme.<sup>13</sup>

Topological order does not distinguish phases based on their broken symmetries but rather on the discrete values of a topological invariant, the Chern number. For example in terms of the quantum Hall effect, where each quantum Hall state is distinguished by a different Chern number. However, the concept of topology in solid state physics was lacking attention until the theoretical prediction of so called topological insulators (TI) by Kane and Mele in 2005.<sup>14,15</sup> The experimental realization of such a phase was achieved in 2D HgCdTe quantum wells by König and coworkers in 2007.<sup>16</sup> The conduction in a 2D TI is restricted to

<sup>10</sup> K. v. Klitzing et al., Phys. Rev. Lett. **45**, 494–497 (1980)

<sup>11</sup> F Delahaye and B Jeckelmann, Metrologia **40**, 217–223 (2003)

<sup>12</sup> R. B. Laughlin, Phys. Rev. B **23**, 5632–5633 (1981)

<sup>13</sup> D. J. Thouless et al., Phys. Rev. Lett. **49**, 405–408 (1982)

<sup>14</sup> C. L. Kane and E. J. Mele, Phys. Rev. Lett. **95**, 226801 (2005)

<sup>15</sup> C. L. Kane and E. J. Mele, Phys. Rev. Lett. **95**, 146802 (2005)

<sup>16</sup> M. König et al., Science **318**, 766–770 (2007)

1D edge-states (cp. Figure 1a) similar to the quantum Hall effect and is quantized to  $2e^2/h$ . Furthermore, the two different spin species can only propagate in opposite directions, which is why 2D TIs are also called quantum spin Hall insulators. The quantized and dissipationless transport associated with the quantum Hall and quantum spin Hall effect are key aspects responsible for the numerous research activities. The layer stack used by König and coworkers consisted of a HgTe layer between CdTe layers. In CdTe, the conduction band states have  $s$  character whereas the valance band states have  $p$  character. For thin HgTe layers the 2D states in the quantum well have the same band order and the state equals a trivial insulator at low temperatures. However, it comes to a band inversion in the HgTe layer for thicknesses larger than 6.3 nm (cp. Figure 1b). This band inversion leads to a phase transition from a trivial insulator to a TI. In a simple picture one can imagine that the inverted parity of the  $s$  and  $p$  bands leads to unavoidable band crossings and with such to conducting states in the quantum well. The conducting states are often referred as topologically protected states, since the TI state is separated from the trivial insulator by a quantum phase transition and, therefore, can not be transformed into the other in a smooth fashion.

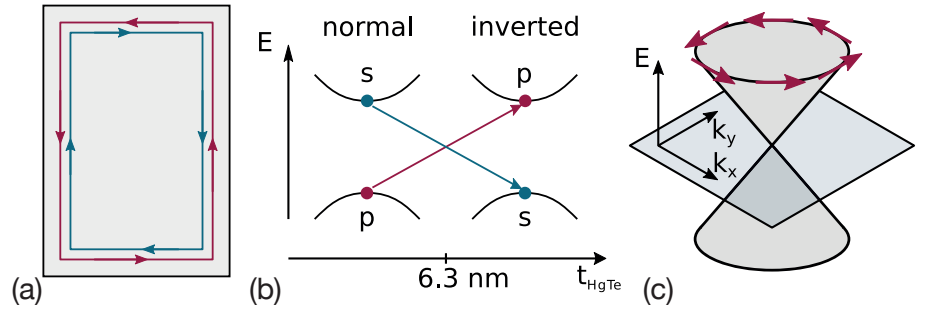


Figure 1: (a) Scheme of a 2D TI with 1D edge states. The opposite propagation direction for electrons with different spin is indicated with the blue and red arrows. (b) Band inversion in HgTe as a function of the layer thickness. The critical point is at approximately 6.3 nm. (c) Representation of a Dirac cone for example spanning the gap in a 3D TI. The red arrows indicate the spin momentum locking.

The concept of 2D TIs was soon after generalized to three dimensions (3D). In 3D TIs the conduction is restricted to surface states while the bulk is insulating. The surface states resemble the shape of two cones touching in one point. The low energy excitations close to the touching point can be described with a linear Dirac equation. Thus, the two cones together are referred to as Dirac cone (cp. Figure 1c). The surface states themselves are not necessarily topological protected. But in 3D TI the num-



ber of band crossings is odd and thereby at least one Dirac cone can not be gaped out without going through a quantum phase transition. This protection can be formulated in form of robustness against smooth changes of the Hamiltonian of the system and can for example be interpreted as robustness against small material variations. The first material for which topological surface states were proven experimentally was  $\text{Bi}_{1-x}\text{Sb}_x$ .<sup>17</sup> Soon after that a second generation of 3D TI materials was discovered with  $\text{Bi}_2\text{Se}_3$ ,  $\text{Bi}_2\text{Te}_3$  and  $\text{Sb}_2\text{Te}_3$ , which were mainly investigated regarding their thermoelectric properties.<sup>18,19,20</sup> At that time, all confirmations of materials as 3D TI were based on angle resolved photoelectron spectroscopy (ARPES) measurements. Electrical transport experiments followed, focussing mainly on the high mobility and suppressed backscattering of the surface states. Another exciting property of 3D TIs is the spin momentum locking of the surface states as illustrated in Figure 1c. In other words a current carried by the surface states is fully spin polarized. Different experiments have been dedicated to utilize this property in the field of spintronics e.g. as spin injector.<sup>21</sup>

Until this point, investigations of topological states were mainly restricted to band insulators. But metals can also host topologically protected states. Those states are again bound to band crossings. If two double degenerate bands cross, one speaks of a Dirac cone as for the surface states of a 3D TI. The touching points in the band structure are not necessarily topologically protected but can be protected by certain symmetries. Only materials where the Dirac points are symmetrically protected are referred to as Dirac semimetals. The required symmetries are space-inversion and time-reversal symmetry. If one breaks either one of the two it is possible to split the Dirac cone into two non-degenerate cones, which are separated in momentum space. Already in 1937, it was discussed that accidental touching points of non-degenerate electronic bands will resemble a linear dispersion in vicinity of the crossing point.<sup>22</sup> The low energy excitations related to such crossing points can be described by the Weyl equation, which is a special formulation of the Dirac equation for massless fermions with defined chirality proposed by Hermann Weyl in 1929.<sup>23</sup> Weyl nodes appear always in pairs of opposite chirality. Materials in which such Weyl nodes appear somewhat close to the chemical potential are named Weyl semimetals (WSM). The first materials predicted as WSM were magnetic phases such as pyrochlore iridates,  $\text{HgCr}_2\text{Se}_4$ ,  $\text{Hg}_{1-x-y}\text{Cd}_x\text{Mn}_y\text{Te}$  and ferromagnet/ TI heterostructures.<sup>24</sup> The magnetic order fulfills one of the require-

<sup>17</sup> D Hsieh et al., *Nature* **452**, 970–974 (2008)

<sup>18</sup> Y Xia et al., *Nat. Phys.* **5**, 398–402 (2009)

<sup>19</sup> Y. L. Chen et al., *Science* **325**, 178–181 (2009)

<sup>20</sup> D. Hsieh et al., *Phys. Rev. Lett.* **103**, 146401 (2009)

<sup>21</sup> Y. Q. Huang et al., *Nat. Commun.* **8**, 15401 (2017)

<sup>22</sup> C. Herring, *Phys. Rev.* **52**, 365–373 (1937)

<sup>23</sup> H. Weyl, *Z. Phys.* **56**, 330–352 (1929)

<sup>24</sup> X. Wan et al., *Phys. Rev. B* **83**, 205101 (2011)

<sup>25</sup> S.-Y. Xu et al., *Science* **349**, 613–617 (2015)

<sup>26</sup> B. Q. Lv et al., *Nat. Phys.* **11**, 724–727 (2015)

<sup>27</sup> L. X. Yang et al., *Nat. Phys.* **11**, 728–732 (2015)

<sup>28</sup> N Xu et al., *Nat. Commun.* **7**, 11006 (2016)

<sup>29</sup> S.-Y. Xu et al., *Nat. Phys.* **11**, 748–754 (2015)

<sup>30</sup> S. Souma et al., *Phys. Rev. B* **93**, 161112 (2016)

<sup>31</sup> S. L. Adler, *Phys. Rev.* **177**, 2426–2438 (1969)

<sup>32</sup> J. S. Bell and R. Jackiw, *Il Nuovo Cimento A* (1965–1970) **60**, 47–61 (1969)

<sup>33</sup> H. Nielsen and M. Ninomiya, *Phys. Lett. B* **130**, 389–396 (1983)

<sup>34</sup> A. Niemann et al., *Sci. Rep.* **7**, 43394 (2017)

ments for topological semimetals by breaking time-reversal symmetry. However, the first WSM to be confirmed experimentally was TaAs.<sup>25,26,27</sup> This compound has a broken space-inversion symmetry through its crystal structure rather than time-reversal symmetry breaking by magnetic order. Also other members of this material group, such as TaP, NbAs and NbP, where soon confirmed as WSM.<sup>28,29,30</sup>

The states related to the Weyl nodes are topological protected in the sense, that it is impossible to open a gap in only one of the nodes. To open a gap it is necessary to push two Weyl nodes of opposite chirality through the Brillouin zone until they annihilate. Furthermore, a pair of Weyl nodes is always connected via topologically protected surface states named Fermi arcs. Fermi arcs were successfully resolved in ARPES experiments.<sup>16,17,18</sup> Another interesting consequence of the Weyl nodes is the manifestation of the Adler-Bell-Jackiw (ABJ) anomaly in the magnetotransport.<sup>31,32,33</sup> The parallel component of an electrical and magnetic field lead to chiral symmetry breaking and, thus, to a creation of Weyl fermions of one chirality and the annihilation of Weyl fermions with the opposite chirality. In total, charge is conserved but chirality is not. In a simple picture as illustrated by Figure 2, one can imagine that a parallel electric and magnetic field pump Weyl fermions from one node into the other. The

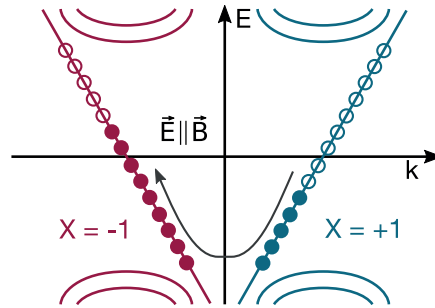


Figure 2: Energy spectrum of two Weyl nodes with opposite chirality. A parallel electric and magnetic field create/ annihilate Weyl fermions and thus lead to a chiral imbalance. The figure is adapted from Niemann et al.<sup>34</sup>

chiral magnetic effect creates a electrical current parallel to an external magnetic field in the presence of an chiral imbalance. The combination of ABJ anomaly and chiral magnetic effect leads to a positive correction to the magnetconductivity. This correction scales quadratically with the magnetic field since the chiral magnetic effect scales with  $\vec{B}$  and the chiral imbalance depends on the ABJ anomaly ( $\vec{E} \cdot \vec{B}$ ). The ABJ anomaly (sometimes chiral anomaly) is interpreted regularly as the transport signature

of WSM.<sup>35,36,37,38</sup> Recent experiments underline the necessity of caution when analyzing magnetoresistance measurements for parallel electric and magnetic field, since the artifact of current jetting produces a very similar transport response.<sup>39,40</sup>

Another manifestation of Weyl physics can be found in a contribution to the AHE<sup>41</sup> as invoked by Yang and coworkers in 2011.<sup>42</sup> They discussed the impact of the Weyl points acting as monopoles of Berry flux onto the anomalous Hall conductivity (AHC). The AHC in a model system with only two Weyl points, with the chemical potential directly at the Weyl node, depends only on the distance between the two Weyl nodes.<sup>43</sup> However, the situation in real materials is more complicated since the chemical potential usually does not reside exactly at the Weyl nodes.

Recently it is discussed that a large part of the AHE in body centered cubic (bcc) iron stems from two Weyl nodes in the band structure.<sup>44</sup> This is only one example how common topological features in the band structure are. Investigations based on quantum chemistry revealed that approximately 30% of all materials inherit topological non-trivial states.<sup>45,46</sup> This underlines the broad applicability of this new classification scheme for matter. Most important, novel phenomena are related to this new type of matter and therefore it is worth to further elucidate the impact of such topological protected features in the band structure onto for example electromagnetic transport responses. A reoccurring concept for the transport response of topological materials are the Berry phase and Berry curvature. Therefore, the next section is dedicated to the Berry curvature and its impact on the transport response, recognizing the central role of this concept.

## *Berry Curvature and Transport Response*

Imagine a system described by a set of parameters is moved through parameter space on a closed loop. The system is called nonholonomic/ anholonomic if it differs from the initial state after completing the loop. A very vivid example of nonholonomy is the parallel-transport on a 3D manifold. For simplicity assume a vector  $V$  being transported along a loop  $C$  on a sphere (cp. Figure 3a). The vector is moved along  $C$  in incremental steps and kept parallel to its previous position. After completing the loop  $V$  will have acquired an additional angle  $\alpha$  (or phase) to its initial position. This becomes clear if one flattens out the 3D manifold to 2D as shown in Figure 3b. Nonholonomicity enters in many

<sup>35</sup> H.-J. Kim et al., Phys. Rev. Lett. **111**, 246603 (2013)

<sup>36</sup> X. Huang et al., Phys. Rev. X **5**, 031023 (2015)

<sup>37</sup> C.-Z. Li et al., Nat. Commun. **6**, 10137 (2015)

<sup>38</sup> Z. Wang et al., Phys. Rev. B **93**, 121112 (2016)

<sup>39</sup> R. D. dos Reis et al., New J. Phys. **18**, 085006 (2016)

<sup>40</sup> Y. Li et al., Front. Phys. **12**, 127205 (2017)

<sup>41</sup> The AHE will be discussed in more detail in chapter 4.

<sup>42</sup> K.-Y. Yang et al., Phys. Rev. B **84**, 075129 (2011)

<sup>43</sup> A. A. Burkov, Phys. Rev. Lett. **113**, 187202 (2014)

<sup>44</sup> D. Gosálbez-Martínez et al., Phys. Rev. B **92**, 085138 (2015)

<sup>45</sup> B. Bradlyn et al., Nature **547**, 298–305 (2017)

<sup>46</sup> M. G. Vergniory et al., Nature **566**, 480–485 (2019)

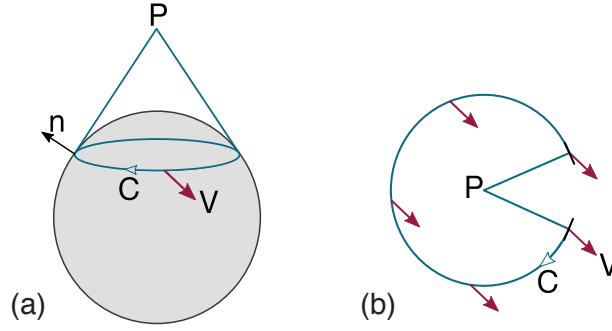


Figure 3: (a) Example for parallel transport of a vector  $V$  on a closed loop  $C$  on a non-planar manifold. (b) Flattened out cone in 2D as seen from point  $P$ . The vector  $V$  has a different angle after completing the loop. The figure is adapted from Ong et al.<sup>52</sup>

<sup>47</sup> R. Karplus and J. M. Luttinger, Phys. Rev. **95**, 1154–1160 (1954)

<sup>48</sup> S. Pancharatnam, Proc. Natl. Acad. Sci. India A **44**, 247–262 (1956)

<sup>49</sup> H. C. Longuet-Higgins et al., Proc. R. Soc. London. Ser. A **244**, 1–16 (1958)

<sup>50</sup> M. V. Berry, Proc. R. Soc. London. Ser. A **392**, 45–57 (1984)

<sup>51</sup> M. Born and V. Fock, Z. Phys. **51**, 165–180 (1928)

<sup>52</sup> N. P. Ong and W.-L. Lee, in Foundations of quantum mechanics in the light of new technology isqm-tokyo '05 (2005), 121–126

<sup>53</sup> J. Smit and J. Volger, Phys. Rev. **92**, 1576–1577 (1953)

<sup>54</sup> M.-C. Chang and Q. Niu, Phys. Rev. B **53**, 7010–7023 (1996)

<sup>55</sup> G. Sundaram and Q. Niu, Phys. Rev. B **59**, 14915–14925 (1999)

different fields of solid-state physics.<sup>47,48,49</sup>

The generalized concept for nonholonomicity in quantum systems was given by M. V. Berry in 1984.<sup>50</sup> A system in an unchanging environment will be in an eigenstate of the corresponding Hamiltonian ( $\hat{H}$ ).  $\hat{H}$  will vary as the system is moved through parameter space. For slow (adiabatic) changes the system will remain in an eigenstate of  $\hat{H}$ .<sup>51</sup> If the system is brought back to its initial state it will be in the same eigenstate as in the beginning but with an additional phase. This phase is often named Berry phase and it can be calculated by performing a line integral of the Berry potential  $A$  along the loop. Based on that, one can define a vector field  $\Omega = \nabla \times A$  named Berry curvature.<sup>52</sup> However, please note, that the Berry phase and the Berry curvature are descriptions based on a semiclassical approach.

One of the earliest instances of Berry phase in solids was reported by Karplus and Luttinger (KL) in 1954.<sup>47</sup> They investigated the AHE in ferromagnetic materials and derived a correction to the electron velocity (anomalous velocity). The concept of Berry phase was not derived yet and the KL theory for the AHE faced strong resistance. Other scattering based mechanisms were thought to be responsible for the AHE in ferromagnetic materials.<sup>53</sup> Later, the KL theory was combined with the Berry phase concept resulting in a widely accepted explanation of the intrinsic AHE.<sup>54,55</sup> The semi classical equations of motion for electrical transport now take the form of:<sup>55</sup>

$$\frac{\partial \vec{x}}{\partial t} = \frac{1}{\hbar} \frac{\partial E_n(k)}{\partial \vec{k}} - \frac{\partial \vec{k}}{\partial t} \times \vec{\Omega}_n(k) \quad (1)$$

$$\hbar \frac{\partial \vec{k}}{\partial t} = -e\vec{E} - e \frac{\partial \vec{x}}{\partial t} \times \vec{B} \quad (2)$$

where  $E_n$  is the Energy of the  $n$ -th band and  $\vec{E}$  is the electric field,  $\vec{B}$  is the magnetic field and  $\Omega_n$  is the Berry curvature of the  $n$ -th band. The second term in Eq. (1) is the velocity correction due to the Berry phase effect. Comparing Eq. (1) and Eq. (2) coined the term magnetic field in momentum space for the Berry curvature. It is possible to calculate the intrinsic anomalous Hall conductivity  $\sigma_{xy}$  arising from the velocity correction in Eq. (1) by integrating the Berry curvature over the Brillouin zone and sum over all occupied bands:<sup>56</sup>

$$\sigma_{xy} = -\frac{e^2}{h} \sum_n \int \frac{d\vec{k}}{(2\pi)^3} f_{n,\vec{k}} \vec{\Omega}_z(n, \vec{k}) \quad (3)$$

where  $f_{n,\vec{k}}$  is the equilibrium Fermi occupation. This formalism is capable of explaining many experimental results for ferromagnetic metals and semiconductors.

The Berry phase concept is closely connected to topological materials. Already Berry realized that the Berry potential is divergent at non-degenerate band touching points and therefore named such touching points diabolic points.<sup>57</sup> In general, topological features in the electronic band structure lead to a large accumulation of Berry curvature and impact the transport response for example by inducing an anomalous velocity.

The Berry phase mechanism for the AHE focusses on electrons driven by an electrical field but the anomalous velocity vanishes in the absence of mechanical forces. Xiao and coworkers derived a formalism showing that the Berry phase effect also influences statistically driven electrons for example thermally induced currents even in the absence of mechanical forces.<sup>58</sup>

In a recent work, Noky and coworkers investigated the subtle difference of how the Berry phase impacts the AHE and its thermomagnetic counterpart the anomalous Nernst effect (ANE).<sup>59</sup> They considered a simple model system with one pair of Weyl points and calculated how the AHE and ANE response depends on the position of the chemical potential. The AHE is maximal when the chemical potential is directly at the Weyl point and decreases strongly if the chemical potential is shifted up or downwards. The ANE response behaves quite differently. It is zero if the chemical potential is directly at the Weyl point and reaches a maximal magnitude (different signs) when the chemical potential is tuned somewhat away from the Weyl nodes. This illustrates how AHE and ANE can be used as complementary tools to study the transport properties in topological materials.

<sup>56</sup> T. Jungwirth et al., Phys. Rev. Lett. **88**, 207208 (2002)

<sup>57</sup> M. V. Berry, in *Chaotic behavior in quantum systems: theory and applications*, edited by G. Casati (Springer US, Boston, MA, 1985), 123–140

<sup>58</sup> D. Xiao et al., Phys. Rev. Lett. **97**, 026603 (2006)

<sup>59</sup> J. Noky et al., Phys. Rev. B **98**, 241106 (2018)





# Microstructure Preparation and Magnetic Properties

## Crystal Structure

$\text{Co}_3\text{Sn}_2\text{S}_2$  belongs to the family of shandites with the generalized formula  $\text{M}_3\text{A}_2\text{Ch}_2$  ( $\text{M} = \text{Co}, \text{Ni}, \text{Rh}, \text{Pd}$ ;  $\text{A} = \text{In}, \text{Sn}, \text{Tl}, \text{Pb}$ ;  $\text{Ch} = \text{S}, \text{Se}$ ).<sup>60</sup> The first high pressure synthesis of many shandites, including  $\text{Co}_3\text{Sn}_2\text{S}_2$ , was reported 1979 by Zabel and coworkers.<sup>61</sup>  $\text{Co}_3\text{Sn}_2\text{S}_2$  crystallizes in the  $R\bar{3}m$  structure and its characteristic features are metallic CoSn layers stacked along the  $c$ -direction in ABC fashion (cp. Figure 4a).<sup>62,63</sup> A very interesting aspect of this structure is the arrangement of the Co atoms within the  $a$ - $b$ -plane. A cut through the  $a$ - $b$ -plane is depicted in Figure 4b featuring a corner sharing Kagome network of Co atoms. Such a Kagome network can exhibit interesting magnetic properties, e.g., frustration between the three lattice sides.

<sup>60</sup> R. Weihrich et al., Z. Anorg. Allg. Chem. **631**, 1463–1470 (2005)

<sup>61</sup> M. Zabel et al., Z. Naturforsch. **34b**, 238–241 (1979)

<sup>62</sup> R. Weihrich et al., Z. Anorg. Allg. Chem. **630**, 1767–1767 (2004)

<sup>63</sup> R. Weihrich and I. Anusca, Z. Anorg. Allg. Chem. **632**, 1531–1537 (2006)

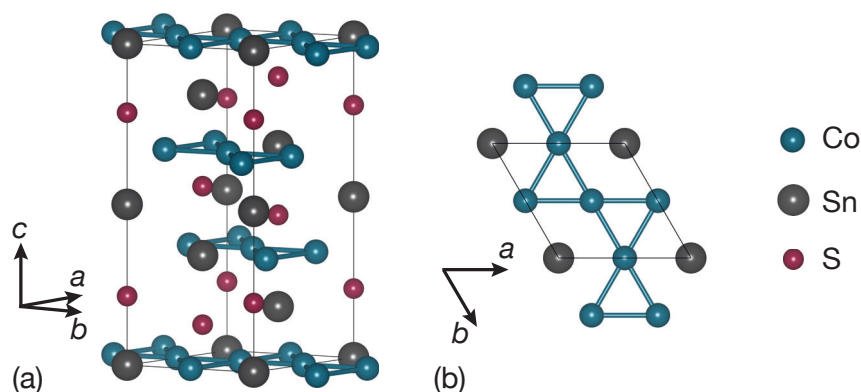


Figure 4: (a) Crystal structure of  $\text{Co}_3\text{Sn}_2\text{S}_2$  in isometric representation. (b) Cut of the  $a$ - $b$ -plane illustrating the Kagome network of Co atoms.

First investigations of the electronic and magnetic properties of  $\text{Co}_3\text{Sn}_2\text{S}_2$  found metallic behavior and Pauli paramagnetism even though a phase transition below 200 K was deduced from the resistivity data.<sup>64</sup> This phase transition is related to ferromag-

<sup>64</sup> S. Natarajan et al., J. Less Common Met. **138**, 215–224 (1988)

<sup>65</sup> Y. S. Dedkov et al., J. Conf. **100**, 072011 (2008)

<sup>66</sup> M. Holder et al., Phys. Rev. B **79**, 205116 (2009)

<sup>67</sup> P. Florian et al., Z. Naturforsch. B. **69**, 55 (2014)

<sup>68</sup> W. Schnelle et al., Phys. Rev. B **88**, 144404 (2013)

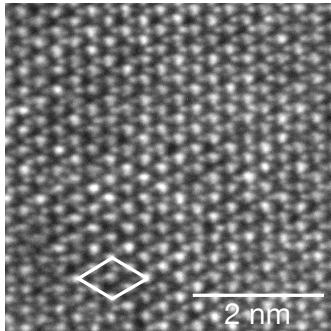


Figure 5: TEM micrograph of the *a-b* plane. The white rhombus indicates one unit cell.

<sup>69</sup> P. Vaquero and G. G. Sobany, Solid State Sci. **11**, 513–518 (2009)

<sup>70</sup> The beam aperture size for FIB preparation is denoted as current to obtain an energy product when combined with the acceleration voltage.

netic ordering at low temperatures with an ordering temperature between 170 K and 175 K. Density functional theory studies and photoemission spectroscopy revealed that ferromagnetic  $\text{Co}_3\text{Sn}_2\text{S}_2$  exhibits a gap in one spin channel and, thus, can be seen as a half-metal.<sup>65,66,67</sup> The half-metallicity paired with the ferromagnetism in  $\text{Co}_3\text{Sn}_2\text{S}_2$  attracted research interest in this compound for potential applications in spintronic devices.<sup>68</sup>

The single crystals of  $\text{Co}_3\text{Sn}_2\text{S}_2$  used in this work to fabricate micro ribbon devices are grown by a self-flux method using Sn as flux. High purity elements (99.99 %) of Co, Sn, S are mixed in the ratio Co:Sn:S of 8:6:86 and placed in an pre-dried alumina crucible. The crucible is sealed in a quartz tube under Ar atmosphere and the reaction mixture is heated to 673 K with a rate of  $100 \text{ K h}^{-1}$ . It is kept at 673 K for the reaction of Sn with S. Afterwards, it is heated to 1323 K with a rate of  $200 \text{ K h}^{-1}$  and homogenized for 6 h. The mixture is cooled to 973 K with  $3.5 \text{ K h}^{-1}$  and the extra flux is removed at 923 K by centrifugation. After cool down to room temperature, the crucible is filled with differently shaped single crystals of  $\text{Co}_3\text{Sn}_2\text{S}_2$ , including thin hexagonal shaped flakes of several hundreds of micrometers in diameter and approximately  $50 \mu\text{m}$  in thickness. Figure 5 depicts a transmission electron microscopy (TEM) micrograph with atomic resolution of the *a-b*-plane recorded on a lamella cut from such a hexagonal flake using a focussed ion beam (FIB). The white rhombus indicates one unit cell within the lattice and the lattice parameter in the plane is determined to 0.54 nm which is comparable to 0.537 nm determined from powder neutron diffraction.<sup>69</sup>

FIB cutting is well suited to prepare microscopic specimen with a defined lateral structure. Thus, FIB cutting is used to cut micro ribbons with a typical size of  $0.3 \times 5 \times 50 \mu\text{m}$  from  $\text{Co}_3\text{Sn}_2\text{S}_2$  single crystals. One needs to consider that the transverse direction of the micro ribbon device is oriented out-of-plane during the FIB preparation. Therefore the hexagonal flake is mounted on a  $90^\circ$  stub with silverpaste and one hexagon edge aligned parallel with the stub surface. This results in the *c*-direction being out of plane in the micro ribbon. In the first step a layer of carbon and Pt is deposited on the surface using a gas injection system and the electron beam at 3 kV and 11 nA.<sup>70</sup> This layer protects the material against excessive damage induced by the Ga-ions. In the next step the rough shape of the micro ribbon is defined by cutting two staircase shaped trenches next to the ribbon into the surface using 30 kV and 21 nA. During this step the micro ribbon is tilted by  $2^\circ$  to account for the beam shape and absorp-



tion. Afterwards, each side of the ribbon is further thinned to the desired thickness of 300 nm to 500 nm. The ribbon starts to bend for thicknesses below 300 nm, effectively limiting thickness to approximately 300 nm.<sup>71</sup> During the thinning the acceleration voltage is kept constant at 30 kV but the current is reduced stepwise to 80 pA. The cutting parameters are summarized in table 1.

In the next step, the protection layer on top of the micro ribbon is cut off with 30 kV, 0.23 nA and an angle of 62°. The same parameters are used to detach the bottom of the ribbon. Figure 6(a) depicts a scanning electron microscopy (SEM) micrograph of the micro ribbon in the crystal after detaching the bottom.

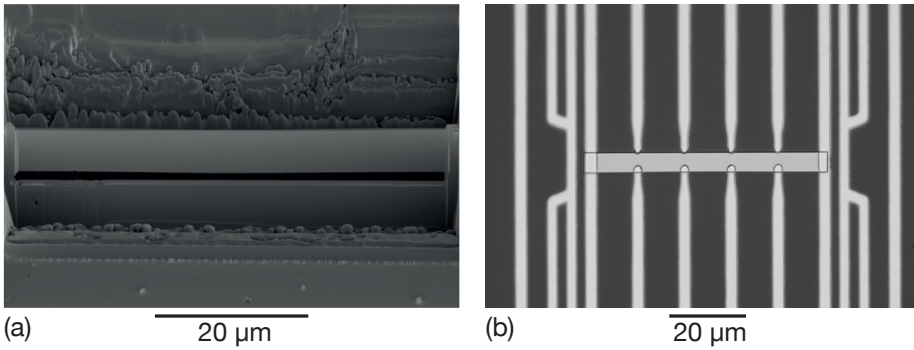


Figure 6: (a) SEM micrograph of the micro ribbon in the host crystal after cutting the bottom side and before cutting the sides. (b) Optical micrograph of a 60 μm long  $\text{Co}_3\text{Sn}_2\text{S}_2$  micro ribbon in the center and the Ti/Pt contacts, thermometers and heaters around it.

In a final step the sides are cut with 30 kV, 0.23 nA and an angle of 62°. The sides are not cut completely, but a thin connection to the host crystal remains to hold the micro ribbon in place. For the lift-out of the micro ribbon the crystal is taken to ambient conditions. The lift-out procedure is performed under a light microscope using a "Kleindiek" micro manipulator and a self-made glass needle. If the micro ribbon adheres to the glass needle it can be transferred onto a 7×8 mm<sup>2</sup> glass substrate.

Laser lithography combined with a lift-off procedure is used to define the contact structure. The sample is baked on a hotplate at 180 °C for 5 min to desorb water from the substrate and, thus, increase the photoresist adhesion. Afterwards, the sample is spin coated with a double layer of photoresist. The coating and baking parameters are summarized in table 2.

A μPG 101 laser writer from Heidelberg Instruments is used to expose the layout. For the exposure 8 mW, 80% and 1×10<sup>17</sup> with an additional filter with ~ 13% transmission is used. The structure is developed in maD331 for 30 s and afterwards visually inspected

<sup>71</sup> This depends on the material and the ribbon length

current	tilt
9 nA	−2°
2.5 nA	−2°
0.79 nA	−1.5°
0.23 nA	−1.5°
0.08 nA	−1.7°

Table 1: Overview of the FIB cutting parameters for subsequent thinning steps.

<sup>72</sup> This denotes the number of passes the writing head moves over the sample and the corresponding writing speed.

	photoresist	spin speed	spin time	bake temp.	bake time
layer 1	LOR3B	6000 rpm	50 s	180 °C	250 s
layer 2	maP1205	4500 rpm	40 s	100 °C	30 s

Table 2: Overview of the photoresists and spin coat parameters used for the bilayer lift-off process.

under a light microscope. The development time is adjusted to ensure a clear undercut in the double layer photoresist. The contact area is cleaned in situ for 2 min in Ar-plasma prior to the sputter deposition of 10 nm Ti and 150 nm Pt as contacts. The lift-off is performed in "Microposit Remover 1165" at 50 °C. The increased lift-off temperature is required since ultrasonication can detach the micro ribbon from the substrate and, thus, must be avoided. This is also the reason for the need of a clear undercut after development. A micrograph of the final device after lift-off is depicted in Figure 6(b). In addition to the longitudinal and transverse sample contacts, the device layout features on chip four-point thermometers and heater lines on both sides of the sample. The device is mounted onto a chip carrier and wire bonded for the transport experiments.

## *Magnetic Properties*

$\text{Co}_3\text{Sn}_2\text{S}_2$  exhibits an interesting magnetic ground state due the layered structure and the Kagome network of Co atoms. The magnetometry data of the single crystals used in this work are recorded using a MPMS7-XL by QuantumDesign with the reciprocating sample option. The data is shown in Figure 7, to compare the single crystals used to fabricate the micro ribbon devices with previous investigations. A single crystal was glued on a  $5 \times 5 \mu\text{m}$  Yttrium-Aluminum-Garnet (YAG) substrate using silverpaste. The diamagnetic background of the YAG has been determined for 220 K where  $\text{Co}_3\text{Sn}_2\text{S}_2$  is paramagnetic and thus a linear background is subtracted from the measurements. The magnetization as a function of temperature measured in field cool with different external magnetic fields along the crystal  $c$ -direction is depicted in Figure 7a.  $\text{Co}_3\text{Sn}_2\text{S}_2$  is paramagnetic for temperatures above 175 K and orders magnetically below, with the net magnetization aligned along the  $c$ -direction. The saturation magnetization is  $69 \text{ kA m}^{-1}$  at 250 mT and 10 K. This is smaller than the previous reports of  $0.3 \mu_{\text{B}}/\text{Co-atom}$  (corresponding to  $75 \text{ kA m}^{-1}$ ). However, the irregular shape of the single crystal leads to a systematic error in the volume determination

and, thus, can be responsible for the apparent deviation from previous measurements.

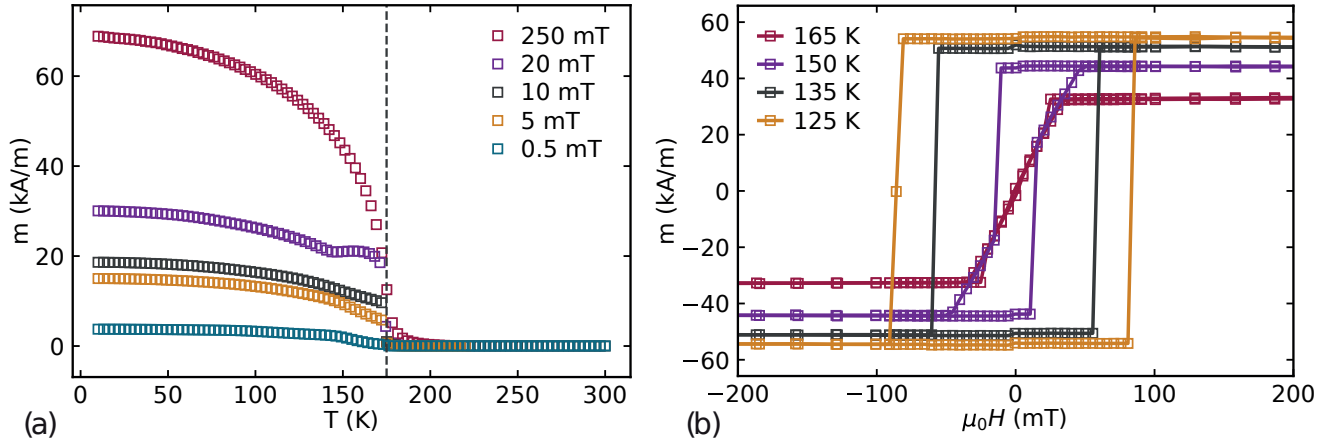


Figure 7: SQUID magnetometry measurements of the magnetization along the  $c$ -direction of a single crystal used to fabricate the micro ribbon devices. (a) Magnetization as a function of temperature for different external fields. (b) Magnetization as a function of the external magnetic field recorded at different base temperatures.

Figure 7b depicts the magnetization as a function of the external magnetic field along the  $c$ -direction for different base temperatures below the critical temperature. A sharp rectangular hysteresis loop develops towards lower temperatures. The easy axis along the  $c$ -direction is consistent with previous investigations of crystals grown by different groups.<sup>73,74</sup> The anisotropy in this compound is very large as the magnetization can not be saturated in the  $a$ - $b$ -plane in a typical SQUID magnetometer with a maximum magnetic field of 7 T.<sup>75,76</sup>

Kassem and coworkers found that the compound behaves comparable to a quasi 2D magnetic system with an easy axis out of plane.<sup>77</sup> They reported an anomalous phase, named A-phase (cp. Figure 8), with very slow spin dynamics directly below the critical temperature. This phase can be identified in measurements of the AC-susceptibility and field / zero field cooled temperature dependent magnetization measurements.<sup>78</sup> The kink in the field cool measurements (cp. Figure 7a) indicates the presence of the A-phase in the single crystals used here. For more details on the extraction of the A-phase region, please see reference 80. It was suggested by Kassem and coworkers that the domain structure in  $\text{Co}_3\text{Sn}_2\text{S}_2$  could be the origin of this A-phase. The domain structure is therefore investigated using magnetooptical Kerr-effect (MOKE) microscopy.

MOKE microscopy is a powerful tool to investigate the domain structure of magnetically ordered systems. The MOKE describes the change of polarization when polarized light interacts with a

- <sup>73</sup> M. A. Kassem et al., J. Crys. Growth **426**, 208–213 (2015)
- <sup>74</sup> W. Schnelle et al., Phys. Rev. B **88**, 144404 (2013)
- <sup>75</sup> M. A. Kassem et al., J. Solid State Chem. **233**, 8–13 (2016)
- <sup>76</sup> W. Yan et al., Solid State Commun. **281**, 57–61 (2018)
- <sup>77</sup> M. A. Kassem et al., J. Phys. Soc. Jpn. **85**, 064706–7 (2016)
- <sup>78</sup> M. A. Kassem et al., Phys. Rev. B **96**, 014429–6 (2017)

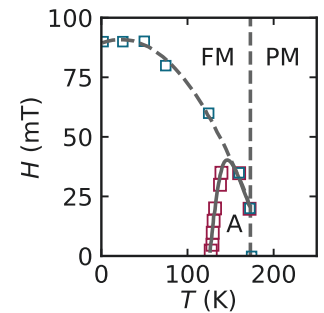


Figure 8: Magnetic phase diagram of  $\text{Co}_3\text{Sn}_2\text{S}_2$ , where A denotes the anomalous phase. The figure is adapted from Kassem et al.<sup>78</sup>

magnetic material. Another common techniques to study magnetic domains are magnetic force microscopy (MFM) and scanning tunneling microscopy (STM). A big advantage of MOKE microscopy over magnetic force microscopy is the short acquisition time of  $\sim 1$  s for MOKE microscopy compared to typically  $\sim 10$  min for MFM. This is especially advantageous for studying the temperature dependence of the domain structure since this requires numerous microscopy images.

In the following the results of MOKE microscopy performed on  $\text{Co}_3\text{Sn}_2\text{S}_2$  will be discussed. The  $\text{Co}_3\text{Sn}_2\text{S}_2$  single crystal is attached to a copper plate using silverpaste and subsequently mounted in a table top cryostat with optical access. This allows to acquire MOKE micrographs below the ordering temperature of 175 K. The micrographs depicted in Figure 9 are acquired in polar mode which is sensitive to the out of plane magnetization (crystalline  $c$ -direction). Panel a-d depict the domain structure without external magnetic after cooling in zero magnetic field.

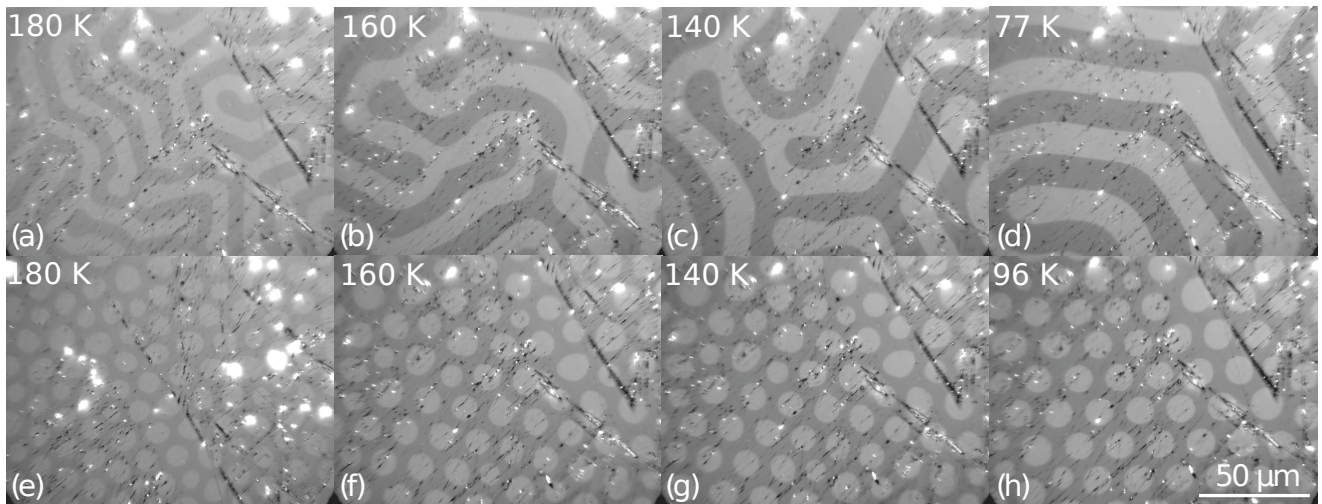


Figure 9: Kerr microscopy images taken in polar mode. (a)-(d) Stripe domains as ground state in zero external magnetic field. (e)-(h) Bubble domains in zero magnetic field, formed after field cooling with 2 mT.

A maze structure is formed (cp. Figure 9a-d), which is the typical domain structure for materials with strong out of plane anisotropy.<sup>79</sup> All micrographs have the same scale and it is visible that the domain width is decreasing with decreasing temperature. This behavior is counterintuitive as the domain width is determined by two energy contributions, which are the exchange energy in the domain wall and the stray field energy. The stray field energy scales with the saturation magnetization, thus this energy term should increase with decreasing temperature (cp. Figure 7a). Assuming the exchange energy is less temperature dependent one would expect a decreasing domain width

<sup>79</sup> F. V. Lisovskii et al., JETP Letters **96**, 596–600 (2013)



towards lower temperatures. However, the opposite behavior is observed in  $\text{Co}_3\text{Sn}_2\text{S}_2$  as it becomes clear from Figure 10 depicting the domain width as function of temperature. The thickness of the flake with  $\sim 50 \mu\text{m}$  can be responsible for the observed behavior as the demagnetization field is smaller in crystals than in thin films.

It is possible to nucleate a bubble domain phase when field cools with 2 mT are performed. This phase is depicted for various temperatures in panel e-h of Figure 9. The bubble domains can be moved in the material and also arranged in a hexagonal lattice by applying an external AC magnetic field. The formation of this phase in the experiments is only possible through field cooling. After saturating the bubble state with an external magnetic field along one direction (single domain state) it is not possible to return to the bubble phase. After removing the external field the sample will return to the maze domain structure as for the zero field cools. The bubble phase remains stable well below 100 K and, thus, expands to much lower temperatures than the A-phase. This indicates that the A-phase is not related to the bubble domain state. Furthermore, such a bubble phase is rather common for magnetic materials with strong out of plane anisotropy.<sup>80</sup>

Additional experiments with Lorentz TEM were performed for high resolution investigation of the magnetic domains. In a recent publication, Sugawara and coworkers report investigations of the domain structure in  $\text{Co}_3\text{Sn}_2\text{S}_2$  with Lorentz microscopy. However, they report experimental difficulties arising from the relatively small saturation magnetization and, therefore, a small Lorentz signal. Consequently, they were only able to observe any signal for samples thicker than 150 nm while using an ultra-high-voltage (1 MV) cold-field-emission cathode. The TEM used in this work has an acceleration voltage of 300 keV and thus limiting the sample thickness to below 150 nm. Due to the aforementioned limitations of the TEM used in the scope of this work, the domain structure could not be reconstructed from the defocus series.

The magnetic properties of the  $\text{Co}_3\text{Sn}_2\text{S}_2$  single crystals used in this work are in agreement with reports from other groups. However, there are still unresolved details e.g. the origin of the A-phase. Furthermore, there is a report of muon spin-rotation experiments indicating a mixed magnetic state with competing anti-ferromagnetic and ferromagnetic order.<sup>81</sup> Lachman and coworkers report an intrinsic exchange bias driven by the frustration within the Kagome lattice.<sup>82</sup> Overall there are still interesting aspects of the rich magnetic state in  $\text{Co}_3\text{Sn}_2\text{S}_2$  to uncover.

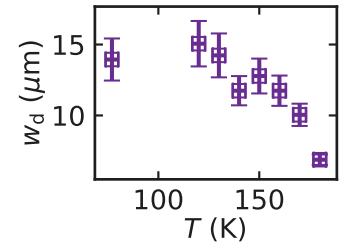


Figure 10: Domain width  $w_d$  as a function of temperature.

<sup>80</sup> A. Hubert and R. Schäfer (Springer, Berlin, Heidelberg, 1998)

<sup>81</sup> Z. Guguchia et al., Nat. Commun. **11**, 559 (2020)

<sup>82</sup> E. Lachman et al., Nat. Commun. **11**, 560, (2020)



# Magnetoresistance and Anomalous Hall Effect

The results of magnetotransport experiments on the micro ribbon device will be discussed in this chapter, in particular focusing on the longitudinal MR and the anomalous Hall effect (AHE). In the first section, two regimes of the longitudinal MR with external magnetic fields along the z-direction are identified and the different contributions are discussed. The second section focusses on the AHE. There, first a short introduction will be given followed by a discussion of the AHE in  $\text{Co}_3\text{Sn}_2\text{S}_2$  micro ribbons with particular emphasis on the band structure contributions.

The following chapter is based on my own publication "Magnetoresistance and Anomalous Hall effect in  $\text{Co}_3\text{Sn}_2\text{S}_2$  micro ribbons".<sup>83</sup> Thus, passages and figures from the following chapter are adopted or directly taken from this publication.

<sup>83</sup> K. Geishendorf et al., Appl. Phys. Lett. **114**, 092403 (2019)

## Longitudinal Magnetoresistance

The MR measurements are performed under isothermal conditions in a cryostat equipped with a variable temperature inset and a superconducting solenoid magnet. An external magnetic field  $\mu_0 H_z$  of up to 9 T is applied along the z-direction. Figure 43 illustrates the measurement geometry. For the measurements a current  $I_x$  of 100  $\mu\text{A}$  is applied along the x-direction while the voltage drop  $V_x$  is recorded along the same direction.

The current density  $\vec{j}$  in a material is connected to the electrical field  $\vec{E}$  with the resistivity tensor  $\rho$ .<sup>84</sup>

$$\begin{pmatrix} E_x \\ E_y \\ E_z \end{pmatrix} = \begin{pmatrix} \rho_{xx} & \rho_{xy} & \rho_{xz} \\ \rho_{yx} & \rho_{yy} & \rho_{yz} \\ \rho_{zx} & \rho_{zy} & \rho_{zz} \end{pmatrix} \begin{pmatrix} j_x \\ j_y \\ j_z \end{pmatrix} \quad (4)$$

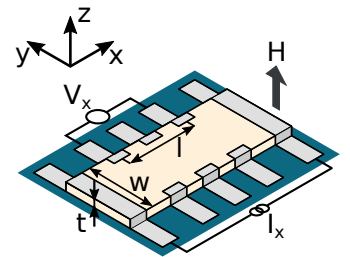


Figure 11: Contacting scheme for measurements of the longitudinal electrical transport response. The typical dimensions are  $0.3 \times 3 \times 50 \mu\text{m}^3$

<sup>84</sup> R. O'Handley (Wiley, 1999)

The longitudinal electrical field is then given by:

$$E_x = \rho_{xx}j_x + \rho_{xy}j_y + \rho_{xz}j_z \quad (5)$$

The defined measurement geometry of the micro ribbon dictates  $j_y = j_z = 0$ , such that one can calculate the longitudinal electric field for a current applied along the micro ribbon as shown in Figure 43 as:

$$E_x = \rho_{xx}j_x \quad (6)$$

To express this in experimental quantities one can replace the current density  $j_x$  with  $I_x/(w \cdot t)$  and the electric field  $E_x$  with  $V_x/l$ :

$$\rho_{xx} = \frac{V_x \cdot w \cdot t}{I_x \cdot l} \quad (7)$$

Here  $w$  is the sample width,  $t$  is the sample thickness and  $l$  is the distance between the voltage probes.

Figure 12 depicts the longitudinal resistivity  $\rho_{xx}$  as a function of temperature.  $\text{Co}_3\text{Sn}_2\text{S}_2$  exhibits a positive temperature coefficient of the resistivity over the full temperature range from 10 K to 300 K. The resistivity increases from  $0.5 \mu\Omega \text{ m}$  to  $4.2 \mu\Omega \text{ m}$ . For

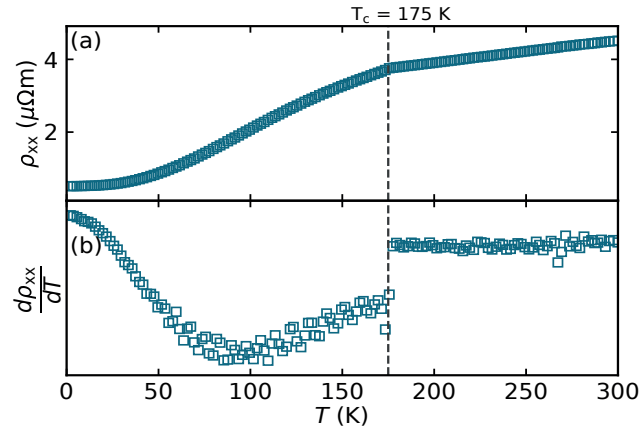


Figure 12: (a) The longitudinal resistivity in zero external magnetic field as function of temperature. The kink in the curve coincides with the magnetic ordering temperature  $T_c$ . (b) The derivative of  $\rho_{xx}$  with respect to the temperature. It exhibits a discontinuity at the ordering temperature  $T_c$ .

$T > T_c$ , the resistivity increases linearly with the temperature, suggesting that the resistivity is governed by electron-phonon interactions in that temperature range.<sup>85</sup> Below 200 K a pronounced change of  $d\rho/dT$  is observed. The discontinuity at 175 K is consistent with the magnetic ordering temperature of  $\text{Co}_3\text{Sn}_2\text{S}_2$ .<sup>86,87,88,89</sup> The alignment of the magnetic moments below  $T_c$  freezes out the spin-disorder contribution to the resistivity and thus increases

<sup>85</sup> T. Kasuya, Prog. Theor. Phys. **16**, 58–63 (1956)

<sup>86</sup> T. Kubodera et al., Physica B: Condens. Matter **378-380**, 1142–1143 (2006)

<sup>87</sup> W. Schnelle et al., Phys. Rev. B **88**, 144404 (2013)

<sup>88</sup> J. Corps et al., Chem. Mater. **27**, 3946–3956 (2015)

<sup>89</sup> M. A. Kassem et al., J. Solid State Chem. **233**, 8–13 (2016)



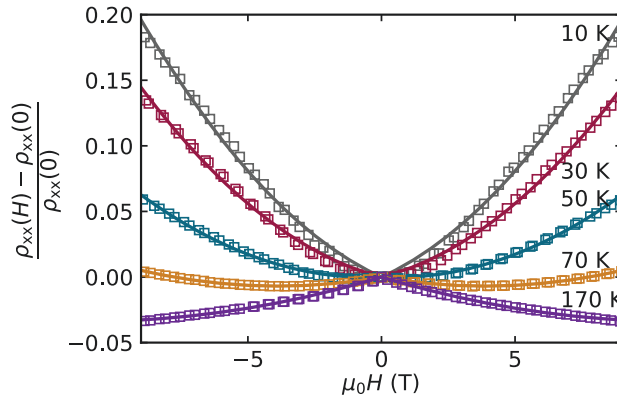


Figure 13: The longitudinal MR for an external magnetic field applied along the  $z$ -direction ( $I \perp H$ ) recorded at different temperatures below the ordering temperature. The open symbols represent the data and the solid lines represent fits to the minimal model given in Eq. 8.

$\partial\rho/\partial T$ . The micro ribbon in this measurement displays a residual resistance ratio ( $\text{RRR} = R(300\text{ K})/R(10\text{ K})$ ) of 6.5, which is comparable to the RRR of 6.8 reported for bulk crystals.<sup>90</sup>

The longitudinal magnetoresistance is obtained from recording  $\rho_{xx}$  during sweeps of the external magnetic field along the  $z$ -direction ( $I \perp H$ ). Figure 13 depicts exemplary MR measurements (open symbols) at different temperatures, where the MR is derived as  $(\rho_{xx}(H) - \rho_{xx}(0))/\rho_{xx}(0)$ . A crossover from negative to positive MR is already visible in the raw data.

The MR is extracted for different field strengths ( $H = 1\text{ T}$  to  $9\text{ T}$ ) as a function of temperature to gain further insight into the different contributions to the MR (cp. Figure 14).  $\text{Co}_3\text{Sn}_2\text{S}_2$  displays a constant negative MR of 2.2 % at 9 T between 110 K and 150 K. A negative MR is expected in ferromagnetic materials for perpendicular magnetic and electric fields as a result of the suppression of spin fluctuations.<sup>91</sup> However, below 110 K a crossover to positive MR is observed. For even lower temperatures the MR increases up to 22.8% at 10 K and 9 T. The Lorentz deflection of charge carriers in an external magnetic field leads to a positive quadratic MR as it is the case for the  $\text{Co}_2\text{Sn}_2\text{S}_3$  micro ribbon at low temperatures.<sup>92</sup> This contribution is proportional to the charge carrier mobility. Semimetals typically exhibit high charge carrier mobilities at low temperatures.<sup>93,94,95</sup> Another possible origin of this large positive MR for temperatures below 50 K is electron-hole resonance. Electron-hole resonance was discussed as an origin for the large and non saturating MR in  $\text{WTe}_2$ ,  $\text{NbP}$  and  $\text{WP}_2$ .<sup>96,97,98</sup> The prerequisite for electron-hole resonance is the presence of both carrier types at the Fermi level in a simi-

<sup>90</sup> E. Liu et al., Nat. Phys. **14**, 1125–1131 (2018)

<sup>91</sup> K. Ueda, Solid State Commun. **19**, 965–968 (1976)

<sup>92</sup> I. M. Lifshitz et al., Zh. Eksperim. i Teor. Fiz. **31** (1956), English translation: Soviet Phys.- JETP **12**, 283 (1961)

<sup>93</sup> J. H. Mangenz et al., Phys. Rev. B **14**, 4381–4385 (1976)

<sup>94</sup> T. Liang et al., Nat. Mater. **14**, 280–284 (2015)

<sup>95</sup> J. Xiong et al., Science **350**, 413–416 (2015)

<sup>96</sup> M. N. Ali et al., Nature **514**, 205–208 (2014)

<sup>97</sup> C. Shekhar et al., Nat. Phys. **11**, 645–649 (2015)

<sup>98</sup> N. Kumar et al., Nat. Commun. **8**, 1642 (2017)

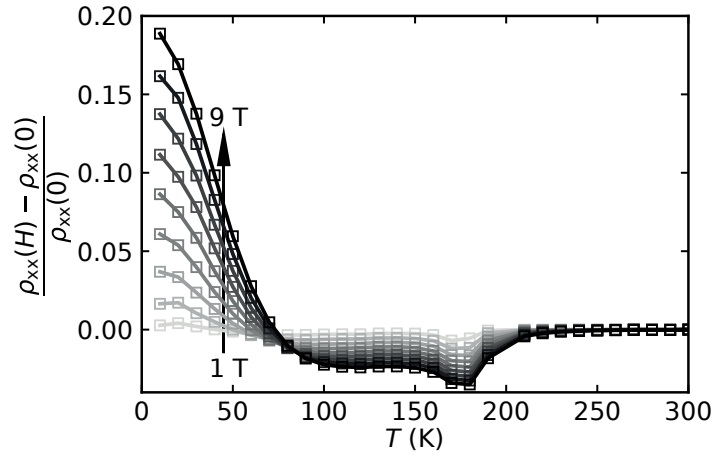


Figure 14: The longitudinal magnetoresistance as function of the temperature extracted for different external magnetic field strength between 1 T and 9 T. Each line represent the magnetoresistance at one given field strength as a function of the temperature (e.g. the black line traces the MR at 9 T between 10 K and 300 K).

lar concentration. In  $\text{Co}_3\text{Sn}_2\text{S}_2$  quantum oscillations of the MR recorded in high magnetic field revealed that a small electron and a small hole pocket are very close to the Fermi level and thus could be responsible for the non saturating MR.<sup>99</sup> From those two contributions, the suppression of spin fluctuations and Lorentz deflection, a minimal model to fit the MR data can be established incorporating a linear negative and a quadratic positive term:

$$\text{MR} = -\alpha|H| + \beta H^2 \quad (8)$$

This model is used to fit the MR sweeps at different temperatures. The solid lines in Figure 13 represent least square fits of Eq. 8 to the raw data. From comparing data and fit it becomes clear that the MR in  $\text{Co}_3\text{Sn}_2\text{S}_2$  can be explained invoking a simple model with a negative term proportional to  $|H|$  and a positive term scaling with  $H^2$ .

One additional feature is the maximum negative MR at the ordering temperature (cp. Figure 14). A maximum of the negative MR at  $T_c$  is also observed in other ferromagnetic compounds due to the significant suppression of critical fluctuations near the ordering temperature.<sup>100</sup> This feature is only apparent in the microstructures presented here, whereas no sharp maximum of the negative MR around  $T_c$  is observed in measurements of bulk crystals. This underlines the importance of systematic MR experiments in microstructures as a function of field strength and temperature to resolve all the details of the MR response in single crystals.

<sup>99</sup> E. Liu et al., Nat. Phys. **14**, 1125–1131 (2018)

<sup>100</sup> Y. Masuda et al., Physica B+C **91**, 291–297 (1977)

## Anomalous Hall effect

Two important contributions to the transverse transport response are the ordinary and anomalous Hall effect. The ordinary Hall effect (OHE) describes the transverse voltage generated by the deflection of charged carriers in a perpendicular magnetic field.<sup>101</sup> The OHE results in a linear change of the transverse resistivity  $\rho_{xy}$  with magnetic field:

$$\rho_{xy} = R_H \cdot \mu_0 H_z \quad (9)$$

where  $R_H$  is the (ordinary) Hall coefficient and  $\mu_0 H_z$  is the external magnetic field along the  $z$ -direction. Soon afterwards, E. H. Hall also discovered that there is an additional contribution to the transverse resistance in ferromagnetic materials. This effect is called AHE. The transverse resistivity  $\rho_{xy}$  in ferromagnetic materials exhibits a second contribution which is independent of the external magnetic field, named anomalous Hall resistivity  $\rho_{xy}^A$  (cp. Figure 15) and another part which is linearly dependent on the magnetic field. Therefore, for ferromagnets, Eq. 9 has to be extended by a term that scales with the magnetization rather than the magnetic field:

$$\rho_{xy} = R_H \cdot \mu_0 H_z + R_A \cdot \mu_0 M_z \quad (10)$$

where  $R_A$  is the anomalous Hall coefficient and  $\mu_0 M_z$  is the projection of the magnetization on the  $z$ -direction. Note that in the experiment, the Hall resistivity  $\rho_{xy}$  is usually recorded, while in theoretical calculations, the Hall conductivity  $\sigma_{xy}$  is the quantity of choice.

Since the experimental discovery of the AHE, different mechanisms have been proposed to account for the magnetization dependent Hall effect. Intense theoretical work supported by a broad range of AHE experiments led to the development of a model including three mechanisms. Nowadays, most of the experiments can be explained in the framework of this model. Figure 16 illustrates schematically the three mechanisms that can be involved in the AHE.

The first mechanism is intrinsic and band structure driven. The intrinsic AHE is based on the anomalous velocity introduced by the Berry curvature  $\vec{\Omega}_n(k)$ .<sup>103</sup> As this mechanism is independent of scattering events one expects it to be independent of the longitudinal conductivity ( $\sigma_{xy}^{\text{int}} \propto \sigma_{xx}^0$ ). The second contribution originates from the side jump mechanism. A wave package will

<sup>101</sup> E. H. Hall, Am. J. Math. **2**, 287–292 (1879)

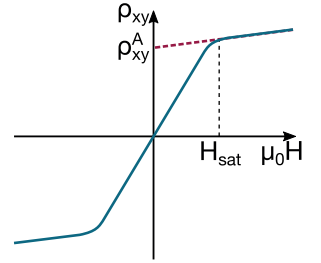


Figure 15: Illustration of the experimental signature of the AHE.

<sup>102</sup> N. Nagaosa et al., Rev. Mod. Phys. **82**, 1539–1592 (2010)

<sup>103</sup>  $\propto \frac{\partial \vec{k}}{\partial t} \times \vec{\Omega}_n(k)$

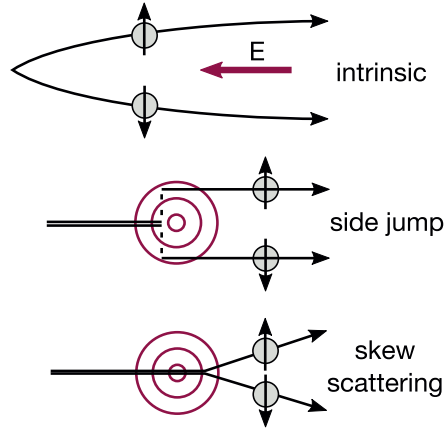


Figure 16: Scheme of the three mechanism involved in the AHE (reproduced from Nagaosa et al.).<sup>102</sup>

<sup>104</sup> J. Smit, *Physica* **24**, 39 – 51 (1958)

<sup>105</sup> L. Berger, *Phys.* **30**, 1141 –1159 (1964)

<sup>106</sup> J. Smit, *Physica* **21**, 877 –887 (1955)

<sup>107</sup> S. Onoda et al., *Phys. Rev. B* **77**, 165103 (2008)

<sup>108</sup> N. Nagaosa et al., *Rev. Mod. Phys.* **82**, 1539–1592 (2010)

<sup>109</sup> T. Miyasato et al., *Phys. Rev. Lett.* **99**, 086602 (2007)

<sup>110</sup> S. Iguchi et al., *Phys. Rev. Lett.* **99**, 077202 (2007)

<sup>111</sup> M. Lee et al., *Phys. Rev. B* **75**, 172403 (2007)

acquire a transverse displacement if it is scattered on a spherical impurity.<sup>104,105</sup> This mechanism is again independent of the scattering rate, as is the intrinsic contribution, even though it is a scattering mechanism ( $\sigma_{xy}^{\text{side-jump}} \propto \sigma_{xx}^0$ ). The last mechanism, contributing to the AHE, is skew scattering. Here, asymmetric scattering directions arise for electrons with opposite spin being scattered at an impurity when including spin orbit coupling.<sup>106</sup> Note that the skew scattering only leads to a transverse signal in the presence of a spin polarization. Otherwise both scattering directions compensate. This mechanism depends directly on the scattering rate and, thus, dominates in the ultra clean limit ( $\sigma_{xy}^{\text{skew}} \propto \sigma_{xx}$ ).<sup>107</sup> The experimentally observed anomalous Hall conductivity constitutes of all three contributions:<sup>108</sup>

$$\sigma_{xy}^A = \sigma_{xy}^{\text{int}} + \sigma_{xy}^{\text{side-jump}} + \sigma_{xy}^{\text{skew}} \quad (11)$$

The anomalous Hall effect appears to follow three different scaling regimes. This becomes apparent when plotting the transverse conductivity as a function of the longitudinal conductivity for multiple materials (cp. Figure 17).

The anomalous conductivity decreases proportionally to  $\sigma_{xx}^{1.6}$  in the bad metal regime with low longitudinal conductivity ( $\sigma_{xx} < 10^4$  (S/cm)). This is depicted exemplarily in Figure 17 for  $\text{Cu}_{1-x}\text{Zn}_x\text{Cr}_2\text{Se}_4$  and  $\text{Nd}_2(\text{MoNb})_2\text{O}_7$ . For the moderately dirty regime ( $10^4 \text{ S/cm} < \sigma_{xx} < 10^6 \text{ S/cm}$ ) it appears that the anomalous Hall conductivity is mostly independent of the longitudinal conductivity. This regime is also named intrinsic regime since  $\sigma_{xy}^{\text{int}}$  is here the dominating contribution. In the ultra clean regime ( $\sigma_{xx} > 10^6 \text{ S/cm}$ )  $\sigma_{xy}$  differs from the constant plateau in the intrinsic regime. One would expect the anomalous Hall conduc-

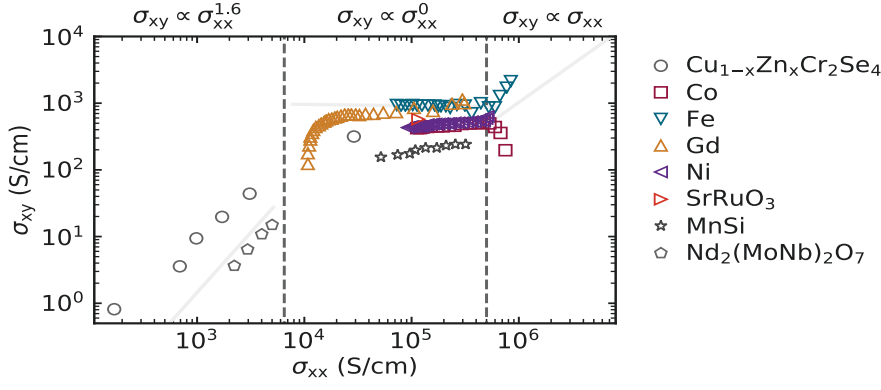


Figure 17: Experimental overview of the AHE in various ferromagnetic materials. Three distinct scaling regimes are marked. The data is taken from Miyasato et al (Gd, Fe, Ni, Co,  $\text{Cu}_{1-x}\text{Zn}_x\text{Cr}_2\text{Se}_4$ ,  $\text{La}_{1-x}\text{Sr}_x\text{CoO}_3$ ,  $\text{SrRuO}_3$ ), Iguchi et al. ( $\text{Nd}_2(\text{MoNb})_2\text{O}_7$ ) and Lee et al. (MnSi).<sup>109–119</sup> The bright grey lines represent the model from Onoda et al.<sup>108</sup>

tivity to scale directly with the longitudinal conductivity as the skew-scattering is the predominant mechanism. However, also decreasing Hall conductivities are observed. Overall, experimental results for the AHE in the ultra clean region are rather limited. Nevertheless, it is interesting that the AHE in a broad spectrum of materials follows this universal scaling behavior depicted in Figure 17.

$\text{Co}_3\text{Sn}_2\text{S}_2$  is reported to have Weyl nodes only 60 meV below the Fermi level.<sup>112</sup> Thus the Berry curvature associated with such band crossing points can strongly enhance the AHE. Measurements of the anomalous Hall resistivity in  $\text{Co}_3\text{Sn}_2\text{S}_2$  are performed to investigate the magnitude of the AHE and its origin. The schematic measurement setup is illustrated in Figure 18. Here, the transverse voltage drop  $V_y$  is recorded while applying a constant current  $I_x$  along the  $x$ -direction and sweeping the magnetic field  $\mu_0 H_z$  along the  $z$ -direction. Similar to Eq. 5 and Eq. 6 one can express the transverse electrical field by:

$$E_y = \rho_{yx} j_x \quad (12)$$

Again, this can be expressed in experimental quantities :

$$\rho_{yx} = -\rho_{xy} = \frac{V_y \cdot t}{I_x} \quad (13)$$

Figure 19 depicts  $\rho_{yx}$  traces for magnetic field sweeps along the  $z$ -direction. The anomalous Hall resistivity is extracted by linear fitting of the high field part ( $\mu_0 H_z > 5\text{T}$ ) and determining the intercept ( $\rho_{yx}^A$ ) of the linear fit with the ordinate (as can be schematically seen in Figure 15). This corresponds to the anomalous Hall

<sup>112</sup> Q. Xu et al., Phys. Rev. B 97, 235416 (2018)

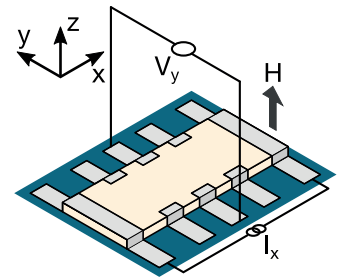


Figure 18: Contacting scheme for measurements of the transverse electrical transport response.

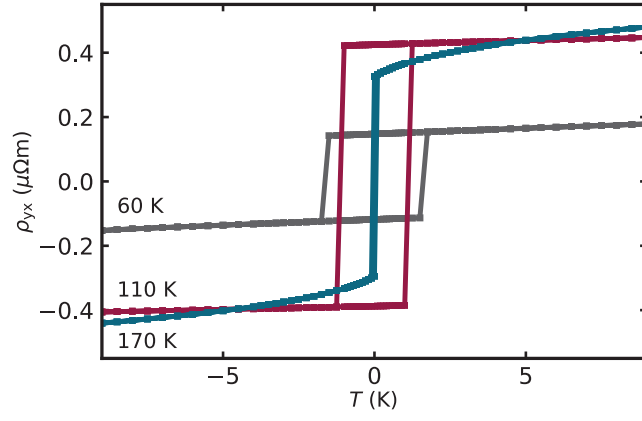


Figure 19: Exemplary Hall resistivity as a function of the magnetic field, recorded for 60 K, 110 K and 170 K.

resistivity arising from the saturation magnetization without any external magnetic field. Offsets caused by, e.g., non-symmetric contact placement are corrected by antisymmetrization of  $\rho_{yx}^A$  as:

$$\rho_{yx}^A = \frac{\rho_{yx}^A(B) - \rho_{yx}^A(-B)}{2} \quad (14)$$

Above 220 K,  $\rho_{yx}$  only depends linearly on the magnetic field as expected for the OHE, not shown here. For lower temperatures, a nonlinear Hall contribution emerges, resulting in s-shaped Hall traces and, thus, a finite  $\rho_{yx}^A$ . The extracted  $\rho_{yx}^A$  is depicted in Figure 20a. The anomalous Hall resistivity is zero for temperatures above 220 K and increases strongly for temperatures below, reaching a maximum of  $0.5 \mu\Omega m$  at 140 K. For temperature below 140 K  $\rho_{yx}^A$  decreases again but does not vanish. Note, that the anomalous Hall effect becomes finite already in the paramagnetic regime as the magnetic susceptibility of the compound increases in the vicinity of the ordering temperature.

In typical experiments  $\rho_{yx}$  is recorded while in theoretical calculations  $\sigma_{yx}$  is the quantity of choice. Assuming that  $\rho_{xx} = \rho_{yy}$  and using  $\rho_{xy} = -\rho_{yx}$  one can express the conductivity  $\sigma$  (for the 2D case) as follows:

$$\sigma = \rho^{-1} = \frac{1}{\det \rho} \cdot \text{adj} \rho = \frac{1}{\rho_{xx}^2 + \rho_{xy}^2} \begin{pmatrix} \rho_{xx} & -\rho_{xy} \\ \rho_{xy} & \rho_{xx} \end{pmatrix} \quad (15)$$

To evaluate the microscopic mechanism involved in the AHE, it is helpful to study the evolution of  $\sigma_{yx}^A$  with  $\sigma_{xx}$ . Both quantities are calculated according to Eq. 15 and the result is depicted in Figure 20b.  $\text{Co}_3\text{Sn}_2\text{S}_2$  exhibits a plateau of  $\sigma_{yx}^A$  for conductivities  $\sigma_{xx} > 3700 \text{ S/cm}$ . Such a plateau is characteristic for the intrinsic



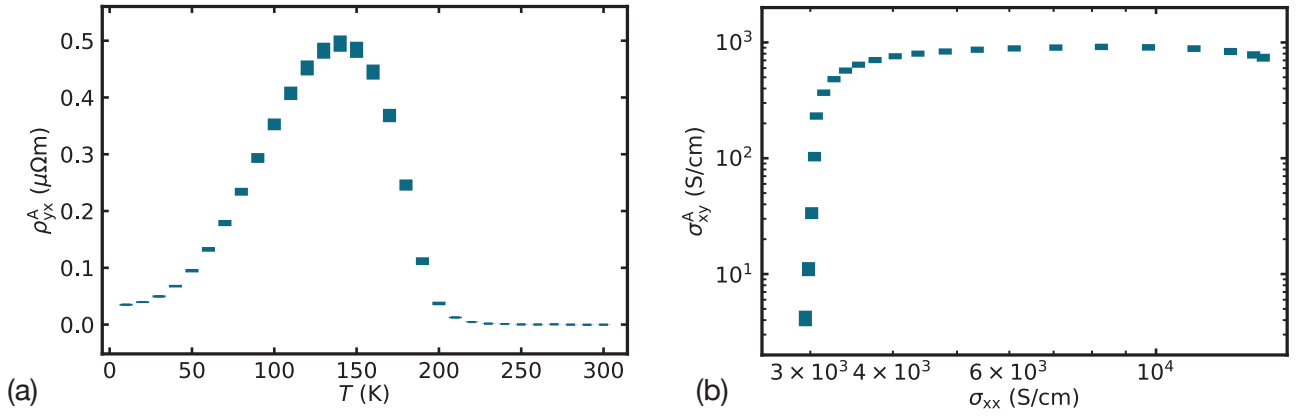


Figure 20: (a) Anomalous Hall resistivity extracted from Hall traces recorded at temperatures between 10 K and 300 K. (b) Anomalous Hall conductivity as function of the longitudinal conductivity. The plateau of  $\sigma_{xy}^A$  indicates the intrinsic origin of the AHE in  $\text{Co}_3\text{Sn}_2\text{S}_2$ . Note that the bar height corresponds to the error of the given quantity calculated from standard deviations and Gaussian error propagation.

AHE contribution or the side-jump mechanism. It is possible to calculate the anomalous Hall conductivity  $\sigma_{xy}$  from the band structure by integrating the Berry curvature over the Brillouin zone and sum all occupied bands:<sup>113</sup>

$$\sigma_{xy} = -\frac{e^2}{h} \sum_n \int \frac{d\vec{k}}{(2\pi)^3} f_{n,\vec{k}} \vec{\Omega}_z(n, \vec{k}) \quad (16)$$

where  $\vec{\Omega}_z(n, \vec{k})$  is the Berry curvature associated with each band and  $f_{n,\vec{k}}$  is the equilibrium Fermi occupation factor. The magnitude of the AHC depends on the position of the chemical potential within the material. Figure 21 depicts the AHC as a function of the energy shift of the chemical potential away from the Fermi level of the undoped material, calculated following Eq. 16.<sup>114</sup> According to the calculations the intrinsic contribution in the undoped compound should be in the order of 1000 S/cm. This is in good agreement with the experimental value depicted in Figure 20b.

It is difficult to distinguish between side-jump and intrinsic contribution, since they follow the same scaling behavior. However, the magnitude of the intrinsic contribution is usually much larger compared to the side-jump contribution.<sup>115</sup> This and the good agreement with the theoretical calculation of the AHC lead to the conclusion that the large AHE in  $\text{Co}_3\text{Sn}_2\text{S}_2$  is dominated by the intrinsic contribution and arises from the complex band structure of this compound.

The Kagome network of Co-atoms in  $\text{Co}_3\text{Sn}_2\text{S}_2$  paired with the out of plane magnetization makes this compound a good plat-

<sup>113</sup> T. Jungwirth et al., Phys. Rev. Lett. **88**, 207208 (2002)

<sup>114</sup> E. Liu et al., Nat. Phys. **14**, 1125–1131 (2018)

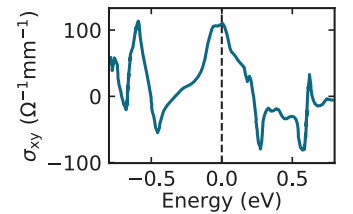


Figure 21: AHC calculated as a function of the chemical potential.

<sup>115</sup> N. Nagaosa et al., Rev. Mod. Phys. **82**, 1539–1592 (2010)

form for the realization of the quantum anomalous Hall effect (QAHE). As demonstrated here for micro ribbon devices patterned from high quality single crystals,  $\text{Co}_3\text{Sn}_2\text{S}_2$  exhibits a very large AHE arising from topological protected band crossings. As such, one can argue that this presents an experimental step towards the realization of the quantum anomalous Hall effect at intermediate temperatures.

Another important aspect of the AHE experiments is the demonstration of the predictive power of the Berry curvature. The Berry curvature is straight forward to compute and can thereby be calculated for many compounds. The robust connection of Berry curvature and intrinsic AHE, thus, opens a way towards the identification of more compounds with large AHE.



# Anisotropic Magnetoresistance

It is generally accepted that a magnetoresistive response can be anisotropic, namely dependent on the direction of the applied external magnetic field or the direction of the magnetization. Any such anisotropic magnetoresistive response will hereafter be referred to as AMR. For example, the resistivity in polycrystalline ferromagnetic thin films depends on the angle between magnetization and current.  $(\rho_{\parallel} - \rho_{\perp})/\rho_{\perp}$  of the non-crystalline AMR is usually in the order of 1-4 % and has achieved technological relevance in magnetic field sensors.<sup>116</sup> However, AMR can also be used to study fundamental properties of a system. Charge currents are coupled to the magnetization of a material via the spin orbit interaction. Consequently, AMR measurements can be used to probe the spin structure in transport experiments. In the following, the MR and its anisotropy in  $\text{Co}_3\text{Sn}_2\text{S}_2$  microstructures will be examined for rotations of the external magnetic field in three orthogonal rotation planes.

## AMR near the magnetic transition temperature

The three orthogonal rotation planes are depicted schematically in the first row (a-c) of Figure 23. The experiments are performed in a cryostat equipped with a variable temperature insert and three superconducting magnets allowing to apply an external magnetic field  $\mu_0 H \leq 2\text{T}$  in any spatial direction. Figure 23d-f depict the longitudinal resistivity  $\rho_{xx}$  recorded during the rotation of  $\vec{H}$ . A strong modulation of  $\rho_{xx}$  is observed in both out-of-plane rotations (panels e and f). The modulation has 180°-symmetry. For increasing external magnetic fields along the z-direction a decrease in resistivity is observed. This is in agreement with the MR reported in the previous chapter for a magnetic field sweep along the z-direction at 170 K (cp. Figure 22). However,  $\rho_{xx}$  increases when the magnetic field is rotated into the  $x$ - $y$ -plane

<sup>116</sup> T. McGuire and R. Potter, IEEE T.Magn. **11**, 1018–1038 (1975)

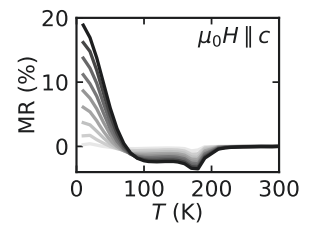


Figure 22: MR as a function of temperature for external magnetic field between 1 T and 9 T.

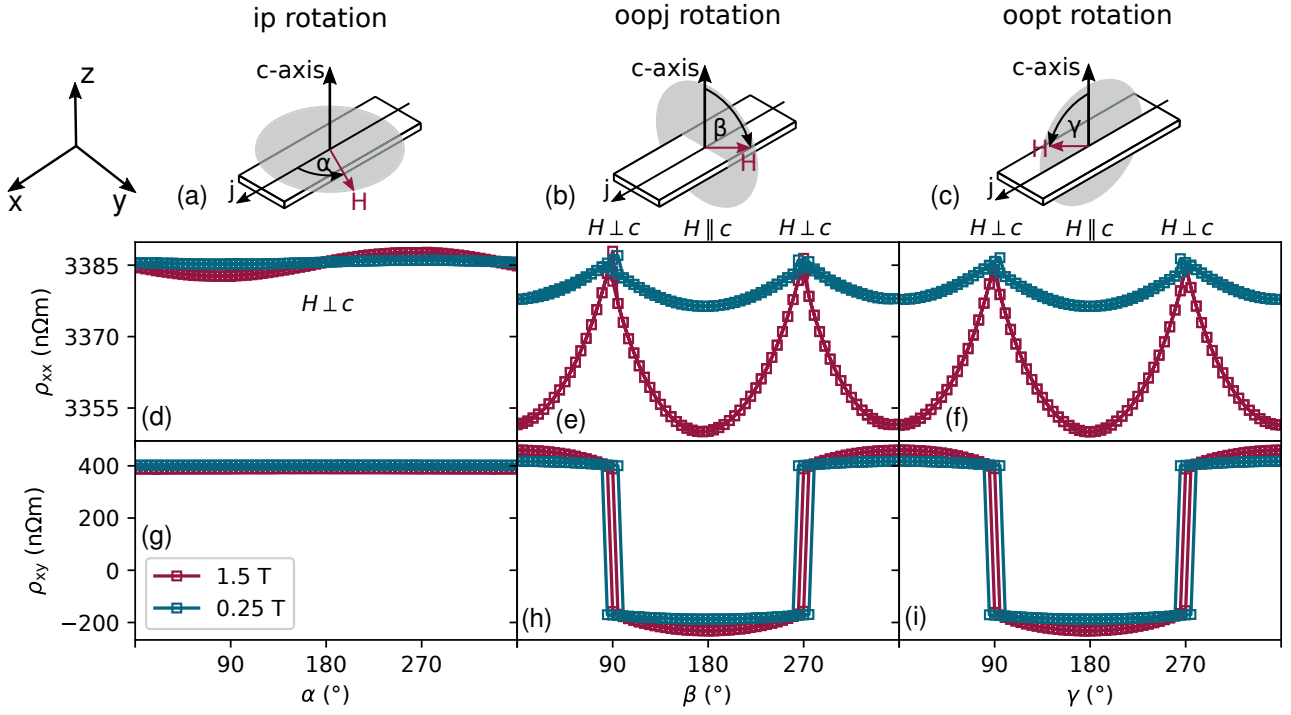


Figure 23: (a)-(c) Schematic representation of the three orthogonal rotation planes around three distinguished directions, namely the surface normal  $n \parallel z$ , the current direction  $j \parallel x$  and transverse direction  $t \parallel y$ . (d)-(f) Longitudinal resistivity  $\rho_{xx}$  recorded for rotations of an external magnetic field of  $\mu_H = 0.25$  T and 1.5 T at 170 K. (g)-(i) Corresponding transverse resistivity  $\rho_{xy}$ . The solid lines are a guide to the eye.

and is maximum for  $H \perp z$ . Here no significant change of the resistivity can be observed when increasing the external magnetic field. The steps in the transverse resistivity  $\rho_{xy}$  depicted in Figure 23h-i show the sharp switching of  $\vec{M}$  around  $90^\circ$  and  $270^\circ$ . The magnetic switching occurs along the crystalline  $c$ -direction, since it is the easy direction of  $\text{Co}_3\text{Sn}_2\text{S}_2$ . The steps arise from the anomalous Hall effect governed by  $\vec{M}$  and their height is, thus, independent of the magnitude of  $\vec{H}$ . Between the switching an additional contribution arises from the projection of  $\vec{H}$  on the  $z$ -direction. This transverse effect stems from the ordinary Hall effect i.e. it is increasing with increasing external magnetic field as can be seen by the more pronounced  $\cos(\beta, \gamma)$  contribution in Figure 23h and i. The step from the anomalous Hall effect is absent in the ip-rotations as  $\vec{M}$  does not switch from  $z$  to  $-z$  or vice versa. Also no modulation due to the ordinary Hall effect is observed in the ip-rotation as  $\vec{H}$  is never perpendicular to both  $x$  and  $y$  at the same time.

Please note that the sinusoidal modulation in Figure 23d can originate from a misalignment between the  $c$ -axis and the  $z$ -direction. A tilt of the  $c$ -axis along the  $y$ -direction for example would give rise to sinusoidal modulation with its extreme

at  $90^\circ$  and  $270^\circ$ . Furthermore, the minimum expected at  $180^\circ$  in Figure 23e is shifted by approximately  $5^\circ$ , which is in good agreement with the proposed misalignment. This misalignment can either originate from a misalignment during the FIB preparation or a misalignment of the sample within the chip carrier.

The  $z$ -direction appears to be the relevant direction for the AMR and, thus, suggests the crystalline  $c$ -axis to be the relevant axis for the AMR. To test this hypothesis, the same measurements are performed in a device, where the  $c$ -axis is not parallel to the  $z$ -direction but parallel to the  $y$ -direction. Figure 24d-f depict  $\rho_{xx}$  recorded for rotations of  $\mu_0 H_z = 1.5$  T in the planes depicted in panel a-c. A very similar modulation of  $\rho_{xx}$  is observed in

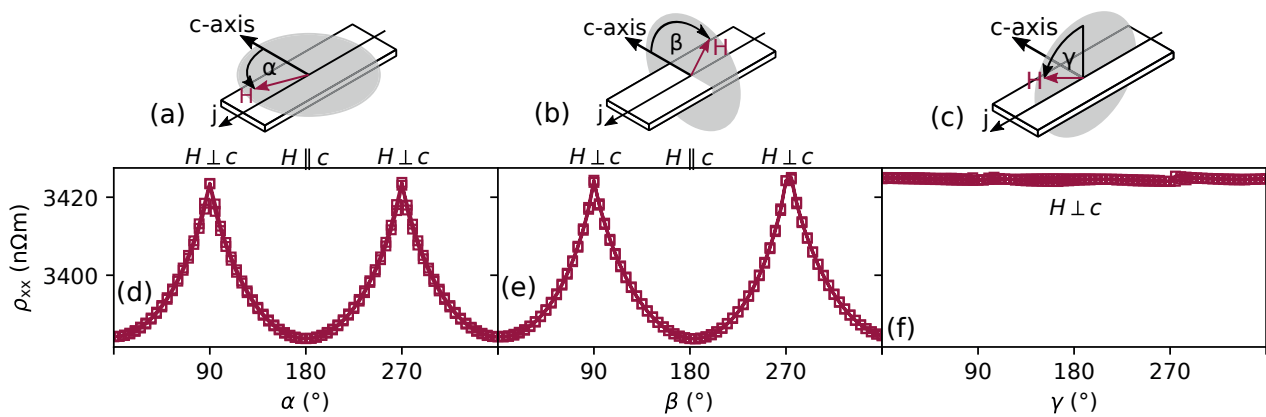


Figure 24: (a)-(c) Schematic representation of the three orthogonal rotation planes around three distinguished directions, namely the surface normal  $n \parallel z$ , the current direction  $j \parallel x$  and transverse direction  $t \parallel y$ . (d)-(f) Longitudinal resistivity  $\rho_{xx}$  recorded for rotations of an external magnetic field of  $\mu_H = 1.5$  T at 170 K.

this sample. However, the distinct direction is no longer the  $z$ -direction, but the  $y$ -direction along which the  $c$ -axis is oriented. Therefore, it can be concluded that the  $c$ -axis is relevant for the effect inducing the modulation of  $\rho_{xx}$  in the rotations of the external magnetic field.

The modulation of  $\rho_{xx}$  in Figure 23e and f appears to scale with the magnitude of  $\vec{H}$  for  $\vec{H} \parallel c$ . If the effect responsible for this modulation would only depend on e.g. the projection of  $\vec{H}$  on  $z$ , then one would expect a  $\sin^2$ -shaped modulation. However, this is not the case. The magneto-crystalline anisotropy in  $\text{Co}_3\text{Sn}_2\text{S}_2$  favors the  $c$ -axis as its easy direction. Consequently, external magnetic fields larger than the anisotropy field are needed to rotate the magnetization coherently with the external magnetic field away from the  $c$ -axis. Thus, magnetic fields much larger than 7 T are required (approximately 25 T at 10 K).<sup>117</sup> For small external magnetic fields ( $\mu_0 H < 2$  T),  $\vec{M}$  can only be slightly tilted

<sup>117</sup> M. A. Kassem et al., J. Solid State Chem. **233**, 8–13 (2016)

away from the  $c$ -axis during the rotation until it switches to the opposite direction. The observed modulations of  $\rho_{xx}$  in Figure 23e and f resemble the modulation expected of  $M_z$  for such rotations in the presence of a strong magneto-crystalline anisotropy. This indicates that the effect responsible for the AMR depends on both, the external magnetic field and the magnetization.

## Magnon Magnetoresistance

In the following the magnon magnetoresistance (MMR) is discussed as possible origin of the observed AMR. The MMR depends on the change of magnon-electron scattering through changes in the magnon population.<sup>118</sup> The theory is based on the assumption that scattering between an  $s$ - and  $d$ -band electrons requires magnons with wave vectors exceeding the distance of the two Fermi surfaces.<sup>119</sup> Thus, the probability for spin-flip scattering between the two bands is closely related to the energy spectrum of the magnon modes. The dispersion relation of long-wavelength magnon modes has a quadratic form:<sup>120</sup>

$$E(q) = Dq^2 + g\mu_B B_t \quad (17)$$

where  $D$  is the exchange stiffness constant,  $g$  is the  $g$ -factor,  $\mu_B$  is the Bohr magneton and  $B_t$  is the total magnetic flux including the contribution from the anisotropy.<sup>121</sup>  $g\mu_B B_t$  in Eq. 17 accounts for a gap in the magnon dispersion. At a given temperature one can reduce or increase the maximal wave vector of magnon modes attainable by increasing or decreasing the external magnetic field. Increasing the external magnetic field increases the gap in the magnon dispersion and thus decreases the number of accessible magnon modes. Decreasing the number of attainable magnon modes in turn leads to a decreasing electron-magnon scattering and consequently to a decrease in resistivity. This effect reproduces the development of  $\rho_{xx}$  at  $\vec{H} \parallel c$  for increasing magnitude of  $\vec{H}$ . However, if the reduction of  $\rho_{xx}$  is proportional to  $B_t$ , also a decrease in resistivity is expected for  $\vec{H} \perp c$ . This behavior was not observed, the resistivity appears independent of  $\vec{H}$  for  $\vec{H} \perp c$ . A possible explanation for this disagreement is that the external field does not directly modify the magnon population. The measurements depicted in Figure 23 suggest that only the projection of  $\vec{H}$  on  $\vec{M}$  gives rise to the MMR. Consequently, the MMR has the form  $\propto \vec{M} \cdot \vec{H}$ . This can be understood considering that the magnon modes are only suppressed if the external magnetic field

<sup>118</sup> B. Raquet et al., Phys. Rev. B **66**, 024433 (2002)

<sup>119</sup> D. A. Goodings, Phys. Rev. **132**, 542–558 (1963)

<sup>120</sup> G. R. Taylor et al., Phys. Rev. **165**, 621–631 (1968)

<sup>121</sup> A. P. Mihai et al., Phys. Rev. B **77**, 060401 (2008)

is pointing along the magnetization. Therefore, a vanishing MMR is expected for  $\vec{M} \perp \vec{H}$ , which is the case for  $\vec{H} \perp c$  assuming that the anisotropy along the  $c$ -axis is strong enough that  $\vec{M}$  remains approximately parallel to  $c$  for small fields ( $\mu_0 H < 2$  T). This is consistent with the observation that  $\rho_{xx}$  for  $\vec{H} \perp c$  does not depend on the magnitude of  $\vec{H}$ . Therefore, it can be concluded, that the MMR in combination with a strong uniaxial anisotropy, as it is present in  $\text{Co}_3\text{Sn}_2\text{S}_2$ , can lead to an AMR effect, where the easy axis of the magnetization is the relevant direction.

The appearance of MMR is not restricted to the ferromagnetic phase. It can also occur in the paramagnetic phase when the external magnetic field partially aligns the magnetic moments. The net magnetization is only sizable for very large magnetic fields or sufficiently large susceptibility, as it is the case for temperatures a few degrees above the ordering temperature. This is the case for  $\text{Co}_3\text{Sn}_2\text{S}_2$  at 180 K, which is 5 K above the ordering temperature. Therefore,  $\rho_{xx}$  is recorded for rotations of the external magnetic field at 180 K to investigate whether the AMR prevails in  $\text{Co}_3\text{Sn}_2\text{S}_2$  in the paramagnetic regime. The results are depicted in Figure 25.

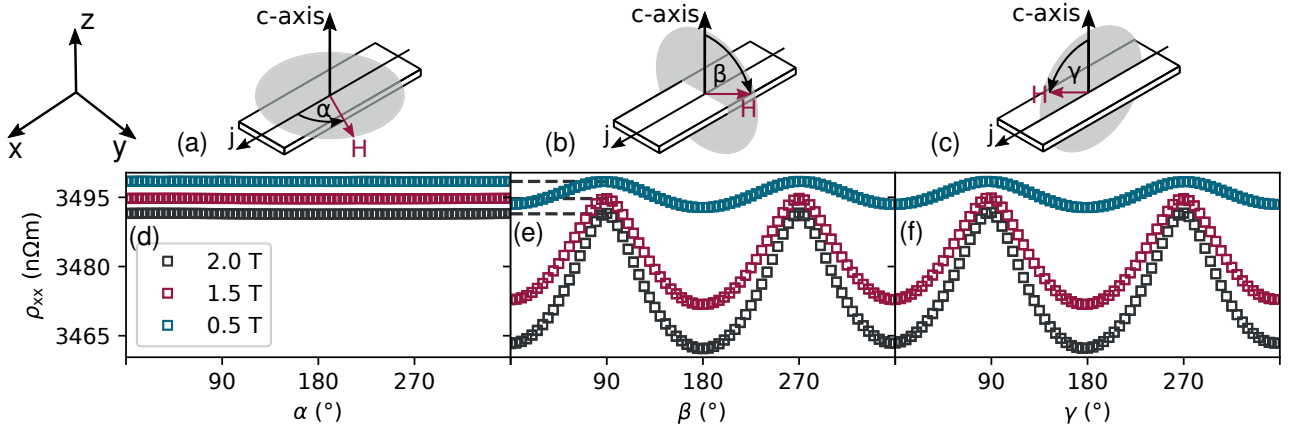


Figure 25: Longitudinal resistivity  $\rho_{xx}$  recorded in the paramagnetic phase at 180 K for the ip (d), oopj rotation (e) and oopt rotation (f). A decrease of the resistivity with increasing external field but no anisotropy is observed in the ip rotations. The levels from (d) correspond to the values in (e) and (f) observed at  $90^\circ$  and  $270^\circ$  where the external magnetic field is parallel to the  $y/x$ -direction.

The in-plane rotations (cp. Figure 25a) of  $\mu_0 H = 0.5$  T, 1.5 T and 2 T exhibit three horizontal lines at different resistivity levels.  $\rho_{xx}$  is isotropic for the in-plane rotations and a decrease of the resistivity level can be observed with increasing external magnetic field. The dashed lines in Figure 25b indicate that the resistivity levels from the in-plane rotations match the resistivity for  $90^\circ$  and  $270^\circ$  in the oopj rotation with the same magnetic field.  $\rho_{xx}$

is not constant for the oopj rotation but a modulation is visible, indicating the presence of AMR. The resistivity is again, as for the measurements in the ferromagnetic phase, minimal for  $\vec{H} \parallel c$  and increases when  $\vec{H}$  is rotated towards  $\vec{H} \perp c$ . However, contrary to the ferromagnetic phase, the resistivity for  $\vec{H} \perp c$  is not independent of the magnitude of  $\vec{H}$  but decreases with increasing magnetic field.

The magnetization in the paramagnetic phase is induced by the external magnetic field, such that both are parallel at all times. Consequently it is possible to rotate the magnetization into the  $x$ - $y$ -plane in this experimental setup (other than at 170 K, which is depicted in Figure 23). Therefore,  $\vec{M} \cdot \vec{H}$  is always finite for  $H > 0$ , leading to MMR for all magnetic field orientations. In the paramagnetic phase the MMR is not expected to be linear in the magnetic field since the magnetization itself is a function of the external magnetic field. The magnetization is given by:<sup>122</sup>

$$M(H) = \chi(H)H \quad (18)$$

where  $\chi(H)$  is the magnetic field dependent susceptibility. Therefore, one expects the MMR for  $\vec{M} \parallel \vec{H}$  to be proportional to:

$$\text{MMR} \propto M(H) \cdot H = \chi(H)H^2 \quad (19)$$

Figure 26 depicts the change of the longitudinal resistivity  $\Delta\rho_{xx}$  for magnetic field sweeps along the  $y$ - and  $z$ -direction. For small magnetic fields the susceptibility can be approximated to be constant. Therefore  $M$  increase increases linearly ((i.e.  $\chi(H) = \text{const.}$ ) with  $H$  and the MMR is proportional to  $H^2$ . The open symbols in Figure 26a represent the data points, whereas the dashed blue line represents a fit of  $\Delta\rho_{xx} = a \cdot H^2$ . Good agreement between the fit and the data points can be achieved, indicating that the linear approximation of  $M(H)$  is justified. The negative MR for the magnetic field sweep along  $y$  can be consistently explained invoking the MMR. However, the quadratic fit does not match the magnetic field sweep along the  $z$ -direction (cp. blue dashed line and open symbols in 26b). This can be explained with an anisotropic susceptibility.  $\chi(H)$  can no longer be approximated to be constant in this particular field range and crystal direction.

The Langevin-function  $L(x) = \coth(x) - 1/x$  can be used to approximate the magnetization of a paramagnet in an external magnetic field by introducing the Langevin parameter ( $\zeta \propto \mu_0 H$ ).<sup>122</sup> The magnetization  $M$  of the paramagnet is proportional to  $L(\zeta)$ :

$$M(H) = a \cdot L(\zeta) \quad (20)$$

<sup>122</sup> R. O'Handley (Wiley, 1999)



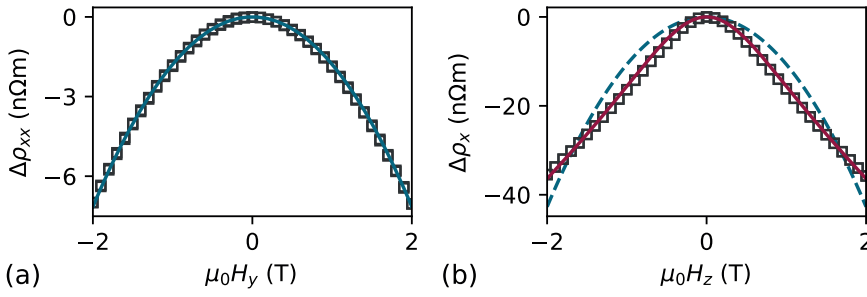


Figure 26: Longitudinal resistivity change  $\Delta\rho_{xx}$  at 180 K for external magnetic fields applied along (a) the  $y$ -direction and (b) the  $z$ -direction (open symbols). The dashed blue lines represent fits to  $\Delta\rho_{xx} = a \cdot H^2$ . The solid red line in (b) represents a fit using Eq. 21.

where  $a$  is a proportionality factor. Consequently,  $M(H)$  in Eq. 19 can be replaced by Eq. 20, resulting in:

$$\Delta\rho_{xx}(H) = a \cdot \left( \coth(b \cdot H) - \frac{1}{b \cdot H} \right) \cdot H \quad (21)$$

where  $a$  and  $b$  are the fit parameters. The fit of Eq. 21 for  $\Delta\rho_{xx}$  recorded during magnetic field sweeps along the  $z$ -direction is depicted by the solid red line. Eq. 21 achieves better agreement with the data compared to the quadratic fit (dashed blue line).

It was discussed in the previous chapter that the transverse resistivity is composed of one term proportional to  $H$  (ordinary Hall effect) and one term proportional to  $M$  (anomalous Hall effect):

$$\rho_{yx} = R_H \mu_0 H + R_A \mu_0 M \quad (22)$$

Figure 27 depicts  $\rho_{yx}$  for a sweep of the external magnetic field along the  $z$ -direction. The s-shaped trace indicates the finite magnetization induced by the magnetic field. Again, one can replace  $M$  in Eq. 22 using Eq. 20:

$$\rho_{yx} = R_H \mu_0 H + R_A \mu_0 \left( \coth(b \cdot H) - \frac{1}{b \cdot H} \right) \quad (23)$$

where  $R_H$  and  $R_A$  are the fit parameters. The parameter  $b$  is extracted from the fit of Eq. 21 (cp. red solid line in Figure 26b). A fit of Eq. 23 is represented by the solid red line in Figure 27. Here, good agreement between Eq. 23 and  $\rho_{yx}$  can be achieved. This indicates, that the approximation of  $M(H)$  with the Langevin-function is appropriate. Therefore, the negative MR in both magnetic field sweeps can be explained invoking the MMR. Furthermore, the AMR for the oopj rotation originates from the anisotropy of the susceptibility. The anisotropy of the

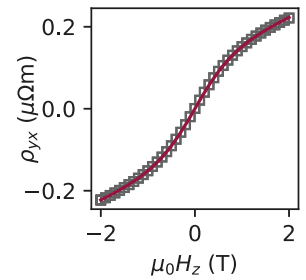


Figure 27:  $\rho_{yx}$  at 180 K (open symbols) and fit to Eq. 23 (solid line).

<sup>123</sup> J. Mathon and E. P. Wohlfarth, Proc. R. Soc. London. Ser. A **302**, 409–418 (1968)

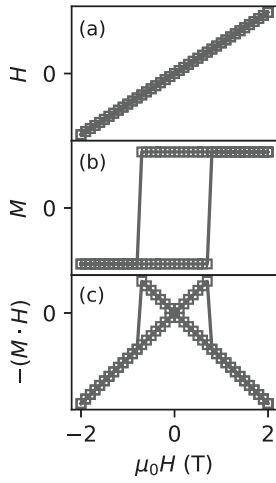


Figure 28: Schematic behaviour of (a)  $H$ , (b)  $M$  and (c)  $M \cdot H$  for a magnetic field sweep parallel to the magnetic easy axis.

<sup>124</sup> A. P. Mihai et al., Phys. Rev. B **77**, 060401 (2008)

<sup>125</sup> V. D. Nguyen et al., Phys. Rev. Lett. **107**, 136605 (2011)

<sup>126</sup> V. D. Nguyen et al., Appl. Phys. Lett. **99**, 262504 (2011)

susceptibility leads to an anisotropic field induces magnetization and consequently an anisotropic MMR.

The magnitude of MMR is expected to decrease towards lower temperatures as more and more magnon modes are frozen out. This is accounted for by introducing the magnon mass renormalization:<sup>123</sup>

$$D = D_0 + D_1 T^2 + D_2 T^{5/2} \quad (24)$$

where the  $T^2$ -term is the temperature dependence of the Fermi distribution and the  $T^{5/2}$ -term is due to magnon-magnon interactions. In the previous chapter a constant negative MR was observed in the magnetic field sweeps along the  $z$ -direction, showing only a weak temperature dependence until it is overcome by the strong positive MR introduced by the Lorentz deflection. The temperature dependence is predominantly contained in the first term of Eq. 17. Consequently, a weak temperature dependence indicates that the second term in Eq. 17 is governing the MMR.

At intermediate temperatures, before the MMR is obscured by the Lorentz MR, an additional experimental fingerprint of the MMR can be observed in magnetic field sweeps along the easy axis. In the low field region a pronounced "bow tie" structure can be observed (cp. Figure 28). This pattern can be understood as the following. Starting with  $\vec{M}$  along  $-z$  ( $H = 0$ ) and applying  $\vec{H}$  along  $-z$  increases the magnon gap (cp. Eq. 17) and consequently decreases the resistivity ( $M \downarrow\downarrow H$ ). The system will return to its initial state upon reducing the external magnetic field. A magnetic field applied along  $z$  is now antiparallel to  $\vec{M}$ , effectively decreasing the magnon gap and increasing the resistivity above the zero field level ( $M \uparrow\uparrow H$ ). The linear behavior continues until the external magnetic field exceeds the coercive field and the magnetization switches to  $z$ . At the point of the magnetization reversal also the resistivity switches to a lower level. The lower level is exactly the resistivity expected when starting with  $\vec{M}$  along  $z$  and increasing the magnetic field  $\vec{H}$  along  $z$  ( $M \uparrow\uparrow H$ ).

Figure 29 depicts  $\rho_{xx}$  at 100 K recorded during a magnetic field sweep along the  $z$ -direction in a device, where the  $c$ -axis is parallel to  $z$ . The resistivity decreases linearly as expected from the MMR for  $\vec{M} \parallel \vec{H}$ . The "bow tie" structure is more pronounced at low temperatures as the coercive field increases and thus a larger  $\vec{H}$  antiparallel to  $\vec{M}$  can be achieved. The coercive field in the microstructures is further increased by the shape anisotropy. This "bow tie" structure was previously observed in FePt thin films, FePt nanowires and NiFe nanowires and discussed in terms of MMR.<sup>124,125,126</sup>



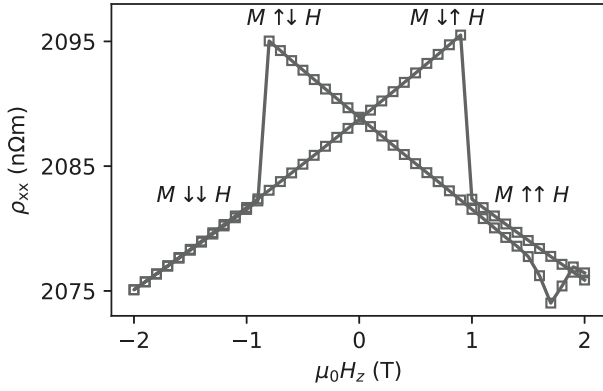


Figure 29: Longitudinal resistivity  $\rho_{xx}$  at 100 K for external magnetic fields applied along the z-direction. The bow-tie structure arises from the increased coercivity at 100 K such that the external field can be applied antiparallel to the magnetization. This leads to a further increase of the resistivity above the  $\mu_0 H_z = 0$  level until the magnetization switches and thus  $H$  is again parallel to  $M$ .

Overall  $\text{Co}_3\text{Sn}_2\text{S}_2$  exhibits a large AMR around the ordering temperature, where the relevant direction is the  $c$ -axis. The easy direction of  $\text{Co}_3\text{Sn}_2\text{S}_2$  is aligned along this crystal direction. Therefore, the AMR is connected to the magneto-crystalline anisotropy. Assuming that the projection of  $\vec{H}$  on  $\vec{M}$  is the relevant quantity for the MMR, it allows to explain the AMR in the ferro- and paramagnetic phase of  $\text{Co}_3\text{Sn}_2\text{S}_2$  down to 100 K.

## AMR at low temperatures

Towards low temperatures the AMR caused by the MMR vanishes. However, the MR in external magnetic fields is still highly anisotropic, as it can be seen in Figure 30. Here, the same set of magnetic field rotations are depicted for a sample temperature of 20 K. The coercive field of the  $\text{Co}_3\text{Sn}_2\text{S}_2$  microstructure is approximately 1.9 T at 20 K, so that an external magnetic field of 1 T is insufficient to switch the magnetization. This can be deduced from the absence of any anomalous Hall signal (i.e. the sharp switching at  $90^\circ$  and  $270^\circ$ ) in the transverse resistivity  $\rho_{yx}$ , recorded during the out-of-plane rotations (cp. Figure 30h,i).

The evolution of  $\rho_{xx}$  during rotations of  $\vec{H}$  is rather complicated and can not be reduced to one particular effect with one relevant direction. However, the raw data suggest two contributions. For the in-plane rotation,  $\rho_{xx}$  appears to be dominated by a sinusoidal modulation with a barely visible modulation on top. The sinusoidal modulation seems to be almost absent in the oopt

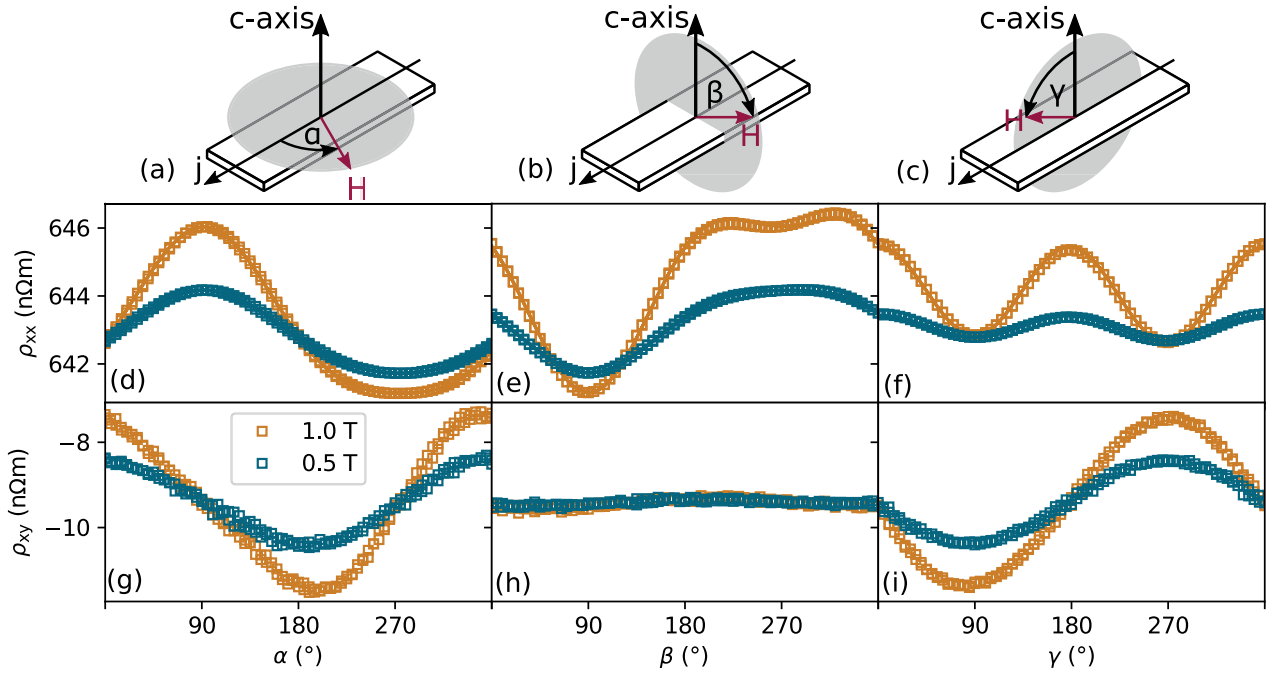


Figure 30: (a)-(c) Schematic representation of the three orthogonal rotation planes around three distinguished directions, namely the surface normal  $n \parallel z$ , the current direction  $j \parallel x$  and transverse direction  $t \parallel y$ . (d)-(f) Longitudinal resistivity  $\rho_{xx}$  recorded for rotations of an external magnetic field of  $\mu_H = 0.5$  T and 1 T at 20 K. (g)-(i) Corresponding transverse resistivity  $\rho_{xy}$ .

rotation, where a  $\sin^2$ -shaped modulation is dominant. For both contributions, the amplitude increases for increasing the external magnetic field from 0.5 T to 1 T. To test whether a combination of a sin and a  $\sin^2$  modulation can represent the data, the following function is used to fit the measurements:

$$\rho_{xx} = A_1 \sin(\phi) + A_2 \sin^2(\phi) \quad (25)$$

here  $A_1$  is the amplitude of the sin modulation,  $A_2$  is the amplitude of the  $\sin^2$  modulation and  $\phi$  is  $\alpha$ ,  $\beta$  or  $\gamma$  for the ip, oopj or oopt rotation, respectively. The fits are depicted by the solid lines in Figure 30d-f. In the following both contributions and their possible origins are discussed.

Figure 31 depicts  $\rho_{xx}^{\text{sym}} = \rho_{xx} - A_1 \sin(\phi)$  for the three field rotations. This equals the  $\sin^2$  modulation and it is named the symmetric contribution as the effect is symmetric with respect to the magnetic field:

$$\begin{aligned} \rho_{xx}^{\text{sym}}(H) &= \rho_{xx}^{\text{sym}}(-H) \\ \rho_{xx}^{\text{sym}}(\phi) &= \rho_{xx}^{\text{sym}}(\phi + 180^\circ) \end{aligned} \quad (26)$$

In the ip rotation,  $\rho_{xx}^{\text{sym}}$  is minimal for  $\vec{H} \parallel x$  and maximal for  $\vec{H} \parallel y$ . The resistivity is increasing with increasing magnetic

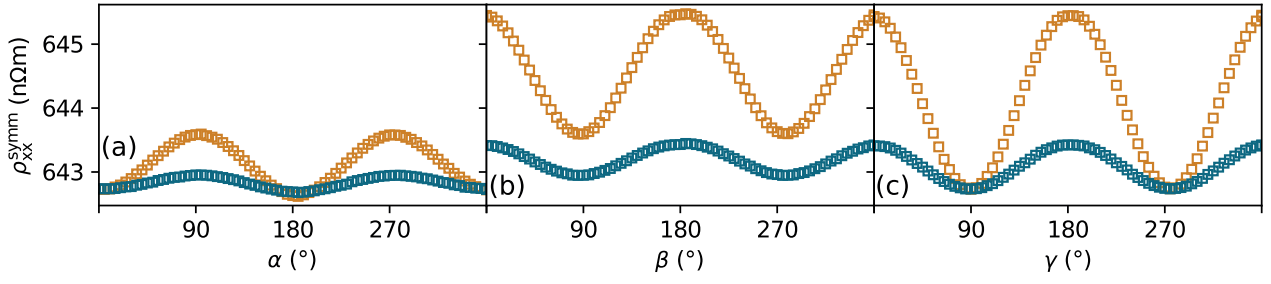


Figure 31: Symmetric contribution  $\rho_{xx}^{\text{sym}}$  in the ip (a), oopj (b) and oopt rotation (c) at 20 K for  $\mu_0 H = 0.5$  T and 1 T

field for  $\vec{H} \parallel y$ . A possible origin for this is the MR caused by the Lorentz deflection of charged carriers in a magnetic field. This type of MR is here referred to as orbital MR. The charge current in the presence of both an electric and magnetic field can be expressed as:<sup>127,128</sup>

$$\vec{j} = \sigma \cdot \vec{E} = ne\mu\vec{E} + \mu\vec{j} \times \vec{B} \quad (27)$$

where  $n$  is the charge carrier concentration,  $e$  is the elementary charge and  $\mu$  is the mobility tensor. In the experiment the charge current is applied along the  $x$ -direction. Therefore, only  $\vec{B} \perp x$  leads to orbital MR as it is the case for  $\alpha = 90^\circ$  and  $270^\circ$  and almost no field dependence of  $\rho_{xx}^{\text{sym}}$  is observed for  $\vec{H} \parallel x$ . The small negative MR for  $\vec{H} \parallel x$  will be discussed later for in-plane rotations measured at 5 K.

Turning now to the discussion of  $\rho_{xx}^{\text{sym}}$  in the oopj rotation. Here no modulation is expected from the orbital MR as  $\vec{B} \perp x$  for all angles of  $\beta$ . The anticipated result for only considering an isotropic orbital MR is horizontal lines shifted to higher resistivity for larger magnetic fields. Indeed, the average resistivity increases with increasing magnetic field. However a pronounced modulation is observed which has a maximum for  $\vec{H} \parallel z$ . This can be understood by having a closer look at the anisotropy of the mobility tensor  $\mu$  (cp. Eq. 27).  $\mu$  is often approximated as isotropic and therefore, written as scalar. However, the anisotropy of the mobility can lead to an anisotropic orbital MR. This has been observed for many high mobility semimetals such as Bi and WTe<sub>2</sub>.<sup>129–133</sup> The charge carrier deflection has a defined direction as it is the result of a cross product of the current with the magnetic field. For example a magnetic field parallel to  $z$  will deflect charge carriers moving along the  $x$ -direction parallel to the  $y$ -direction. The fact that the orbital MR is maximum for  $\vec{H} \parallel z$  indicates that the in-plane mobility is larger compared to the out of plane mobility. The MR for  $\vec{H} \parallel z$  in the ip rotations has the

<sup>127</sup> B. Abeles and S. Meiboom, Phys. Rev. **101**, 544–550 (1956)

<sup>128</sup> J. E. Aubrey, J. Phys. F **1**, 493–497 (1971)

<sup>129</sup> A. Collaudin et al., Phys. Rev. X **5**, 021022 (2015)

<sup>130</sup> M. N. Ali et al., Nature **514**, 205–208 (2014)

<sup>131</sup> Y. Zhao et al., Phys. Rev. B **92**, 041104 (2015)

<sup>132</sup> S. Zhang et al., Phys. Rev. B **99**, 035142 (2019)

<sup>133</sup> J. Yang et al., Phys. Rev. Materials **3**, 014201 (2019)

same magnitude as the MR for the same field orientation in the oopj direction. This is expected when considering the orbital MR as a common origin.

In the oopt rotations a large modulation of  $\rho_{xx}^{\text{sym}}$  can be observed similar to the oopj rotations. However, no change of  $\rho_{xx}^{\text{sym}}$  with the magnitude of  $H$  is observed for  $\vec{H} \parallel x$ . This can be understood as the Lorentz force vanishes for  $\vec{B} \parallel \vec{j}$  (cp. Eq. 27). Again, the orbital MR can be discussed as the origin of the AMR in this rotation plane. The positive MR at  $\gamma = 0^\circ, 180^\circ$  and  $360^\circ$  is increasing with magnetic field as the Lorentz force increases. Furthermore, the resistivity level for  $\vec{H} \parallel x$  matches the same configuration from the ip rotation and also the resistivity levels for  $\vec{H} \parallel z$  matches the oopj maxima. In conclusion the observed AMR in the symmetric contribution to the longitudinal resistivity at 20 K can be explained in terms of the orbital MR with the particular situation of anisotropic carrier mobilities.

The antisymmetric contribution can be written in a similar way compared to Eq. 26:

$$\begin{aligned}\rho_{xx}^{\text{asym}}(H) &= -\rho_{xx}^{\text{asym}}(-H) \\ \rho_{xx}^{\text{asym}}(\phi) &= -\rho_{xx}^{\text{asym}}(\phi + 180^\circ)\end{aligned}\quad (28)$$

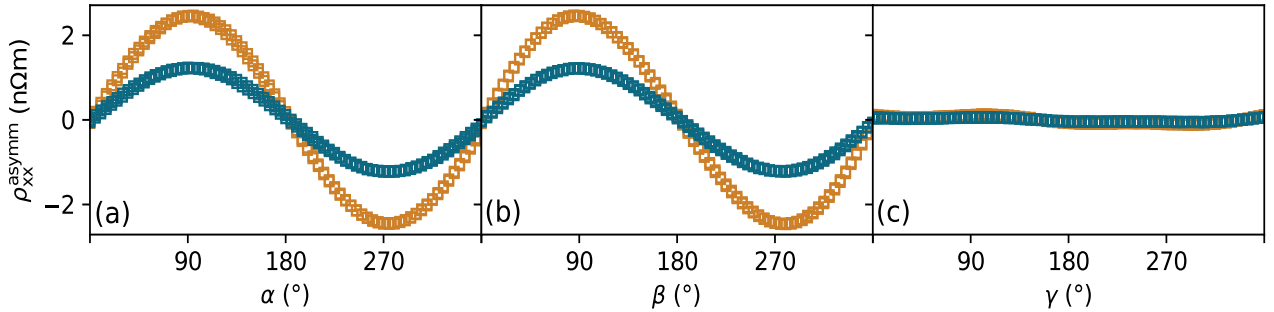


Figure 32: Antisymmetric contribution  $\rho_{xx}^{\text{asym}}$  in the ip (a), oopj (b) and oopt rotation (c) at 20 K for  $\mu_0 H = 0.5$  T and 1 T

$\rho_{xx}^{\text{asym}}$  is almost zero for the oopt rotation and it is comparable in the ip and oopj rotation. The resistivity increases when  $\vec{H}$  is rotated towards  $y$  and decreases when  $\vec{H}$  is rotated towards  $-y$  in both, the ip and oopj rotation. Furthermore, the amplitude is increasing with the external magnetic field and the effect switches sign when the magnetization switches from  $z$  to  $-z$  or vice versa.<sup>134</sup> The  $y$ -direction is the relevant axis for the effect. However, it is unclear at this point what mechanism is responsible for the antisymmetric contribution. Experiments with magnetic

<sup>134</sup> The switching is confirmed by a large change in the transverse resistivity caused by the anomalous Hall effect (which is not shown here for clarity).

fields sufficiently large ( $\approx 25$  T to fully rotate the magnetization are needed to investigate the origin of this contribution.

It was reported that  $\text{Co}_3\text{Sn}_2\text{S}_2$  exhibits a negative quadratic MR for  $\vec{H} \parallel j$  at 2 K, originating from the chiral anomaly.<sup>135</sup> The negative MR is very sensitive to the angle between  $\vec{H}$  and  $j$  because it can be easily covered by a large orbital MR. Measurements of the longitudinal resistivity for in-plane rotations of an external magnetic field of up to 5 T are carried out at 5 K to investigate the negative MR for  $\vec{H} \parallel j$  in more detail. The measurements are performed in a cryostat with a superconducting split coil magnet and a single axis rotation stage. Figure 33 depicts  $\rho_{xx}$  (open symbols) for rotations of  $\mu_0 H = 1$  T, 3 T and 5 T.

<sup>135</sup> E. Liu et al., Nat. Phys. **14**, 1125–1131 (2018)

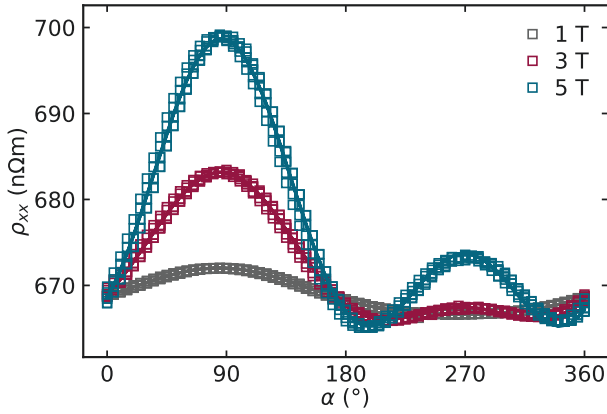


Figure 33: Longitudinal resistivity  $\rho_{xx}$  recorded for rotations of an external magnetic field of  $\mu_H = 0.5$  T and 1 T in-plane at 20 K. The open symbols are the raw data and the solid lines represent fits to Eq. 25.

Again multiple contributions are present and Eq. 25 is used to fit the data (solid lines in Figure 33).<sup>136</sup> The symmetric and antisymmetric contributions of  $\rho_{xx}$  are depicted in Figure 34. The

$$\rho_{xx} = A_1 \sin(\phi) + A_2 \sin^2(\phi)$$

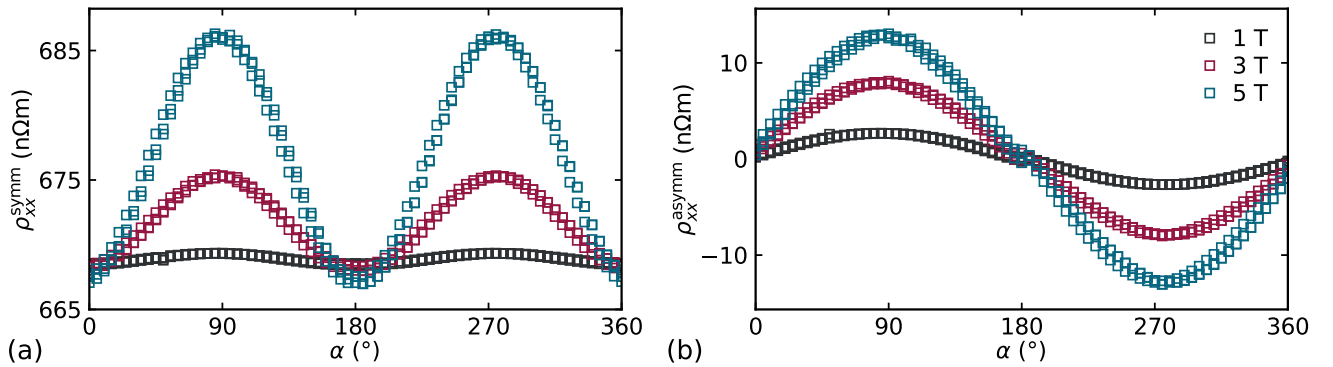


Figure 34: The two contributions to  $\rho_{xx}$  at 5 K from Figure 33 corresponding to (a) the  $\sin^2$ -term and (b) the  $\sin$ -term of Eq. 25.

qualitative behavior for both contributions is comparable to the

results at 20 K (cp. Figure 31a and Figure 32a). The magnitude of the symmetric contribution ( $\propto \sin^2$ ) increases as  $H^2$ , whereas the magnitude of the antisymmetric contribution scales linearly with  $H$ . The scaling with  $H^2$  is expected for the MR arising from Lorentz deflection in compensated metals.<sup>137</sup> If the symmetric contribution stems only from the ordinary MR one would expect to find a field independent resistivity  $\rho_0$  for  $\vec{H} \parallel j$ . However, a negative MR is observed for  $\vec{H} \parallel j$ . This can be explained by two different effects: the chiral anomaly and current jetting. Current jetting can occur in high mobility materials, where the current is not injected homogeneously into the sample. The resistivity along the magnetic field direction is smaller compared to the perpendicular direction. Consequently, the current flows predominantly parallel to the magnetic field direction. In turn, this can lead to a decoupling between the current and voltage probes in a four-point measurement geometry.<sup>138</sup>

Liang and coworkers investigated the signatures of the chiral anomaly in a trivial semimetal (Bi) and compared it to two topological semimetals (Na<sub>3</sub>Bi, GdPtBi).<sup>139</sup> The authors demonstrate that the competition between the current jetting and the chiral anomaly is strongly dependent on the mobility of the material. Materials with high mobility show a strong orbital MR and, thus, a strong anisotropy of the resistivity. This for example is the case for TaAs and NbP with mobilities of 300 000 cm<sup>2</sup>/Vs to 500 000 cm<sup>2</sup>/Vs.<sup>140,141</sup> In such materials, the in-plane AMR is characterized by a small negative MR for  $\vec{H} \parallel j$  and a steep increase of the resistivity when rotating the field away from the current direction, leading to a small ratio of negative MR to orbital MR. In GdPtBi the ratio of orbital to chiral anomaly induced MR is approximately 1:1, which results from the low mobility of 1500 cm<sup>2</sup>/Vs.<sup>142</sup> The defined sample geometry and contact placement of the Co<sub>3</sub>Sn<sub>2</sub>S<sub>2</sub> micro ribbon device improves the homogeneity of the current injection and, thus, renders the device less prone to current jetting. However, the mobility of Co<sub>3</sub>Sn<sub>2</sub>S<sub>2</sub>, with 73 000 cm<sup>2</sup>/Vs, is much larger compared to GdPtBi.<sup>143</sup> Consequently, the origin of the negative MR can not be determined unambiguously. The contribution stemming from current jetting can be further quantified by measuring at the sample spine and the sample edge. This constitutes a possible test for future investigations. Overall, the AMR measurements at low temperatures demonstrate the difficulties arising when probing the chiral anomaly in transport experiments. However, they give additional information about the anisotropy of the resistivity and ,there-

<sup>137</sup> I. M. Lifshitz et al., Zh. Eksperim. i Teor. Fiz. **31** (1956), English translation: Soviet Phys.- JETP **12**, 283 (1961)

<sup>138</sup> R. D. dos Reis et al., New J. Phys. **18**, 085006 (2016)

<sup>139</sup> S. Liang et al., Phys. Rev. X **8**, 031002 (2018)

<sup>140</sup> C. Shekhar et al., Nat. Phys. **11**, 645–649 (2015)

<sup>141</sup> C.-L. Zhang et al., Phys. Rev. B **95**, 085202 (2017)

<sup>142</sup> M. Hirschberger et al., Nat. Mater. **15**, 1161–1165 (2016)

<sup>143</sup> E. Liu et al., Nat. Phys. **14**, 1125–1131 (2018)

fore, help to assess the negative MR regarding current jetting and chiral anomaly.

Lastly, there is the point, that no clear evidence for AMR only sensitive to the direction of the magnetization has been observed in  $\text{Co}_3\text{Sn}_2\text{S}_2$ . The antisymmetric contribution at low temperatures switches sign for reversing the magnetization. This presumably indicates the presence of an AMR only sensitive to  $\vec{M}$ . However, the magnetic fields accessible in the setup with the vector magnet of 2 T is too small to create a sizable displacement of  $\vec{M}$  from the easy axis. Future experiments in high magnetic fields ( $\approx 25$  T) could be used to investigate the magnetization dependent AMR in  $\text{Co}_3\text{Sn}_2\text{S}_2$ .





# Thermomagnetic Transport

The following chapter is based on my own publication "Signatures of the Magnetic Entropy in the Thermopower Signals in Nanoribbons of the Magnetic Weyl Semimetal  $\text{Co}_3\text{Sn}_2\text{S}_2$ ".<sup>144</sup> Thus, passages and figures from the following chapter are adopted or directly taken from this publication.

The analysis in the previous chapters focuses on transport experiments under isothermal conditions ( $\nabla T = 0$ ). In addition, the presence of a thermal gradient leads to a diffusive motion of charge carriers. Electrons for example will move from the hot to the cold side. Thus, the current density  $\vec{j}$  in linear transport theory is related to both, an electric field  $\vec{E}$  and a temperature gradient  $\nabla \vec{T}$ :<sup>145</sup>

$$\vec{j} = \sigma \vec{E} + \alpha (-\nabla \vec{T}) \quad (29)$$

where  $\sigma$  is the conductivity tensor and  $\alpha$  is the thermopower tensor. This reduces to the previously discussed form of  $\vec{j} = \sigma \vec{E}$  under isothermal conditions ( $\nabla T = 0$ ).

The thermomagnetic measurements in this chapter are performed under open circuit conditions by connecting the contact leads to an input resistance of more than  $10 \text{ G}\Omega$ . Thus, the net current density equals zero ( $\vec{j} = 0$ ). Equation 29 can then be rewritten as:

$$\vec{E} = \sigma^{-1} \alpha (\nabla \vec{T}) = \mathbf{S} \nabla \vec{T} \quad (30)$$

where  $\mathbf{S}$  is the Seebeck tensor.

A vital part of thermomagnetic transport experiments is the evaluation of the thermal gradient. Therefore, the first section is dedicated to the description of the gradient evaluation procedure. The section afterwards focuses on the temperature and magnetic field dependence of the longitudinal components of the Seebeck tensor. In the third section, the transverse Seebeck, namely the Nernst effect, is discussed in detail. A test of the Mott relation is discussed in the last section, to link the magnetotransport experiments of chapter 4 with the thermomagnetic experiments.

<sup>144</sup> K. Geishendorf et al., Nano Lett. **20**, 300–305 (2020)

<sup>145</sup> J. M. Luttinger, Phys. Rev. **135**, A1505–A1514 (1964)

## Gradient Evaluation

The generation of a thermal gradient in the micro ribbon device is achieved by driving a DC current through the heater line. The Joule heating through the ohmic losses heats up one side of the device generating a temperature gradient across the sample. It is possible to apply different temperature gradients, by controlling the DC current. To minimize the thermal gradient along the  $y$ -direction, it is important to fabricate a long heater line compared to the device length. If  $d_H$  denotes the distance of the two heater lines, the heater length is chosen as  $3 \cdot d_H$ . The platinum four-point thermometers are used to evaluate the temperature for different heater currents. The thermometer resistance is calibrated with respect to the cryostat base temperature under isothermal conditions. The temperature dependence of the resistance of the two thermometers is depicted in Figure 35a. Platinum exhibits a large temperature coefficient of the resistance over a broad temperature range. This is beneficial for the use as thermometers. In principle also other metals with a comparable temperature coefficient can be used for the on-chip thermometry. After calibrating the thermometers it is possible to determine the temperature difference  $\Delta T$  between the thermometers. Figure 35b depicts  $\Delta T$  as a function of the average sample temperature ( $T = (T_1 + T_2)/2$ ) for heater currents of 2 mA, 4 mA and 6 mA. Very often, the thermal gradient is approximated to be linear over

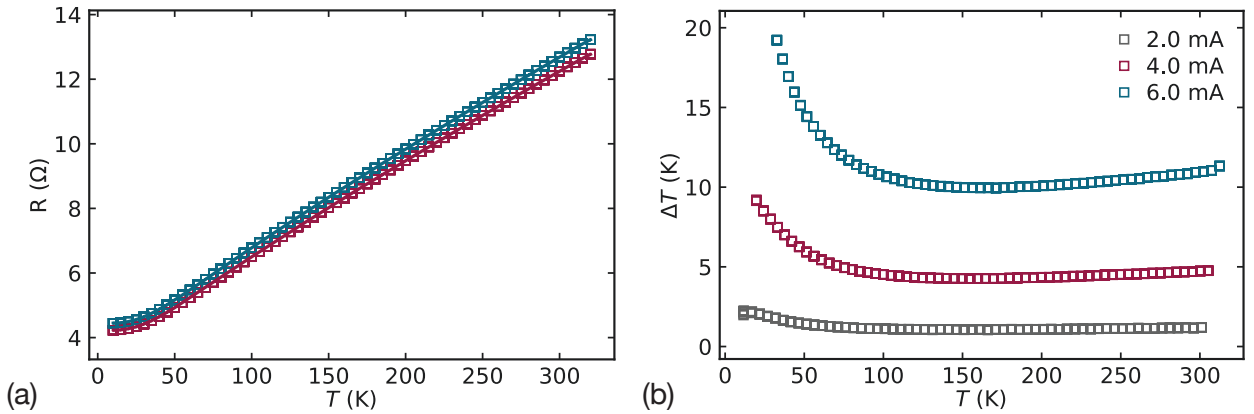


Figure 35: (a) Resistance of the two four-point thermometers on each side of the device. The solid line is the interpolation to generate a function  $T(R)$  returning the temperature for a given resistance. (b) Temperature difference between both thermometers for a heater current of 2 mA, 4 mA and 6 mA as a function of the base temperature.

the sample. However, it is possible to evaluate the gradient more carefully, when the transverse response is recorded at multiple

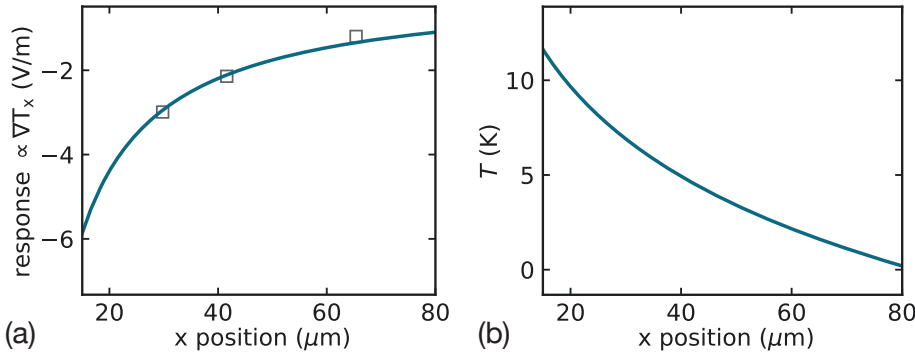


Figure 36: (a) Transverse transport response recorded at three different contact pairs for a heater current of 6 mA at a base temperature of 50 K. The solid line represents a fit to  $f(x) = -a/x$ . The relative temperature profile reconstructed from the fit in (b) and using the boundary conditions given by the two thermometers.

positions of the gradient. The transverse response is proportional to the thermal gradient at the position of the side-contact. Figure 36a depicts the transverse response recorded at three  $x$ -positions (open squares). The response is not constant over the sample length indicating that the gradient is not constant along the  $x$ -direction. The model used for the gradient evaluation originates from the temperature profile in a cylinder with a heat source in the center. This approximation seems appropriate as the device dimensions are much smaller compared to the substrate dimensions. In the cylinder the temperature changes as  $T \propto \ln(x)$  from the center to the cylinder edge. Therefore the temperature is assumed to decay also as  $T \propto \ln(x)$  from the heater line across the sample. Consequently, the thermal gradient is assumed to change as  $\nabla T \propto (1/x)$ . The solid line in Figure 36a represents a fit of  $f(x) = -a/x$  to the transverse response. In the next step the temperature profile is reconstructed by forming the indefinite integral of the temperature gradient and using the thermometer temperatures as boundary conditions:

$$\int \nabla T dx = \int \frac{-a}{x} dx = -a \cdot \ln(x) + b \quad (31)$$

where  $b$  is the integration constant. For the model, only relative temperatures are important. Therefore, it is assumed that the temperature at thermometer 1 ( $x_{\text{therm.1}}$ ) equals  $\Delta T$ , whereas the temperature at thermometer 2 ( $x_{\text{therm.2}}$ ) equals zero. The latter can be used to determine  $b = a \cdot \ln(x_{\text{therm.2}})$ . Please note, if Eq. 31 is evaluated at  $x_{\text{therm.1}}$  one does not obtain  $\Delta T$ . The reason for that is that fitting the transport response which is proportional to the temperature gradient is not equal to fitting the temperature gradient itself. Therefore, the whole temperature profile must be

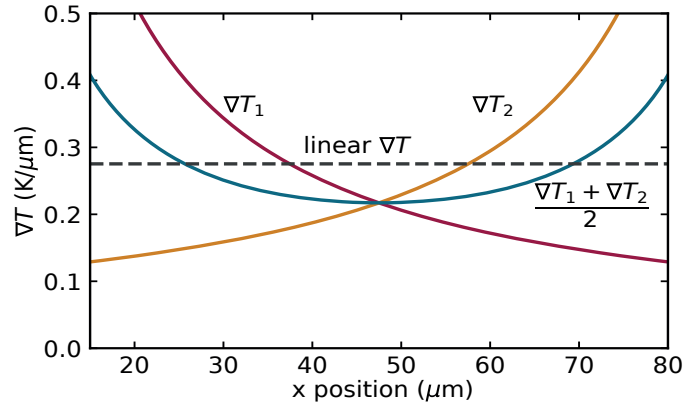


Figure 37: Comparison of the reconstructed gradient (red and yellow line) with a linear gradient (dashed lined) and the effective gradient when applying a gradient reversal technique (blue line).

rescaled, such that the  $T(x_{\text{therm.1}}) = \Delta T$ . The resulting temperature profile is depicted in Figure 36b.

The rescaling also allows to reconstruct the actual gradient. Figure 37 depicts the reconstructed gradient in comparison to a linear gradient. Figure 37 indicates that the actual gradient differs from the linear approximated one and a correction factor is needed depending on the specific contact used for the measurements. The gradient evaluation is performed for five different temperatures (not shown here) and the correction factors for each contact are temperature independent. This is expected, since the gradient shape depends on the device geometry and not the base temperature (as long as the thermal conductivity of the substrate remains isotropic over the temperature range).

The symmetric device layout offers the possibility to reverse the temperature gradient by driving the heater current through the heater on the opposite side of the micro-ribbon. This is especially useful to separate artifacts such as thermovoltages from the cryostat leads, which are even with respect to the on-chip temperature gradient, from the Seebeck signals as they are odd with respect to the temperature gradient. The effective gradient in the current reversal technique is also depicted in Figure 37 by the blue solid line. Alternating the gradient homogenizes the gradient across the ribbon. However, the linear gradient approximation still overestimates the actual gradient between 25  $\mu\text{m}$  and 70  $\mu\text{m}$  and needs to be corrected.

## Seebeck and Magnetoseebeck

When discussing thermoelectric effects, people often call the longitudinal Seebeck component, e.g.  $S_{xx}$ , the Seebeck effect and the transverse Seebeck component, e.g.  $S_{yx}$ , the Nernst effect. The experimental setup to measure the longitudinal Seebeck is depicted schematically in Figure 38. The temperature gradient is generated along the  $x$ -direction, the thermovoltage is measured also along the  $x$ -direction using a Keithley 2182A nanovoltmeter. For the magnetoseebeck measurements an external magnetic field is applied along the  $z$ -direction. Figure 39 depicts the thermovoltage  $V_x$  as a function of the magnitude of the applied thermal gradient. Following Eq. 30, one expects the electric field generated by the temperature gradient to increase linearly with an increasing temperature gradient. This is confirmed by the linear scaling in Figure 39.

Figure 40 depicts  $S_{xx}$  as a function of the temperature. Note that the temperature on the x-axis denotes the average sample temperature. The negative sign of the longitudinal Seebeck coefficient indicates n-type carriers to be dominant in  $\text{Co}_3\text{Sn}_2\text{S}_2$ . This agrees with the carrier densities obtained from a two band fit of the OHE reported by Liu and coworkers for single crystals.<sup>146</sup>

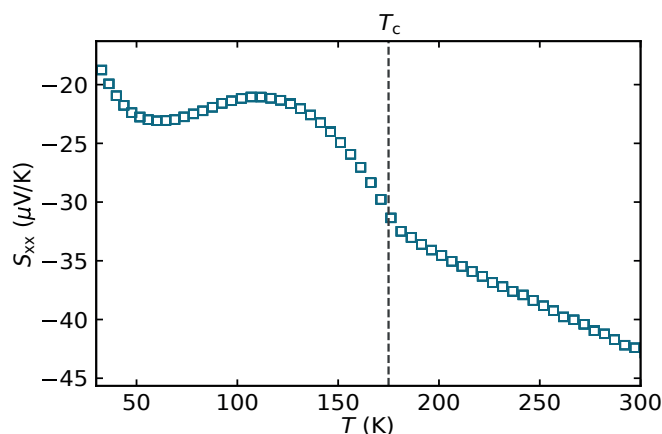


Figure 40: Longitudinal Seebeck coefficient  $S_{xx}$ .  $S_{xx}$  is linearly proportional to the temperature above the magnetic transition temperature and exhibits a suppression below the magnetic ordering temperature.

At 300 K,  $S_{xx}$  is approximately  $-40 \mu\text{V K}^{-1}$  which is smaller than previous literature reports ranging from  $-50 \mu\text{V K}^{-1}$  to  $-60 \mu\text{V K}^{-1}$ .<sup>147,148,149</sup> The magnitude of  $S_{xx}$  decreases with decreasing temperature and exhibits a trend towards zero for  $T < 50$  K. The Seebeck effect is expected to vanish for  $T \rightarrow 0$  K since the entropy, to which the Seebeck effect is linked, also approaches

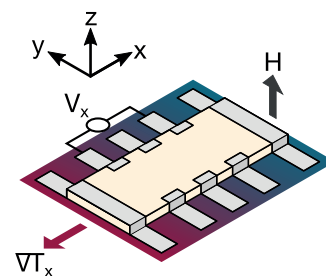


Figure 38: Contacting scheme for measurements of the longitudinal thermomagnetic response.

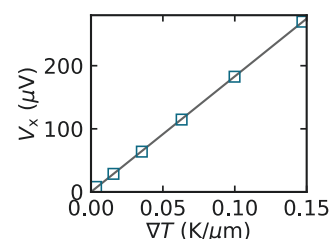


Figure 39: The longitudinal thermo voltage  $V_x$  generated as a function of the longitudinal gradient (open rectangles). The solid line represents a linear fit.

<sup>146</sup> E. Liu et al., Nat. Phys. **14**, 1125–1131 (2018)

<sup>147</sup> J. Corps et al., J. Mater. Chem. A **1**, 6553–6557 (2013)

<sup>148</sup> J. Corps et al., Chem. Mater. **27**, 3946–3956 (2015)

<sup>149</sup> P. Mangelis et al., J. Solid State Chem. **251**, 204–210 (2017)

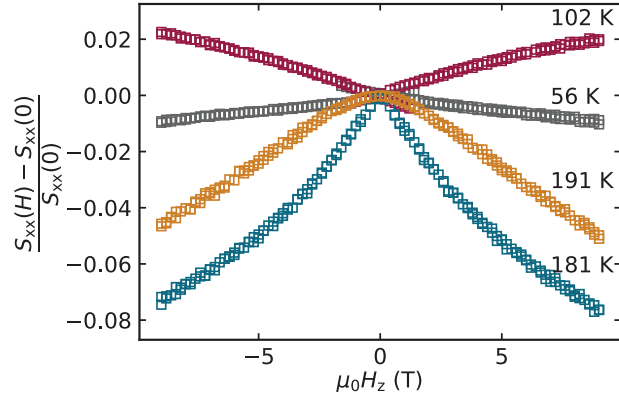


Figure 41: Magnetic field dependence of  $S_{xx}$  for temperature above as well as below the ordering temperature. The raw data indicate multiple sign changes.

zero in this limit. For temperatures above the magnetic ordering temperature,  $S_{xx}$  exhibits a linear slope and is suppressed below the ordering temperature. Again, this can be understood with the reduction of the entropy of the system through the magnetic ordering.

Measurements of the Seebeck effect are a powerful tool to investigate the charge carrier transport and especially the interactions between the charge carriers. Thus, Seebeck measurements are not limited to research of thermoelectric materials but are also used to study strongly correlated electron systems such as superconductors.<sup>150,151,152</sup> The external magnetic field used in measurements of the magneto Seebeck (MS) offers an additional handle to the temperature in standard Seebeck measurements. The MS at one specific temperature is defined as:

$$MS(H) = \frac{S_{xx}(H) - S_{xx}(0)}{S_{xx}(0)} \quad (32)$$

where  $S_{xx}(H)$  is the magnetic field dependent Seebeck and  $S_{xx}(0)$  is the longitudinal Seebeck coefficient without external magnetic field. Exemplary traces of the MS at 56 K, 102 K, 181 K and 191 K are depicted in Figure 41.

The traces in Figure 41 indicate a more complicated temperature dependence compared to the MR discussed in the previous chapter, since the MS changes from negative to positive between 181 K and 102 K and again from positive to negative between 102 K and 56 K. Similar to the approach used in the discussion of the MR, it is useful to extract the temperature dependence of the MS for different magnetic field strength (cp. Figure 42).

No significant influence of the external magnetic field on the longitudinal Seebeck is visible for temperature between 240 K

<sup>150</sup> M. Matusiak et al., Phys. Rev. B **79**, 212502 (2009)

<sup>151</sup> S. Arsenijevic et al., Phys. Rev. Lett. **116**, 087202 (2016)

<sup>152</sup> I. Pallecchi et al., Supercond. Sci. Technol. **29**, 073002 (2016)

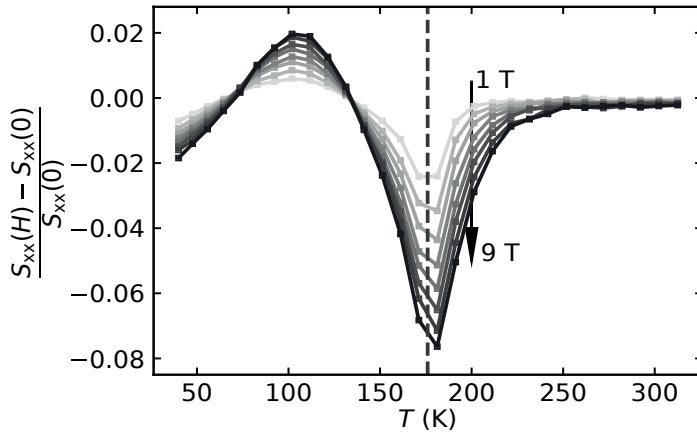


Figure 42: The magnetoseebeck for different field strengths between 1 T and 9 T as a function of temperature. A negative MS of up to 7.5 % is visible at the magnetic transition.

and 300 K. A negative peak in the MS is visible around the ordering temperature. The width and height of the peak is increasing with increasing external magnetic field. A very similar behavior was recently observed in  $\text{Fe}_2\text{V}_{0.9}\text{Cr}_{0.1}\text{Al}_{0.9}\text{Si}_{0.1}$ . There it was concluded that the Seebeck effect is enhanced by spin fluctuations. Thus, the suppression of spin fluctuations by the external magnetic field leads to a negative MS.<sup>153</sup> This mechanism appears to be generic for magnetically ordered systems since the magnetic transition coincides with a negative peak of the MS in many materials.<sup>154–157</sup> Note that this behavior is qualitatively similar to the MR observed around the ordering temperature. However the MS reaches approximately -7.5 %, which is three times larger compared to the MR.

Another interesting feature is the positive MS between 80 K and 130 K. Here, the external magnetic field increases the Seebeck effect by 2 % at 9 T. The diffusive part of the Seebeck effect should not be affected by the external magnetic field. However, there are other contributions which are enhanced or suppressed by the magnetic field. The two most often discussed contributions are the phonon- and magnon-drag.

A thermal gradient also results in a movement of phonons. The phonons can change the electron momentum through phonon-electron interactions and thus contribute to the Seebeck coefficient. This effect is only prominent around a specific temperature  $T \approx T_{\Theta}/5$ , where  $T_{\Theta}$  is the Debey temperature.<sup>158</sup> At higher temperatures the phonons equilibrate through phonon-phonon scattering rather than phonon-electron scattering, while at low temperatures the number of phonons decreases and, thus,

<sup>153</sup> N. Tsujii et al., *Sci. Adv.* **5** (2019)

<sup>154</sup> B. Chen et al., *Phys. Rev. B* **53**, 5094–5097 (1996)

<sup>155</sup> D. V. Maheswar Repaka et al., *J. Appl. Phys.* **112**, 123915 (2012)

<sup>156</sup> G. V. M. Williams and J. E. Stephen, *Adv. Cond. Matter Phys.* **2017**, 7578930 (2017)

<sup>157</sup> A. Kumar et al., *Mater. Res. Express* **5**, 086110 (2018)

<sup>158</sup> F. J. Blatt et al., *Phys. Rev. Lett.* **18**, 395–396 (1967)



<sup>159</sup> A. Aziz et al., Phys. Rev. B **94**, 165131 (2016)

<sup>160</sup> F. Blatt et al., Solid State Commun. **15**, 411–414 (1974)

<sup>161</sup> F. Caglieris et al., Phys. Rev. B **90**, 134421 (2014)

the phonon-drag contribution also decreases. The phonon-drag is only present in clean samples with few impurities and few crystal defects, which is the case in the single crystalline microstructures. The Debye temperature  $T_{\Theta}$  of  $\text{Ni}_3\text{Sn}_2\text{S}_2$  was calculated to be 297 K.<sup>159</sup> Assuming a similar  $T_{\Theta}$  for  $\text{Co}_3\text{Sn}_2\text{S}_2$  would indicate the phonon-drag to be strongest at 60 K. Figure 40 exhibits a slight increase of  $S_{xx}$  around 70 K possibly related to the phonon-drag. Experiments on the magnetoseebeck effect in Cu, Au and Ag wires showed that the phonon-drag contribution can be enhanced by the magnetic field.<sup>160</sup> Therefore, the positive MS between 80 K and 130 K could be explained as a magnetic field enhanced phonon-drag. The different temperature window could be explained if the Debye temperature is higher than approximated above.

The other contribution to the thermopower stems from the charge carriers dragged along with the magnon heat flux. An external magnetic field modifies the magnon population and, thus, influences the magnon-drag. Experiments indicate a decrease of the magnon-drag contribution to the Seebeck with increasing external magnetic field.<sup>161</sup> This effect could explain the sign change of the MS in  $\text{Co}_3\text{Sn}_2\text{S}_2$  observed at temperatures below 80 K. However, a more comprehensive investigation of the MS is needed to disentangle the involved mechanisms. This could for example include MS measurements towards lower temperatures combined with specific heat measurements.

## Anomalous Nernst Effect

The anomalous Nernst effect (ANE) is the thermomagnetic counterpart to the AHE (cp. chapter 4). Both effects are characterized by the same experimental fingerprint i.e an additional contribution, which scales with the magnetization of the sample rather than the external magnetic field. The measurement setup for the ANE is comparable to the setup used for measuring the Seebeck effect. A thermal gradient is applied along the  $x$ -direction and the transverse voltage drop  $V_y$  is recorded (cp. Figure 43). The transverse Seebeck coefficient is evaluated as:

$$S_{yx} = \frac{V_y}{\nabla T \cdot w} \quad (33)$$

where  $V_y$  is the transverse voltage,  $w$  is the sample width and  $\nabla T$  is the temperature gradient. Figure 44 depicts the transverse Seebeck coefficient  $S_{yx}$  recorded for external magnetic field sweeps

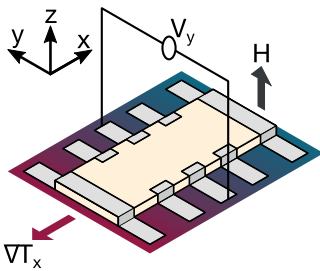


Figure 43: Contacting scheme for measurements of the transverse thermomagnetic response.



along the  $z$ -direction at different temperatures. The traces exhibit a constant slope in the high field region ( $\mu_0 H_z > 5$  T), which stems from the ordinary Nernst effect. Note that the ordinary Nernst signal can originate from both, the  $\text{Co}_3\text{Sn}_2\text{S}_2$  micro ribbon as well as the Pt contacts. A step like change of  $S_{yx}$  is visible around zero field which is related to the anomalous Nernst effect. The magnitude of the anomalous Nernst effect is extracted by a linear fitting of the high field part and extracting the intercept with the ordinate for each temperature. In particular, this allows to evaluate the anomalous contribution also for temperatures in the vicinity of the ordering temperature where the transverse transport signals exhibit more s-shaped traces. The transverse Seebeck co-

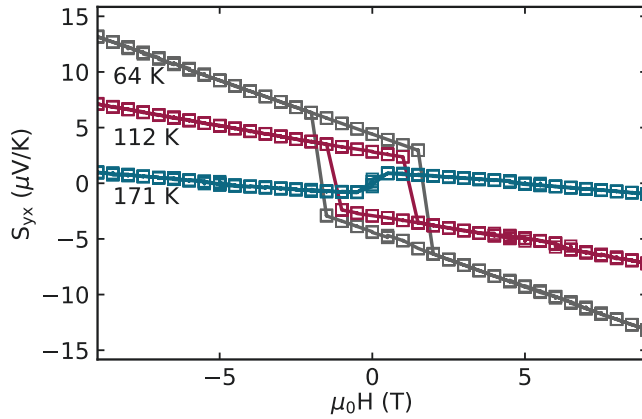


Figure 44: Exemplary transverse Seebeck coefficient ( $S_{yx}$ ) traces recorded for external magnetic field sweeps along the  $z$ -direction. The listed temperatures correspond to the average sample temperature. An anomalous contribution is visible for all three temperatures.

efficient is, like the transverse resistivity, an off diagonal tensor component and is thus odd with respect to the external magnetic field. This antisymmetric behavior is used to correct for possible offsets caused by non-ideal contact placement with the following formula:

$$S_{yx}^A = \frac{S_{yx}^A(B) - S_{yx}^A(-B)}{2} \quad (34)$$

Already the exemplary Nernst sweeps depicted in Figure 44 indicate a sign change between 112 K and 171 K. Figure 45 depicts the extracted anomalous Nernst coefficient as a function of the average sample temperature to study the temperature dependence of the Nernst coefficient in more detail.

The data of three different contact pairs is shown, yielding qualitatively and quantitatively similar results. For each contact pair the individual temperature gradient from the gradient evaluation has been used to calculate the transverse transport response

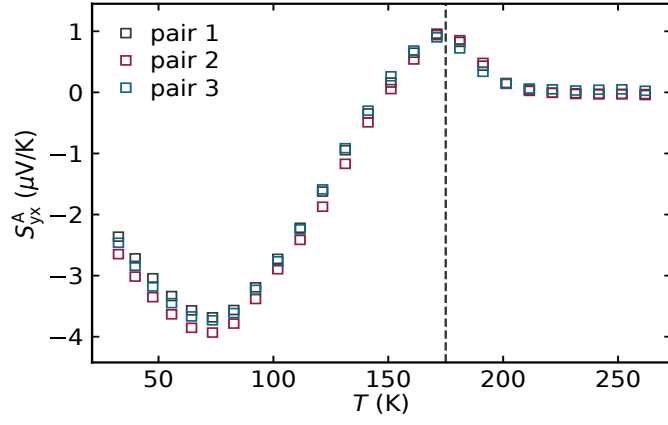


Figure 45: The extracted anomalous Nernst coefficient  $S_{yx}^A$  of three different pairs of sample contacts as a function of the average sample temperature. A sign change at approximately 140 K is visible for all contacts.

from the thermovoltage  $V_y$ . The anomalous Nernst effect is zero in the paramagnetic phase for temperatures above 200 K. However, it becomes finite already 25 K above the ordering temperature of 175 K. This is again, as for the AHE, due to the increasing magnetic susceptibility close to the ordering temperature. After reaching a maximum value of  $1 \mu\text{V K}^{-1}$  at 170 K,  $S_{yx}^A$  starts to decrease with decreasing temperature. The anomalous Nernst coefficient switches sign around 140 K and reaches a negative maximum of  $-3.8 \mu\text{V K}^{-1}$  at 75 K. The magnitude of  $S_{yx}^A$  decreases again below 75 K and tends towards zero. As for the longitudinal Seebeck coefficient also the transverse Seebeck is expected to vanish for  $T \rightarrow 0$ . The maximum magnitude of  $-3.8 \mu\text{V K}^{-1}$  is consistent with two earlier reports of  $-4 \mu\text{V K}^{-1}$  and  $-3 \mu\text{V K}^{-1}$  for the anomalous Nernst effect in  $\text{Co}_3\text{Sn}_2\text{S}_2$ .<sup>162,163</sup> However, both groups did not observe a sign change of the anomalous Nernst coefficient.

Interestingly, only the ANE, and not the AHE, changes sign within the considered temperature range. We compute the anomalous Nernst conductivity  $\alpha_{yx}$  (ANC), to obtain further insight into the thermomagnetic transport properties:

$$\alpha_{yx} = \frac{S_{yx}\rho_{xx} - S_{xx}\rho_{yx}}{\rho_{xx}^2 + \rho_{yx}^2} \quad (35)$$

This equation is derived from Eq. 30. Comparing the terms in Eq. 35 with Eq. 15 one finds an equivalent form:

$$\alpha_{yx} = S_{yx}\sigma_{xx} + S_{xx}\sigma_{yx} \quad (36)$$

Figure 46 depicts the ANC as a function of temperature calculated according to Eq. 35. The ANC is zero in the paramagnetic

<sup>162</sup> L. Ding et al., Phys. Rev. X **9**, 041061 (2019)

<sup>163</sup> S. N. Guin et al., Adv. Mater. **31**, 1806622

regime. However, also the ANC becomes finite slightly above the magnetic ordering temperature as do the AHE and ANE. It increases for temperatures below 200 K and reaches a maximum of  $4 \text{ A m}^{-1} \text{ K}^{-1}$  at 150 K.  $\alpha_{yx}$  decreases below 150 K and the trend

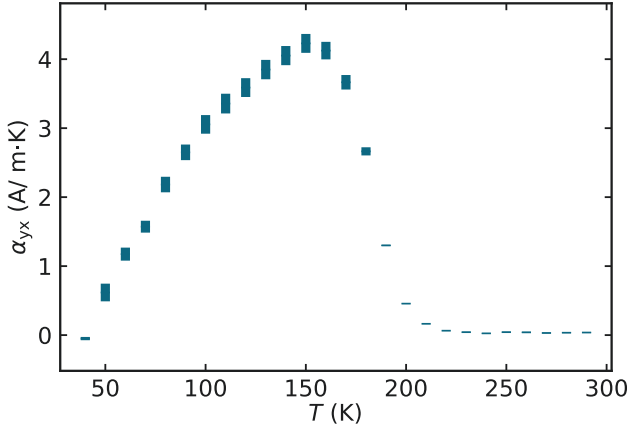


Figure 46: The temperature dependent anomalous Nernst conductivity calculated according to Eq. 35. Note that the bar height of each data point corresponds to the error.

indicates a sign change below 40 K. The qualitative and quantitative behavior is in very good agreement with the experimental results published by Ding and coworkers.<sup>161</sup> The extensive electric and thermomagnetic measurements performed by Ding and coworkers on various  $\text{Co}_3\text{Sn}_2\text{S}_2$  crystals with different purity indicate that the main mechanism for the ANE is also of intrinsic origin.

In conclusion  $\text{Co}_3\text{Sn}_2\text{S}_2$  exhibits a large anomalous Nernst conductivity, which is related to the complicated and interesting band structure of this compound. Furthermore, the sign change in the anomalous Nernst coefficient has not been reported before. To further investigate this feature a test of the Mott relation proposed by Pu and coworkers is carried out for  $\text{Co}_3\text{Sn}_2\text{S}_2$ .<sup>164</sup>

<sup>164</sup> Y. Pu et al., Phys. Rev. Lett. **101**, 117208 (2008)

## Test of the Mott relation

The Mott relations link different transport quantities, in particular the thermopower and the conductivity. However, the validity of the Mott relations is limited to the case of weakly interacting charge carriers.<sup>165</sup> In the special case of metals, where the transport occurs mainly close to the Fermi level, it is possible to further simplify the Mott relation to:

<sup>165</sup> M. Cutler and N. F. Mott, Phys. Rev. **181**, 1336–1340 (1969)

$$\alpha = \frac{\pi^2 k_B^2}{3e} T \left( \frac{\partial \sigma}{\partial E} \right)_\mu \quad (37)$$

where  $k_B$  is the Boltzmann constant,  $e$  the elementary charge,  $T$  the temperature and  $(\partial\sigma/\partial E)_\mu$  is the energy derivative of the conductivity at the chemical potential. This formula can be written for the Seebeck tensor as:

$$\mathbf{S} = \frac{\pi^2 k_B^2}{3e\sigma} T \left( \frac{\partial\sigma}{\partial E} \right)_\mu \quad (38)$$

M. Cutler and N.F. Mott argue that  $(\partial\sigma/\partial E)_\mu$  in Eq. 37 does not change with temperature at low temperatures and thus yields a linear dependence of  $\alpha$  on the temperature. This is often observed and interpreted as validation method of the Mott relation. However, Pu and coworkers derived another test of the Mott relation for the AHE and ANE in the ferromagnetic semiconductor  $\text{Ga}_{1-x}\text{Mn}_x\text{As}$  starting from Eq. 37 evaluated for the transverse component:<sup>166</sup>

$$\alpha_{yx} = \frac{\pi^2 k_B^2}{3e} T \left( \frac{\partial\sigma_{yx}}{\partial E} \right)_\mu \quad (39)$$

They further assume a power law dependence between the longitudinal and transverse transport response. For the resistivity this takes the form of  $\rho_{xy} = \lambda \rho_{xx}^n$  and for the conductivity  $\sigma_{yx} = \lambda \sigma_{xx}^{2-n}$ . With this, one can write the energy derivative in Eq. 39 as:

$$\left( \frac{\partial\sigma_{yx}}{\partial E} \right)_\mu = \left( \frac{\partial\lambda}{\partial E} \right)_\mu \sigma_{xx}^{2-n} + \lambda(2-n) \sigma_{xx}^{1-n} \left( \frac{\partial\sigma_{xx}}{\partial E} \right)_\mu \quad (40)$$

Rewriting Eq. 38 for the longitudinal Seebeck coefficient  $S_{xx}$  yields:

$$\left( \frac{\partial\sigma_{xx}}{\partial E} \right)_\mu = S_{xx} \sigma_{xx} \frac{3e}{\pi^2 k_B^2 T} \quad (41)$$

Now Eq. 41 is inserted in Eq. 40 and subsequently Eq. 40 in Eq. 39. This gives another form of Eq. 39:

$$\alpha_{yx} = \sigma_{xx}^{2-n} \left( \frac{\pi^2 k_B^2}{3e} T \left( \frac{\partial\lambda}{\partial E} \right)_\mu - \lambda(n-2) S_{xx} \right) \quad (42)$$

In the last step  $\lambda \sigma_{xx}^{2-n}$  is replaced by  $\sigma_{yx}$  and  $\sigma_{yx}$  approximated as  $\frac{\rho_{xy}}{\rho_{xx}^2}$ . Thus, yielding the final expression for  $\alpha_{yx}$ :

$$\alpha_{yx} = \frac{\rho_{xy}}{\rho_{xx}^2} \left( \frac{\pi^2 k_B^2}{3e} T \left( \frac{\partial\lambda}{\partial E} \right)_\mu \frac{1}{\lambda} - (n-2) S_{xx} \right) \quad (43)$$

<sup>166</sup> Y. Pu et al., Phys. Rev. Lett. **101**, 117208 (2008)

An expression for  $S_{yx}$  can be derived in a similar manner:

$$S_{yx} = \frac{\rho_{xy}}{\rho_{xx}} \left( \frac{\pi^2 k_B^2}{3e} T \left( \frac{\partial \lambda}{\partial E} \right)_\mu \frac{1}{\lambda} - (n-1) S_{xx} \right) \quad (44)$$

Figure 47 depicts the anomalous Nernst coefficient as a function of temperature for different Mn contents in  $\text{Ga}_{1-x}\text{Mn}_x\text{As}$  (open symbols) reported by Pu and coworkers. The solid lines represent fits of Eq. 44 using  $(\partial \lambda / \partial E)_\mu 1/\lambda$  and  $n$  as fit parameters. The agreement between fit and measurement is interpreted as

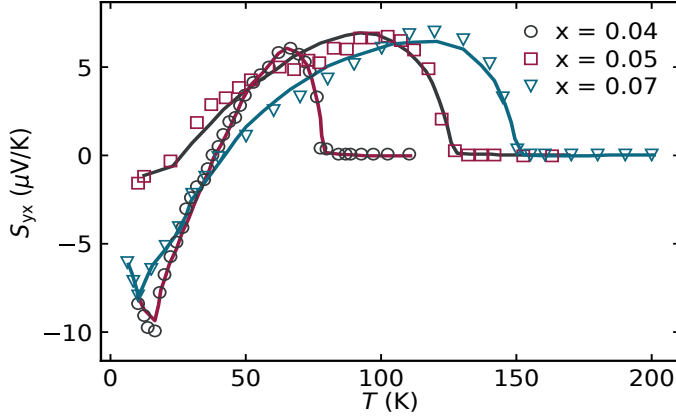


Figure 47: Temperature dependence of the Nernst coefficient of  $\text{Ga}_{1-x}\text{Mn}_x\text{As}$  with different Mn contents. The solid line represents best fits to Eq. 44. The data is taken from Pu et al.<sup>166</sup>

the Mott relation holding for this compound. One can expect to describe  $S_{yx}$  and  $\alpha_{yx}$  with the same set of parameters, as successfully done for different materials.<sup>167,168,169</sup> Furthermore, the fit parameter  $n$  describes the exponent of the power law and, thus, can be used to distinguish between the intrinsic and extrinsic regime, where  $n = 1$  characterizes the extrinsic and  $n = 2$  the intrinsic regime.

We now turn to the temperature dependent Nernst coefficient and ANC in  $\text{Co}_3\text{Sn}_2\text{S}_2$ . The shaded regions in Figure 48a,b represent the corresponding curves calculated from Eqs 44 and 43, respectively, with  $(\partial \lambda / \partial E)_\mu / \lambda = -4.8 \times 10^{19}$  and  $n = 2.3$ . Figure 48c,d displays the difference between the measurements and the calculated curves. Remarkably, both  $\Delta S_{yx}^A$  and  $\Delta \alpha_{yx}$  look very similar and point toward a systematic contribution not considered in Eqs 43 and 44.

The test proposed by Pu and coworkers is only valid up to a certain (bandstructure dependent) temperature. Above this temperature the, neglected higher order terms start to contribute. Considering the small size of the Fermi surface pockets, it is not

<sup>167</sup> R. Ramos et al., Phys. Rev. B **90**, 054422 (2014)

<sup>168</sup> A. Ghosh et al., J. Appl. Phys. **125**, 153902 (2019)

<sup>169</sup> J. Xu et al., Nano Lett. **19**, 8250–8254 (2019)

<sup>170</sup> Q. Shi et al., Results Phys. **11**, 1004–1007 (2018)

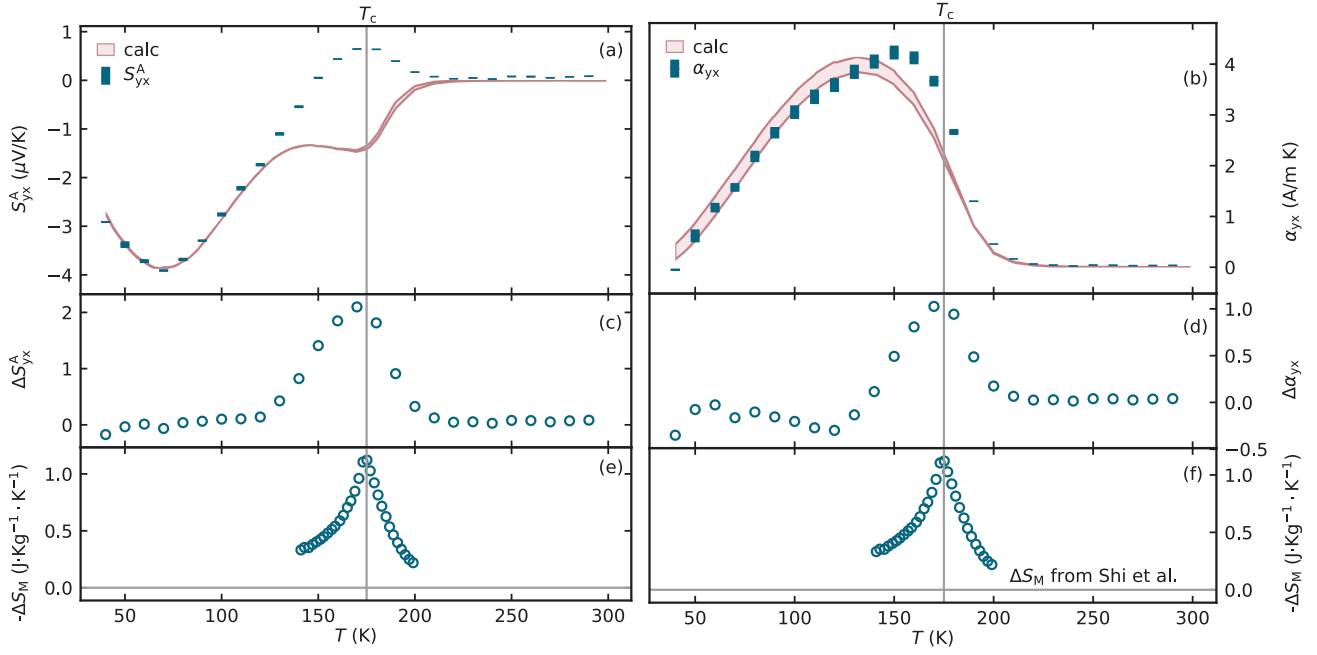


Figure 48: Comparison of the experimental obtained values for  $S_{yx}^A$ (a) and the ANC  $\alpha_{yx}$ (b) with calculations (shaded region) from Eq. 44 and 43, respectively. The differences between Eq. 44 and  $S_{yx}^A$ (c) or Eq. 43 and  $\alpha_{yx}$ (d) is denoted as  $\Delta S_{yx}^A$  and  $\Delta \alpha_{yx}$ , respectively. Isothermal entropy change  $\Delta S^M = S(T, H) - S(T, 0)$  as a function of temperature from magnetocaloric effect measurements for  $\mu_0 H = 5$  T taken from Shi et al. are shown in (e) and (f).<sup>170</sup>Note that the bar height of each data point in (a) and (b) corresponds to the error of the given quantity. The error of the calculations in (a) and (b) is visualized by the shaded region between the two lines.

clear whether this temperature is within the temperature range of the experiment or not. We considered, therefore, higher order terms which can be obtained by expanding in temperature the formula:

$$\alpha_{xy}(T) = \frac{1}{e} \int_{-\text{inf}}^{\text{inf}} d\epsilon \frac{\partial \sigma_{yx}}{\partial \epsilon} s(\epsilon, T) \quad (45)$$

where  $\epsilon$  is the elementary charge and  $s(\epsilon, T)$  is the entropy density associated with carriers of energy  $\epsilon$ .<sup>171,172</sup> However, we could not improve the fit quality with, for example, a cubic term.

It is interesting how large the deviation is around the critical temperature. Figure 48e,f depicts the isothermal entropy change in  $\text{Co}_3\text{Sn}_2\text{S}_2$  caused by an external magnetic field obtained from magnetocaloric measurements.<sup>173</sup> The change in the configuration entropy associated with the magnetic degrees of freedom changes with the external magnetic field at temperatures close to the critical temperature. The similarities between Figure 48c,d and Figure 48e,f suggest that magnetic degrees of freedom influence the entropy-flow responsible for the Nernst effect. Magnetic fluctuations are important for the ANE since they effectively restore time-reversal symmetry at higher temperatures, hence making the ANE vanish. The present analysis indicates that magnetic

<sup>171</sup> D. Xiao et al., Phys. Rev. Lett. **97**, 026603 (2006)

<sup>172</sup> M. P. Ghimire et al., Phys. Rev. Res. **1**, 032044 (2019)

<sup>173</sup> Q. Shi et al., Results Phys. **11**, 1004–1007 (2018)

fluctuations can help to enhance the ANC at the critical temperature.

The question remains whether this is a generic behavior for ferromagnetic materials close to the ordering temperature and if so, why it was not reported previously. One aspect is the sign of the additional contribution. In the presented case of  $\text{Co}_3\text{Sn}_2\text{S}_2$  the sign of the anomalous Nernst coefficient around the magnetic ordering temperature is opposite to the coefficient at lower temperatures. Thus, the deviation between calculation and experiment is obvious in Figure 48a. However, for the ANC the additional contribution has the same sign and thus creates a shoulder rather than a sign change in the experimental data. Upon fitting, the deviation caused by this shoulder appears less dramatic and could almost be assigned to experimental uncertainties.

Figure 49 depicts the ANE coefficient for  $\text{Ga}_{0.93}\text{Mn}_{0.07}\text{As}$  and a calculation according to Eq. 44 for different parameters as in Figure 47, chosen such that the calculation matches the experimental data especially in the low temperature regime. This example indicates that the contribution discussed above is present also in other ferromagnetic materials. However, it can be harder to detect if the contribution creates a shoulder instead of a sign change. Also there are experiments reported where the fit is only shown below the critical temperature and therefore no deviation is observed.<sup>175,176</sup>

The analysis above indicates that the entropy associated with magnetic degrees of freedom close to the critical temperature can be important for the magnitude of the ANE. This provides a clear motivation for a theoretical description of the anomalous Nernst effect in the full temperature range. Such challenging theoretical development would constitute a rich playground linking paradigmatic problems such as transport phenomena originated in the Berry phase and long-range spontaneous symmetry breaking.<sup>177</sup>

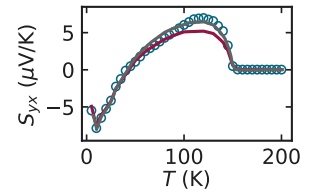


Figure 49: Exemplary  $S_{yx}$  of  $\text{Ga}_{0.93}\text{Mn}_{0.07}\text{As}$  compared to a calculated  $S_{yx}$  (red line) and a best fit (black line).<sup>174</sup>

<sup>174</sup> Y. Pu et al., Phys. Rev. Lett. **101**, 117208 (2008)

<sup>175</sup> R. Ramos et al., Phys. Rev. B **90**, 054422 (2014)

<sup>176</sup> A. Ghosh et al., J. Appl. Phys. **125**, 153902 (2019)

<sup>177</sup> J. Noky et al., Phys. Rev. B **98**, 241106 (2018)





# *Summary and Outlook*

## *Summary*

The results of various magnetotransport experiments in  $\text{Co}_3\text{Sn}_2\text{S}_2$  microstructures are reported in this thesis. As a magnetic Weyl semimetal,  $\text{Co}_3\text{Sn}_2\text{S}_2$  displays intriguing physics, originating from its topological as well as magnetic properties. This leads to many interesting transport responses, including the anomalous Hall effect, the anisotropic magnetoresistance and the anomalous Nernst effect.

An important aspect of this thesis, preceding the actual transport experiments, is the successful fabrication of high quality singly crystalline microstructures. The device platform described within this thesis is based on the combination of FIB preparation and laser lithography. The high quality of materials grown by single crystal growth techniques in conjunction with the precise contact definition with laser lithography result in a powerful platform for general transport experiments.

A particularly large anomalous Hall effect is observed in measurements of the transverse transport response performed in  $\text{Co}_3\text{Sn}_2\text{S}_2$ . The independence of the anomalous Hall conductivity from the longitudinal conductivity suggests an intrinsic origin. Comparing the experimental results with band structure calculations, using the Berry curvature, gives very good agreement. Furthermore, the agreement between measurements of the microstructures with measurements on single crystals demonstrates the high quality of the microstructure devices.

The magnetoresistance of  $\text{Co}_3\text{Sn}_2\text{S}_2$  is found to be highly anisotropic. The magnetoresistance at temperatures above 100 K can be consistently explained invoking the magnon magnetoresistance. This effect is present in the ferromagnetic as well as the paramagnetic phase and exceeds all other MR effects above 100 K. The remarkably strong magneto-crystalline anisotropy of  $\text{Co}_3\text{Sn}_2\text{S}_2$  along its crystalline  $c$ -axis leads to the interesting obser-

vation, that the magnon magnetoresistance appears to depend on the projection of the external magnetic field on the magnetization. Magnon modes are frozen out at low temperature and the magnon magnetoresistance vanishes. However, the anisotropy of the carrier mobilities gives rise to an anisotropic orbital magnetoresistance. Interestingly, no clear signs of crystalline/non-crystalline AMR, depending on the magnetization direction, can be observed.

The transverse transport response in thermomagnetic measurements exhibits a large anomalous Nernst effect. The anomalous Nernst conductivity reaches up to  $4 \text{ A m}^{-1} \text{ K}^{-1}$  in  $\text{Co}_3\text{Sn}_2\text{S}_2$ . This is an important aspect for the uprising discussion of alternative designs of thermoelectric devices based on the transverse transport responses. Interestingly, both quantities, the anomalous Nernst coefficient and the anomalous Nernst conductivity, exhibit a sign change as a function of temperature. However, their counterparts, the anomalous Hall coefficient and the anomalous Hall conductivity, display no sign change. This indicates that the anomalous Hall and Nernst effects indeed probe different states. Therefore, the combined measurements gives an extended toolbox for studying topological materials. The Mott relation is regularly used to connect the different transport coefficients. Testing one specific formulation of the Mott relation led to the identification of an additional contribution at the magnetic phase transition. This contribution appears to be generic for ferromagnetic materials and it is so far not accounted for by this particular formulation of the Mott relation. The change of magnetic entropy at the phase transition is discussed as possible origin for this contribution.

## *Outlook*

The experiments reported in this thesis reveal interesting aspects which are not fully resolved, yet, and can be studied in future experiments. One example is the magnetic structure of  $\text{Co}_3\text{Sn}_2\text{S}_2$ . Even though many details are reported through out various publications, the origin and properties of the anomalous magnetic phase directly below the ordering temperature are yet not understood. The Kerr microscopy investigations reported in this thesis illustrate that the anomalous phase is not connected to the bubble domains formed during field cool experiments.

Two contributions to the highly anisotropic magnetoresistance in  $\text{Co}_3\text{Sn}_2\text{S}_2$  are successfully resolved. However, the complex results of the AMR measurements at low temperatures indicate further contributions. Experiments in large magnetic fields, only attainable in high-field laboratories, could be used to coherently rotate the magnetization in presence of the strong magneto-crystalline anisotropy and, thus, resolve other AMR contributions.

It is the first time that a deviation from the particular formulation of the Mott relation is reported. Looking at other investigations from this perspective indicate that this is a generic effect. Further thermomagnetic transport experiments in proximity to the magnetic ordering temperature of different materials could be used to study the origin of this contribution in more depth and test the connection between the additional contribution and the change in magnetic entropy related to the phase transition.

In this thesis, it was demonstrated that the microstructure devices fabricated by FIB cutting and lithography are suitable to study the anomalous Hall and anomalous Nernst effect, since the fabrication procedure can preserve the salient transport properties of high quality single crystals. Both transport responses can give insight into different extrinsic and intrinsic transport mechanism. Therefore, similar transport experiments should be performed on single crystal microstructures of various topological materials employing this magnetotransport platform.



# Bibliography

- B. Abeles and S. Meiboom, "Galvanomagnetic effects in bismuth", *Phys. Rev.* **101**, 544–550 (1956).
- S. L. Adler, "Axial-vector vertex in spinor electrodynamics", *Phys. Rev.* **177**, 2426–2438 (1969).
- M. N. Ali, J. Xiong, S. Flynn, J. Tao, Q. D. Gibson, L. M. Schoop, T. Liang, N. Haldolaarachchige, M. Hirschberger, N. P. Ong, and R. J. Cava, "Large, non-saturating magnetoresistance in WTe<sub>2</sub>", *Nature* **514**, 205–208 (2014).
- S. Arsenijevic, J. M. Ok, P. Robinson, S. Ghannadzadeh, M. I. Katsnelson, J. S. Kim, and N. E. Hussey, "Anomalous magnetothermopower in a metallic frustrated antiferromagnet", *Phys. Rev. Lett.* **116**, 087202 (2016).
- J. E. Aubrey, "Magnetoelectricity tensor for semimetals", *J. Phys. F* **1**, 493–497 (1971).
- A. Aziz, P. Mangelis, P. Vaqueiro, A. V. Powell, and R. Grau-Crespo, "Electron and phonon transport in shandite-structured  $\text{Ni}_3\text{Sn}_2\text{S}_2$ ", *Phys. Rev. B* **94**, 165131 (2016).
- M. N. Baibich, J. M. Broto, A. Fert, F. N. Van Dau, F. Petroff, P. Etienne, G. Creuzet, A. Friederich, and J. Chazelas, "Giant magnetoresistance of (001)Fe/(001)Cr magnetic superlattices", *Phys. Rev. Lett.* **61**, 2472–2475 (1988).
- J. S. Bell and R. Jackiw, "A peculiar puzzle:  $\pi^0 \rightarrow \gamma\gamma$  in the  $\sigma$ -model", *Il Nuovo Cimento A* (1965-1970) **60**, 47–61 (1969).
- L. Berger, "Influence of spin-orbit interaction on the transport processes in ferromagnetic nickel alloys, in the presence of a degeneracy of the 3d band", *Phys.* **30**, 1141–1159 (1964).
- M. V. Berry, "Quantal phase factors accompanying adiabatic changes", *Proc. R. Soc. London. Ser. A* **392**, 45–57 (1984).

- M. V. Berry, “Aspects of degeneracy”, in *Chaotic behavior in quantum systems: theory and applications*, edited by G. Casati (Springer US, Boston, MA, 1985), 123–140.
- G. Binasch, P. Grünberg, F. Saurenbach, and W. Zinn, “Enhanced magnetoresistance in layered magnetic structures with antiferromagnetic interlayer exchange”, *Phys. Rev. B* **39**, 4828–4830 (1989).
- F. J. Blatt, D. J. Flood, V. Rowe, P. A. Schroeder, and J. E. Cox, “Magnon-drag thermopower in iron”, *Phys. Rev. Lett.* **18**, 395–396 (1967).
- F. Blatt, A. Caplin, C. Chiang, and P. Schroeder, “Phonon drag thermopower of noble metals in a high magnetic field”, *Solid State Commun.* **15**, 411–414 (1974).
- M. Born and V. Fock, “Beweis des adiabatsatzes”, *Z. Phys.* **51**, 165–180 (1928).
- B. Bradlyn, L. Elcoro, J. Cano, M. G. Vergniory, Z. Wang, C. Felser, M. I. Aroyo, and B. A. Bernevig, “Topological quantum chemistry”, *Nature* **547**, 298–305 (2017).
- A. A. Burkov, “Anomalous hall effect in weyl metals”, *Phys. Rev. Lett.* **113**, 187202 (2014).
- F. Caglieris, A. Braggio, I. Pallecchi, A. Provino, M. Pani, G. Lamura, A. Jost, U. Zeitler, E. Galleani D’Aglia, P. Manfrinetti, and M. Putti, “Magneto-seebeck effect in  $r\text{FeAsO}$  ( $r$  = rare earth) compounds: probing the magnon drag scenario”, *Phys. Rev. B* **90**, 134421 (2014).
- M.-C. Chang and Q. Niu, “Berry phase, hyperorbits, and the hofstadter spectrum: semiclassical dynamics in magnetic bloch bands”, *Phys. Rev. B* **53**, 7010–7023 (1996).
- B. Chen, C. Uher, D. T. Morelli, J. V. Mantese, A. M. Mance, and A. L. Micheli, “Large magnetothermopower in  $\text{La}_{0.67}\text{Ca}_{0.33}\text{MnO}_3$  films”, *Phys. Rev. B* **53**, 5094–5097 (1996).
- Y. L. Chen, J. G. Analytis, J.-H. Chu, Z. K. Liu, S. K. Mo, X. L. Qi, H. J. Zhang, D. H. Lu, X. Dai, Z. Fang, S. C. Zhang, I. R. Fisher, Z. Hussain, and Z. X. Shen, “Experimental Realization of a Three-Dimensional Topological Insulator,  $\text{Bi}_2\text{Te}_3$ ”, *Science* **325**, 178–181 (2009).
- A. Collaudin, B. Fauqué, Y. Fuseya, W. Kang, and K. Behnia, “Angle dependence of the orbital magnetoresistance in bismuth”, *Phys. Rev. X* **5**, 021022 (2015).

J. Corps, P. Vaquero, A. Aziz, R. Grau-Crespo, W. Kockelmann, J.-C. Jumas, and A. V. Powell, "Interplay of metal-atom ordering, fermi level tuning, and thermoelectric properties in cobalt shandites  $\text{Co}_3\text{M}_2\text{S}_2$  ( $\text{M} = \text{Sn, In}$ )", *Chem. Mater.* **27**, 3946–3956 (2015).

J. Corps, P. Vaquero, and A. V. Powell, " $\text{Co}_3\text{M}_2\text{S}_2$  ( $\text{M} = \text{Sn, In}$ ) shandites as tellurium-free thermoelectrics", *J. Mater. Chem. A* **1**, 6553–6557 (2013).

M. Cutler and N. F. Mott, "Observation of anderson localization in an electron gas", *Phys. Rev.* **181**, 1336–1340 (1969).

Y. S. Dedkov, M Holder, S. L. Molodtsov, and H Rosner, "Electronic structure of shandite  $\text{Co}_3\text{Sn}_2\text{S}_2$ ", *J. Conf.* **100**, 072011 (2008).

F Delahaye and B Jeckelmann, "Revised technical guidelines for reliable dc measurements of the quantized hall resistance", *Metrologia* **40**, 217–223 (2003).

L. Ding, J. Koo, L. Xu, X. Li, X. Lu, L. Zhao, Q. Wang, Q. Yin, H. Lei, B. Yan, Z. Zhu, and K. Behnia, "Intrinsic anomalous nernst effect amplified by disorder in a half-metallic semimetal", *Phys. Rev. X* **9**, 041061 (2019).

P. Florian, T. A. Samuel, R. Jan, and W. Richard, "In Search for Novel  $\text{Sn}_2\text{Co}_3\text{S}_2$ -based Half-metal Ferromagnets", *Z. Naturforsch. B.* **69**, 55 (2014).

L. Fu, C. L. Kane, and E. J. Mele, "Topological insulators in three dimensions", *Phys. Rev. Lett.* **98**, 106803 (2007).

K. Geishendorf, R. Schlitz, P. Vir, C. Shekhar, C. Felser, K. Nielsch, S. T. B. Goennenwein, and A. Thomas, "Magnetoresistance and anomalous hall effect in micro-ribbons of the magnetic weyl semimetal  $\text{Co}_3\text{Sn}_2\text{S}_2$ ", *Appl. Phys. Lett.* **114**, 092403 (2019).

K. Geishendorf, P. Vir, C. Shekhar, C. Felser, J. I. Facio, J. van den Brink, K. Nielsch, A. Thomas, and S. T. B. Goennenwein, "Signatures of the magnetic entropy in the thermopower signals in nanoribbons of the magnetic weyl semimetal  $\text{Co}_3\text{Sn}_2\text{S}_2$ ", *Nano Lett.* **20**, 300–305 (2020).

M. P. Ghimire, J. I. Facio, J.-S. You, L. Ye, J. G. Checkelsky, S. Fang, E. Kaxiras, M. Richter, and J. van den Brink, "Creating weyl nodes and controlling their energy by magnetization rotation", *Phys. Rev. Res.* **1**, 032044 (2019).

A. Ghosh, R. Das, and R. Mahendiran, "Skew scattering dominated anomalous nernst effect in  $\text{La}_{1-x}\text{NaxMnO}_3$ ", *J. Appl. Phys.* **125**, 153902 (2019).



- D. A. Goodings, “Electrical resistivity of ferromagnetic metals at low temperatures”, *Phys. Rev.* **132**, 542–558 (1963).
- D. Gosálbez-Martinez, I. Souza, and D. Vanderbilt, “Chiral degeneracies and fermi-surface chern numbers in bcc fe”, *Phys. Rev. B* **92**, 085138 (2015).
- Z. Guguchia, J. Verezhak, D. Gawryluk, S. S. Tsirkin, J. X. Yin, I. Belopolski, H. Zhou, G. Simutis, S. S. Zhang, T. A. Cochran, G. Chang, E. Pomjakushina, L. Keller, Z. Skrzeczkowska, Q. Wang, H. C. Lei, R. Khasanov, A. Amato, S. Jia, T. Neupert, H. Luetkens, and M. Z. Hasan, “Tunable anomalous hall conductivity through volume-wise magnetic competition in a topological kagome magnet”, *Nat. Commun.* **11**, 559 (2020).
- S. N. Guin, P. Vir, Y. Zhang, N. Kumar, S. J. Watzman, C. Fu, E. Liu, K. Manna, W. Schnelle, J. Gooth, C. Shekhar, Y. Sun, and C. Felser, “Zero-field nernst effect in a ferromagnetic kagome-lattice weyl-semimetal  $\text{Co}_3\text{Sn}_2\text{S}_2$ ”, *Adv. Mater.* **31**, 1806622.
- E. H. Hall, “On a new action of the magnet on electric currents”, *Am. J. Math.* **2**, 287–292 (1879).
- C. Herring, “Accidental degeneracy in the energy bands of crystals”, *Phys. Rev.* **52**, 365–373 (1937).
- M. Hirschberger, S. Kushwaha, Z. Wang, Q. Gibson, S. Liang, C. A. Belvin, B. A. Bernevig, R. J. Cava, and N. P. Ong, “The chiral anomaly and thermopower of Weyl fermions in the half-Heusler  $\text{GdPtBi}$ ”, *Nat. Mater.* **15**, 1161–1165 (2016).
- M. Holder, Y. S. Dedkov, A. Kade, H. Rosner, W. Schnelle, A. Leithe-Jasper, R. Weihrich, and S. L. Molodtsov, “Photoemission study of electronic structure of the half-metallic ferromagnet  $\text{Co}_3\text{Sn}_2\text{S}_2$ ”, *Phys. Rev. B* **79**, 205116 (2009).
- D. Hsieh, D. Qian, L. Wray, Y. Xia, Y. S. Hor, R. J. Cava, and M. Z. Hasan, “A topological Dirac insulator in a quantum spin Hall phase”, *Nature* **452**, 970–974 (2008).
- D. Hsieh, Y. Xia, D. Qian, L. Wray, F. Meier, J. H. Dil, J. Osterwalder, L. Patthey, A. V. Fedorov, H. Lin, A. Bansil, D. Grauer, Y. S. Hor, R. J. Cava, and M. Z. Hasan, “Observation of time-reversal-protected single-dirac-cone topological-insulator states in  $\text{Bi}_2\text{Te}_3$  and  $\text{Sb}_2\text{Te}_3$ ”, *Phys. Rev. Lett.* **103**, 146401 (2009).
- X. Huang, L. Zhao, Y. Long, P. Wang, D. Chen, Z. Yang, H. Liang, M. Xue, H. Weng, Z. Fang, X. Dai, and G. Chen, “Observation of the chiral-anomaly-induced negative magnetoresistance in 3d weyl semimetal  $\text{TaAs}$ ”, *Phys. Rev. X* **5**, 031023 (2015).

- Y. Q. Huang, Y. X. Song, S. M. Wang, I. A. Buyanova, and W. M. Chen, "Spin injection and helicity control of surface spin photocurrent in a three dimensional topological insulator", *Nat. Commun.* **8**, 15401 (2017).
- A. Hubert and R. Schäfer, *Magnetic Domains: The Analysis of Magnetic Microstructures* (Springer, Berlin, Heidelberg, 1998).
- S. Iguchi, N. Hanasaki, and Y. Tokura, "Scaling of anomalous hall resistivity in  $\text{Nd}_2(\text{Mo}_{1-x}\text{Nb}_x)_2\text{O}_7$  with spin chirality", *Phys. Rev. Lett.* **99**, 077202 (2007).
- T. Jungwirth, Q. Niu, and A. H. MacDonald, "Anomalous hall effect in ferromagnetic semiconductors", *Phys. Rev. Lett.* **88**, 207208 (2002).
- C. L. Kane and E. J. Mele, "Quantum spin hall effect in graphene", *Phys. Rev. Lett.* **95**, 226801 (2005).
- C. L. Kane and E. J. Mele, "Z<sub>2</sub> topological order and the quantum spin hall effect", *Phys. Rev. Lett.* **95**, 146802 (2005).
- R. Karplus and J. M. Luttinger, "Hall effect in ferromagnetics", *Phys. Rev.* **95**, 1154–1160 (1954).
- M. A. Kassem, Y. Tabata, T. Waki, and H. Nakamura, "Single crystal growth and characterization of kagomé-lattice shandites  $\text{Co}_3\text{Sn}_2\text{X}_2$ ", *J. Cryst. Growth* **426**, 208–213 (2015).
- M. A. Kassem, Y. Tabata, T. Waki, and H. Nakamura, "Quasi-Two-Dimensional Magnetism in Co-Based Shandites", *J. Phys. Soc. Jpn.* **85**, 064706–7 (2016).
- M. A. Kassem, Y. Tabata, T. Waki, and H. Nakamura, "Structure and magnetic properties of flux grown single crystals of  $\text{Co}_3\text{X}_2\text{Fe}_x\text{Sn}_{2-x}\text{S}_2$  shandites", *J. Solid State Chem.* **233**, 8–13 (2016).
- M. A. Kassem, Y. Tabata, T. Waki, and H. Nakamura, "Low-field anomalous magnetic phase in the kagome-lattice shandite  $\text{Co}_3\text{Sn}_2\text{S}_2$ ", *Phys. Rev. B* **96**, 014429–6 (2017).
- T. Kasuya, "Electrical Resistance of Ferromagnetic Metals", *Prog. Theor. Phys.* **16**, 58–63 (1956).
- H.-J. Kim, K.-S. Kim, J.-F. Wang, M. Sasaki, N. Satoh, A. Ohnishi, M. Kitaura, M. Yang, and L. Li, "Dirac versus weyl fermions in topological insulators: adler-bell-jackiw anomaly in transport phenomena", *Phys. Rev. Lett.* **111**, 246603 (2013).
- K. v. Klitzing, G. Dorda, and M. Pepper, "New method for high-accuracy determination of the fine-structure constant based on quantized hall resistance", *Phys. Rev. Lett.* **45**, 494–497 (1980).

- M. König, S. Wiedmann, C. Brüne, A. Roth, H. Buhmann, L. W. Molenkamp, X.-L. Qi, and S.-C. Zhang, “Quantum spin hall insulator state in hgte quantum wells”, *Science* **318**, 766–770 (2007).
- T. Kubodera, H. Okabe, Y. Kamihara, and M. Matoba, “Ni substitution effect on magnetic and transport properties in metallic ferromagnet  $\text{Co}_3\text{Sn}_2\text{S}_2$ ”, *Physica B: Condens. Matter* **378–380**, 1142–1143 (2006).
- A. Kumar, C. V. Tomy, and A. D. Thakur, “Magnetothermopower, magnetoresistance and magnetothermal conductivity in  $\text{La}_{0.95}\text{Sr}_{0.05}\text{Co}_{1-x}\text{Mn}_x\text{O}_3$  ( $0.00 \leq x \leq 1.00$ )”, *Mater. Res. Express* **5**, 086110 (2018).
- N. Kumar, Y. Sun, N. Xu, K. Manna, M. Yao, V. Süß, I. Leermakers, O. Young, T. Förster, M. Schmidt, H. Borrmann, B. Yan, U. Zeitler, M. Shi, C. Felser, and C. Shekhar, “Extremely high magnetoresistance and conductivity in the type-II Weyl semimetals  $\text{WP}_2$  and  $\text{MoP}_2$ ”, *Nat. Commun.* **8**, 1642 (2017).
- R. B. Laughlin, “Quantized hall conductivity in two dimensions”, *Phys. Rev. B* **23**, 5632–5633 (1981).
- M. Lee, Y. Onose, Y. Tokura, and N. P. Ong, “Hidden constant in the anomalous hall effect of high-purity magnet  $\text{MnSi}$ ”, *Phys. Rev. B* **75**, 172403 (2007).
- C.-Z. Li, L.-X. Wang, H. Liu, J. Wang, Z.-M. Liao, and D.-P. Yu, “Giant negative magnetoresistance induced by the chiral anomaly in individual  $\text{Cd}_3\text{As}_2$  nanowires”, *Nat. Commun.* **6**, 10137 (2015).
- Y. Li, Z. Wang, P. Li, X. Yang, Z. Shen, F. Sheng, X. Li, Y. Lu, Y. Zheng, and Z.-A. Xu, “Negative magnetoresistance in weyl semimetals  $\text{nbn}$  and  $\text{nbp}$ : intrinsic chiral anomaly and extrinsic effects”, *Front. Phys.* **12**, 127205 (2017).
- S. Liang, J. Lin, S. Kushwaha, J. Xing, N. Ni, R. J. Cava, and N. P. Ong, “Experimental tests of the chiral anomaly magnetoresistance in the dirac-weyl semimetals  $\text{Na}_3\text{Bi}$  and  $\text{GdPtBi}$ ”, *Phys. Rev. X* **8**, 031002 (2018).
- T. Liang, Q. Gibson, M. N. Ali, M. Liu, R. J. Cava, and N. P. Ong, “Ultrahigh mobility and giant magnetoresistance in the Dirac semimetal  $\text{Cd}_3\text{As}_2$ ”, *Nat. Mater.* **14**, 280–284 (2015).
- I. M. Lifshitz, M. Y. Azbel, and K. M. I., *Zh. Eksperim. i Teor. Fiz.* **31** (1956), English translation: *Soviet Phys.- JETP* **12**, 283 (1961).
- F. V. Lisovskii, E. G. Mansvetova, M. P. Temiryazeva, and A. G. Temiryazev, “Study of the branching domain structures in epitaxial films of yttrium iron garnet by end face magnetic force microscopy”, *JETP Letters* **96**, 596–600 (2013).

- E. Liu, Y. Sun, N. Kumar, L. Muechler, A. Sun, L. Jiao, S.-Y. Yang, D. Liu, A. Liang, Q. Xu, J. Kroder, V. Süß, H. Borrmann, C. Shekhar, Z. Wang, C. Xi, W. Wang, W. Schnelle, S. Wirth, Y. Chen, S. T. B. Goennenwein, and C. Felser, "Giant anomalous Hall effect in a ferromagnetic kagome-lattice semimetal", *Nat. Phys.* **14**, 1125–1131 (2018).
- H. C. Longuet-Higgins, U. Öpik, M. H. L. Pryce, and R. A. Sack, "Studies of the jahn-teller effect. ii. the dynamical problem", *Proc. R. Soc. London. Ser. A* **244**, 1–16 (1958).
- J. M. Luttinger, "Theory of thermal transport coefficients", *Phys. Rev.* **135**, A1505–A1514 (1964).
- B. Q. Lv, N. Xu, H. M. Weng, J. Z. Ma, P. Richard, X. C. Huang, L. X. Zhao, G. F. Chen, C. E. Matt, F. Bisti, V. N. Strocov, J. Mesot, Z. Fang, X. Dai, T. Qian, M. Shi, and H. Ding, "Observation of Weyl nodes in TaAs", *Nat. Phys.* **11**, 724–727 (2015).
- D. V. Maheswar Repaka, T. S. Tripathi, M. Aparnadevi, and R. Mahendiran, "Magnetocaloric effect and magnetothermopower in the room temperature ferromagnet  $\text{Pr}_{0.6}\text{Sr}_{0.4}\text{MnO}_3$ ", *J. Appl. Phys.* **112**, 123915 (2012).
- P. Mangelis, P. Vaqueiro, J.-C. Jumas, I. da Silva, R. I. Smith, and A. V. Powell, "The effect of electron and hole doping on the thermoelectric properties of shandite-type  $\text{Co}_3\text{Sn}_2\text{S}_2$ ", *J. Solid State Chem.* **251**, 204–210 (2017).
- J. H. Mangenz, J. P. Issi, and J. Heremans, "Transport properties of bismuth in quantizing magnetic fields", *Phys. Rev. B* **14**, 4381–4385 (1976).
- Y. Masuda, T. Hioki, and A. Oota, "Spin fluctuations in itinerant electron ferromagnet  $\text{Sc}_3\text{In}$ ", *Physica B+C* **91**, 291–297 (1977).
- J. Mathon and E. P. Wohlfarth, "The temperature dependence of the spin wave energy in the itinerant electron model of ferromagnetism", *Proc. R. Soc. London. Ser. A* **302**, 409–418 (1968).
- M. Matusiak, T. Plackowski, Z. Bukowski, N. D. Zhigadlo, and J. Karpinski, "Evidence of spin-density-wave order in  $\text{FeAsO}_1 - x\text{F}_x$  from measurements of thermoelectric power", *Phys. Rev. B* **79**, 212502 (2009).
- T. McGuire and R. Potter, "Anisotropic magnetoresistance in ferromagnetic 3d alloys", *IEEE T.Magn.* **11**, 1018–1038 (1975).
- A. P. Mihai, J. P. Attané, A. Marty, P. Warin, and Y. Samson, "Electron-magnon diffusion and magnetization reversal detection in FePt thin films", *Phys. Rev. B* **77**, 060401 (2008).

- T. Miyasato, N. Abe, T. Fujii, A. Asamitsu, S. Onoda, Y. Onose, N. Nagaosa, and Y. Tokura, "Crossover behavior of the anomalous hall effect and anomalous nernst effect in itinerant ferromagnets", *Phys. Rev. Lett.* **99**, 086602 (2007).
- N. Nagaosa, J. Sinova, S. Onoda, A. H. MacDonald, and N. P. Ong, "Anomalous hall effect", *Rev. Mod. Phys.* **82**, 1539–1592 (2010).
- S. Natarajan, G. Rao, R. Baskaran, and T. Radhakrishnan, "Synthesis and electrical properties of shandite-parkerite phases,  $\text{a}_2\text{m}_3\text{ch}_2$ ", *J. Less Common Met.* **138**, 215–224 (1988).
- V. D. Nguyen, C. Naylor, L. Vila, A. Marty, P. Laczkowski, C. Beigné, L. Notin, Z. Ishaque, and J. P. Attané, "Magnon magnetoresistance of nife nanowires: size dependence and domain wall detection", *Appl. Phys. Lett.* **99**, 262504 (2011).
- V. D. Nguyen, L. Vila, P. Laczkowski, A. Marty, T. Faivre, and J. P. Attané, "Detection of domain-wall position and magnetization reversal in nanostructures using the magnon contribution to the resistivity", *Phys. Rev. Lett.* **107**, 136605 (2011).
- H. Nielsen and M. Ninomiya, "The adler-bell-jackiw anomaly and weyl fermions in a crystal", *Phys. Lett. B.* **130**, 389–396 (1983).
- A. Niemann, J. Gooth, S. Wu, S. Bäsler, P. Sergelius, R. Hühne, C. Rellinhaus B. Shekhar, V. Süß, M. Schmidt, C. Felser, B. Yan, and K. Nielsch, *Sci. Rep.* **7**, 43394 (2017).
- J. Noky, J. Gooth, C. Felser, and Y. Sun, "Characterization of topological band structures away from the fermi level by the anomalous nernst effect", *Phys. Rev. B* **98**, 241106 (2018).
- R. O'Handley, *Modern magnetic materials: principles and applications* (Wiley, 1999).
- S. Onoda, N. Sugimoto, and N. Nagaosa, "Quantum transport theory of anomalous electric, thermoelectric, and thermal hall effects in ferromagnets", *Phys. Rev. B* **77**, 165103 (2008).
- I. Pallecchi, F. Caglieris, and M. Putti, "Thermoelectric properties of iron-based superconductors and parent compounds", *Supercond. Sci. Technol.* **29**, 073002 (2016).
- S. Pancharatnam, "Generalized theory of interference, and its applications", *Proc. Natl. Acad. Sci. India A* **44**, 247–262 (1956).
- Y. Pu, D. Chiba, F. Matsukura, H. Ohno, and J. Shi, "Mott relation for anomalous hall and nernst effects in  $\text{ga}_{1-x}\text{mn}_x\text{As}$  ferromagnetic semiconductors", *Phys. Rev. Lett.* **101**, 117208 (2008).

R. Ramos, M. H. Aguirre, A. Anadón, J. Blasco, I. Lucas, K. Uchida, P. A. Algarabel, L. Morellón, E. Saitoh, and M. R. Ibarra, “Anomalous nernst effect of  $\text{Fe}_3\text{O}_4$  single crystal”, *Phys. Rev. B* **90**, 054422 (2014).

B. Raquet, M. Viret, E. Sondergard, O. Céspedes, and R. Mamy, “Electron-magnon scattering and magnetic resistivity in  $3d$  ferromagnets”, *Phys. Rev. B* **66**, 024433 (2002).

R. D. dos Reis, M. O. Ajeesh, N. Kumar, F. Arnold, C. Shekhar, M. Naumann, M. Schmidt, M. Nicklas, and E. Hassinger, “On the search for the chiral anomaly in weyl semimetals: the negative longitudinal magnetoresistance”, *New J. Phys.* **18**, 085006 (2016).

W. Schnelle, A. Leithe-Jasper, H. Rosner, F. M. Schappacher, R. Pöttgen, F. Pielnhofer, and R. Wehrich, “Ferromagnetic ordering and half-metallic state of  $\text{Sn}_2\text{Co}_3\text{S}_2$  with the shandite-type structure”, *Phys. Rev. B* **88**, 144404 (2013).

C. Shekhar, A. K. Nayak, Y. Sun, M. Schmidt, M. Nicklas, I. Leermakers, U. Zeitler, Y. Skourski, J. Wosnitza, Z. Liu, Y. Chen, W. Schnelle, H. Borrmann, Y. Grin, C. Felser, and B. Yan, “Extremely large magnetoresistance and ultrahigh mobility in the topological Weyl semimetal candidate NbP”, *Nat. Phys.* **11**, 645–649 (2015).

Q. Shi, X. Zhang, E. Yang, J. Yan, X. Yu, C. Sun, S. Li, and Z. Chen, “Study of magnetocaloric effect in half-metallic ferromagnet  $\text{Co}_3\text{Sn}_2\text{S}_2$ ”, *Results Phys.* **11**, 1004–1007 (2018).

J. Smit, “The spontaneous hall effect in ferromagnetics i”, *Physica* **21**, 877–887 (1955).

J. Smit, “The spontaneous hall effect in ferromagnetics ii”, *Physica* **24**, 39–51 (1958).

J. Smit and J. Volger, “Spontaneous hall effect in ferromagnetics”, *Phys. Rev.* **92**, 1576–1577 (1953).

S. Souma, Z. Wang, H. Kotaka, T. Sato, K. Nakayama, Y. Tanaka, H. Kimizuka, T. Takahashi, K. Yamauchi, T. Oguchi, K. Segawa, and Y. Ando, “Direct observation of nonequivalent fermi-arc states of opposite surfaces in the noncentrosymmetric weyl semimetal nbp”, *Phys. Rev. B* **93**, 161112 (2016).

G. Sundaram and Q. Niu, “Wave-packet dynamics in slowly perturbed crystals: gradient corrections and berry-phase effects”, *Phys. Rev. B* **59**, 14915–14925 (1999).

G. R. Taylor, A. Isin, and R. V. Coleman, “Resistivity of iron as a function of temperature and magnetization”, *Phys. Rev.* **165**, 621–631 (1968).



- D. J. Thouless, M. Kohmoto, M. P. Nightingale, and M. den Nijs, "Quantized hall conductance in a two-dimensional periodic potential", *Phys. Rev. Lett.* **49**, 405–408 (1982).
- N. Tsujii, A. Nishide, J. Hayakawa, and T. Mori, "Observation of enhanced thermopower due to spin fluctuation in weak itinerant ferromagnet", *Sci. Adv.* **5** (2019).
- K. Ueda, "Effect of magnetic field on spin fluctuations in weakly ferromagnetic metals", *Solid State Commun.* **19**, 965–968 (1976).
- P. Vaquero and G. G. Sobany, "A powder neutron diffraction study of the metallic ferromagnet  $\text{Co}_3\text{Sn}_2\text{S}_2$ ", *Solid State Sci.* **11**, 513–518 (2009).
- M. G. Vergniory, L. Elcoro, C. Felser, N. Regnault, B. A. Bernevig, and Z. Wang, "A complete catalogue of high-quality topological materials", *Nature* **566**, 480–485 (2019).
- X. Wan, A. M. Turner, A. Vishwanath, and S. Y. Savrasov, "Topological semimetal and fermi-arc surface states in the electronic structure of pyrochlore iridates", *Phys. Rev. B* **83**, 205101 (2011).
- Z. Wang, Y. Zheng, Z. Shen, Y. Lu, H. Fang, F. Sheng, Y. Zhou, X. Yang, Y. Li, C. Feng, and Z.-A. Xu, "Helicity-protected ultrahigh mobility weyl fermions in  $\text{nbp}$ ", *Phys. Rev. B* **93**, 121112 (2016).
- R. Weihrich, A. C. Stückl, M. Zabel, and W. Schnelle, "Magnetischer phasenübergang des  $\text{Co}_3\text{Sn}_2\text{S}_2$ ", *Z. Anorg. Allg. Chem.* **630**, 1767–1767 (2004).
- R. Weihrich and I. Anusca, "Half antiperovskites. iii. crystallographic and electronic structure effects in  $\text{sn}_2 - \text{xinxcO}_3\text{S}_2$ ", *Z. Anorg. Allg. Chem.* **632**, 1531–1537 (2006).
- R. Weihrich, I. Anusca, and M. Zabel, "Halbantiperowskite: zur struktur der shandite  $\text{m}_3/2\text{as}$  ( $\text{m} = \text{Co, Ni}$ ;  $\text{a} = \text{In, Sn}$ ) und ihren typ-antitypbeziehungen", *Z. Anorg. Allg. Chem.* **631**, 1463–1470 (2005).
- H. Weyl, "Elektron und Gravitation. I", *Z. Phys.* **56**, 330–352 (1929).
- G. V. M. Williams and J. E. Stephen, "Magnetothermopower in  $\text{A}_{2-x}\text{La}_x\text{FeMoO}_6$  ( $\text{A} = \text{Sr, Ba}$ )", *Adv. Cond. Matter Phys.* **2017**, 7578930 (2017).
- Y. Xia, D. Qian, D. Hsieh, L. Wray, A. Pal, H. Lin, A. Bansil, D. Grauer, Y. S. Hor, R. J. Cava, and M. Z. Hasan, "Observation of a large-gap topological-insulator class with a single Dirac cone on the surface", *Nat. Phys.* **5**, 398–402 (2009).



D. Xiao, Y. Yao, Z. Fang, and Q. Niu, "Berry-phase effect in anomalous thermoelectric transport", *Phys. Rev. Lett.* **97**, 026603 (2006).

J. Xiong, S. K. Kushwaha, T. Liang, J. W. Krizan, M. Hirschberger, W. Wang, R. J. Cava, and N. P. Ong, "Evidence for the chiral anomaly in the dirac semimetal  $\text{Na}_3\text{Bi}$ ", *Science* **350**, 413–416 (2015).

J. Xu, W. A. Phelan, and C.-L. Chien, "Large anomalous nernst effect in a van der waals ferromagnet  $\text{Fe}_3\text{GeTe}_2$ ", *Nano Lett.* **19**, 8250–8254 (2019).

N Xu, H. M. Weng, B. Q. Lv, C. E. Matt, J Park, F Bisti, V. N. Strocov, D Gawryluk, E Pomjakushina, K Conder, N. C. Plumb, M Radovic, G Autès, O. V. Yazyev, Z Fang, X Dai, T Qian, J Mesot, H Ding, and M Shi, "Observation of Weyl nodes and Fermi arcs in tantalum phosphide", *Nat. Commun.* **7**, 11006 (2016).

Q. Xu, E. Liu, W. Shi, L. Muechler, J. Gayles, C. Felser, and Y. Sun, "Topological surface fermi arcs in the magnetic weyl semimetal  $\text{Co}_3\text{Sn}_2\text{S}_2$ ", *Phys. Rev. B* **97**, 235416 (2018).

S.-Y. Xu, N. Alidoust, I. Belopolski, Z. Yuan, G. Bian, T.-R. Chang, H. Zheng, V. N. Strocov, D. S. Sanchez, G. Chang, C. Zhang, D. Mou, Y. Wu, L. Huang, C.-C. Lee, S.-M. Huang, B. Wang, A. Bansil, H.-T. Jeng, T. Neupert, A. Kaminski, H. Lin, S. Jia, and M Zahid Hasan, "Discovery of a Weyl fermion state with Fermi arcs in niobium arsenide", *Nat. Phys.* **11**, 748–754 (2015).

S.-Y. Xu, I. Belopolski, N. Alidoust, M. Neupane, G. Bian, C. Zhang, R. Sankar, G. Chang, Z. Yuan, C.-C. Lee, S.-M. Huang, H. Zheng, J. Ma, D. S. Sanchez, B. Wang, A. Bansil, F. Chou, P. P. Shibayev, H. Lin, S. Jia, and M. Z. Hasan, "Discovery of a weyl fermion semimetal and topological fermi arcs", *Science* **349**, 613–617 (2015).

W. Yan, X. Zhang, Q. Shi, X. Yu, Z. Zhang, Q. Wang, S. Li, and H. Lei, "Critical behavior of half-metallic ferromagnet  $\text{Co}_3\text{Sn}_2\text{S}_2$ ", *Solid State Commun.* **281**, 57 –61 (2018).

J. Yang, W. L. Zhen, D. D. Liang, Y. J. Wang, X. Yan, S. R. Weng, J. R. Wang, W. Tong, L. Pi, W. K. Zhu, and C. J. Zhang, "Current jetting distorted planar hall effect in a weyl semimetal with ultrahigh mobility", *Phys. Rev. Materials* **3**, 014201 (2019).

K.-Y. Yang, Y.-M. Lu, and Y. Ran, "Quantum hall effects in a weyl semimetal: possible application in pyrochlore iridates", *Phys. Rev. B* **84**, 075129 (2011).

- L. X. Yang, Z. K. Liu, Y Sun, H Peng, H. F. Yang, T Zhang, B Zhou, Y Zhang, Y. F. Guo, M Rahn, D Prabhakaran, Z Hussain, S. K. Mo, C Felser, B Yan, and Y. L. Chen, “Weyl semimetal phase in the non-centrosymmetric compound TaAs”, *Nat. Phys.* **11**, 728–732 (2015).
- M. Zabel, S. Wandiger, and K.-J. Range, “Ternäre chalkogenide  $m_3m_2 \times 2$  mit shandit-struktur”, *Z.Naturforsch.* **34b**, 238–241 (1979).
- C.-L. Zhang, Z. Yuan, Q.-D. Jiang, B. Tong, C. Zhang, X. C. Xie, and S. Jia, “Electron scattering in tantalum monoarsenide”, *Phys. Rev. B* **95**, 085202 (2017).
- S. Zhang, Q. Wu, Y. Liu, and O. V. Yazyev, “Magnetoresistance from fermi surface topology”, *Phys. Rev. B* **99**, 035142 (2019).
- Y. Zhao, H. Liu, J. Yan, W. An, J. Liu, X. Zhang, H. Wang, Y. Liu, H. Jiang, Q. Li, Y. Wang, X.-Z. Li, D. Mandrus, X. C. Xie, M. Pan, and J. Wang, “Anisotropic magnetotransport and exotic longitudinal linear magnetoresistance in WTe<sub>2</sub> crystals”, *Phys. Rev. B* **92**, 041104 (2015).